UNIVERSITA' DEGLI STUDI DI CATANIA
Dottorato di Ricerca in Scienza dei Materiali – XXIV Ciclo

B and Sb in germanium for micro and optoelectronics

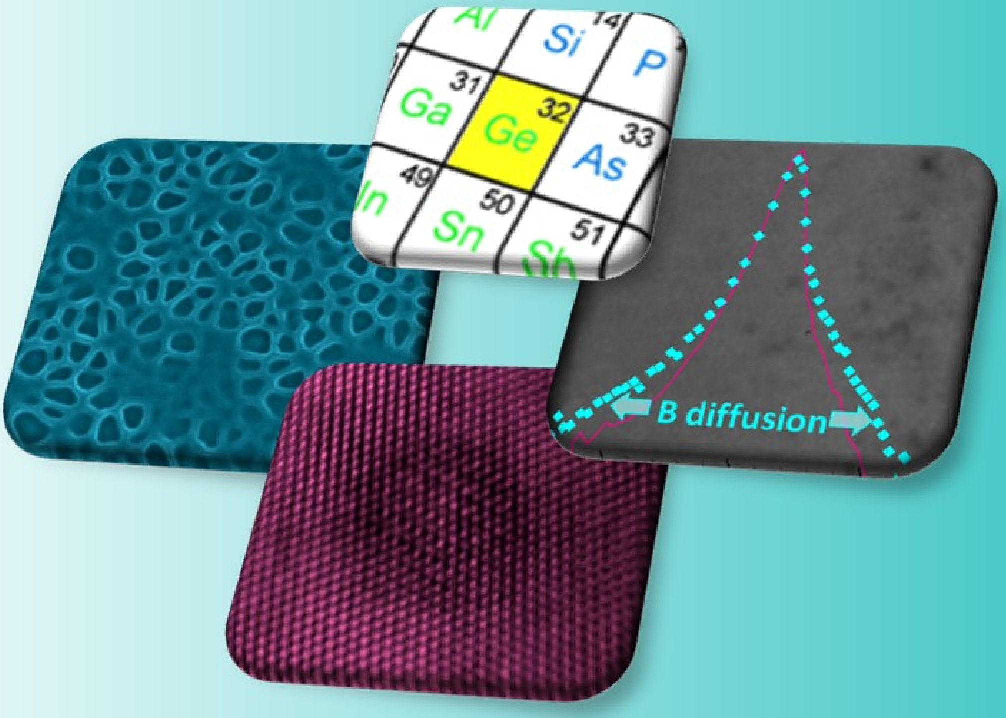

Giorgia G. Scapellato

Tutor: Prof. F. Priolo
Supervisor: Dr. E. Bruno
Coordinatore: Prof. A. Licciardello

Tesi per il conseguimento del titolo

UNIVERSITÀ DEGLI STUDI DI CATANIA

Dottorato di Ricerca in Scienza dei Materiali – XXIV Ciclo

Giorgia G. Scapellato

B and Sb in germanium
for micro and optoelectronics

Tutor: Prof. F. Priolo
Supervisor: Dr. E. Bruno
Coordinatore: Prof. A. Licciardello

Tesi per il conseguimento del titolo

To my granfather

Cover

Top:	*Part of the periodic table of elements.*
Left:	*Scanning electron microscopy image of Ge implanted with Sb. More details can be found within this thesis in section 4.4.2.*
Right:	*B concentration profiles obtained with Secondary Ion Mass Spectrometry analysis, superimposed on Cross Section Transmission Electron Microscopy image of a Ge sample amorphized with Ge and then regrowth. More details can be found within this thesis in section 2.3.2.*
Bottom:	*High resolution Transmission Electron Micoscopy image of a GeO_2 nanocluster embedded in a Ge matrix. More details can be found within this thesis in paragraph 3.4.*

B and Sb in germanium for micro and optoelectronics
Giorgia G. Scapellato
Ph.D Thesis – University of Catania
Printed in Catania, 2011

L'uomo è irragionevole, illogico, egocentrico.
NON IMPORTA, AMALO.
Se fai il bene, ti attribuiranno secondi fini egoistici.
NON IMPORTA, FA' IL BENE.
Se realizzi i tuoi obiettivi, troverai falsi amici e veri nemici.
NON IMPORTA, REALIZZALI.
Il bene che fai verrà domani dimenticato.
NON IMPORTA, FA' IL BENE.
L'onestà e la sincerità ti rendono vulnerabile.
NON IMPORTA, SII FRANCO E ONESTO.
Quello che per anni hai costruito può essere distrutto in un attimo.
NON IMPORTA, COSTRUISCI.
Se aiuti la gente, se ne risentirà.
NON IMPORTA, AIUTALA.
Da' al mondo il meglio di te, e ti prenderanno a calci.
NON IMPORTA, DA' IL MEGLIO DI TE.

Madre Teresa di Calcutta

People are often unreasonable, illogical and self-centered.
FORGIVE THEM ANYWAY.
If you are kind, people may accuse you of selfish ulterior motives.
BE KIND ANYWAY.
If you are successful, you will win some false friends and true
enemies. SUCCEED ANYWAY.
If you are honest and frank, people may cheat you.
BE HONEST ANYWAY.
What you spend years building, someone could destroy overnight.
BUILD ANYWAY.
If you find serenity and happiness, they may be jealous.
BE HAPPY ANYWAY.
The good you do today, people will often forget Tomorrow.
DO GOOD ANYWAY.
Give the world the best you have, and it may never be enough.
GIVE THE WORLD THE BEST YOU'VE GOT ANYWAY.

Mother Teresa of Calcutta

Contents

Chapter 2

Chapter 3

Chapter 4

Introduction

The history of Ge is somewhat controversial. The existence of an element of the IV group of the periodic table, placed between Si and Sn, was predicted by Mendeleev in 1871. He called the unknown element *eka-silicon*. Only fifteen years later Winkler found the missing element in the silver-rich mineral argyrodite. He studied the properties of this new material and called it germanium. Nonetheless, a misunderstanding about its electrical properties, which lasted until the late 1930s, considered germanium as a poorly conducting metal [1] and hampered its correct analysis.

The studies on the physics of semiconductors had a difficult development in the early 20th century. This situation was due, first of all, to the difficulty to properly control impurities and defects in semiconductors in order to obtain reproducible results. At the same time, this science was negatively judged from several influential physicists that had defined it as the “physics of dirt”. In this respect, Wolfgang Pauli berated Rudolf Peierls for his temerity in proposing to study the theory of electric conduction in solids — “one shouldn’t wallow in dirt” was Pauli’s judgment [2]. In spite of this, the interest in semiconductors was kept alive during the World War II thanks to the studies principally conducted at the Purdue University [3], where germanium was used to produce radar receivers. At the end of the War great advances were made in producing high purity germanium thanks to the techniques developed by Ohl, Teal, and Storks [4-6]. This condition made it possible to produce very good, reliable, low noise, point-contact diodes for the radar receivers [7].

The study of the physics of semiconductors continued after the War, with the new objective to make three terminal devices to substitute the vacuum tube triode, invented in 1906 by Lee De Forest [8]. Indeed, even if the vacuum tubes helped the development of telephony, radio and computers, they were too big, not reliable and required too much power to run. In the late 1940's, big computers were built with over 10000 vacuum tubes and occupied over 93 square meters of space.

The invention that definitively created a breakthrough and signed the begin of a new era, occurred in the night of the Christmas Eve of 1947 in Bell Telephone Laboratories by the physicists J. Bardeen and W. Brattain. It was made with a germanium polycrystalline slab: the point contact transistor (shown in Fig. I.1). Unfortunately, the two very fine point contacts pressed onto the germanium surface did not form a mechanically stable configuration. Moreover this device was not able to carry high currents. In this respect, the junction transistor invented by W. Shockley in 1949 remedied both the shortcomings of the point contact transistor [9]. Thanks to this invention Bardeen, Brattain and Shockley received the Nobel Prize in physics in the 1956.

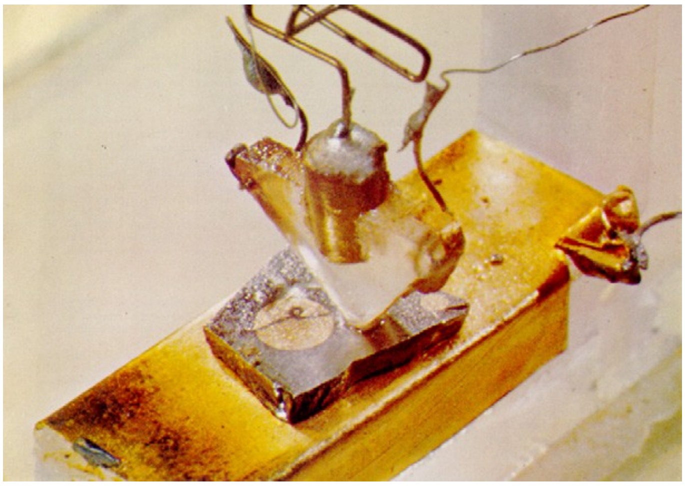

Fig. I.1 The first point-contact transistor fabricated by J. Bardeen and W. Brattain in Bell Laboratories in 1948 with a slab of polycrystalline germanium [10].

For more than a decade, till the late ‘50s , germanium was the material mainly used for the development of bipolar transistors, because it was available with the best quality achievable at that time. Moreover, thanks to the possibility to grow germanium single crystals with the method developed in 1950 by Teal and Little [11], as well as to the upgrade of doping techniques based on melt doping, alloying and diffusion, indeed, the semiconductor technology become a worldwide effort. In this respect, also the first integrated circuit (Fig. I.2), made by Kilby in 1958, for which he received the Nobel prize in physics in the 2000 [12], was made on a germanium slab.

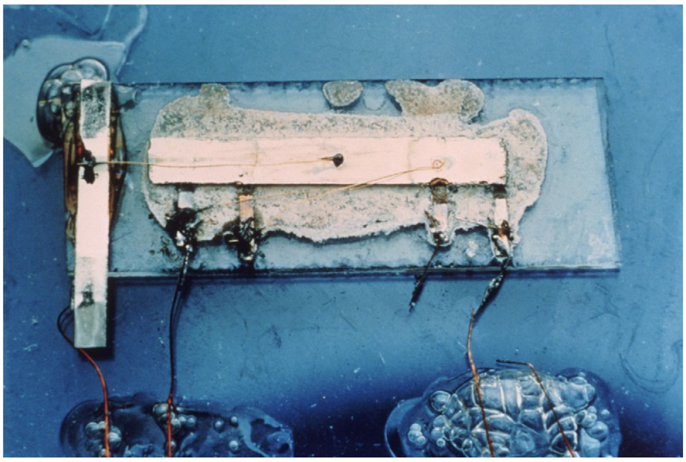

Fig. I.2 The first integrated germanium circuit built by J. Kilby at Texas Instruments in 1958 [1].

On the other hand, the subsequent progress in the germanium field effect devices was less prosperous, principally because of the low quality of the germanium oxide [13], that provided insufficient passivation of the Ge surface. Conversely, the remarkable properties of SiO_2 progressively moved the attention to Si in order to realize new devices with good Si surface passivation layer, high quality gate insulator, as well as field isolation between adjacent devices. So, all these properties, in combination with the introduction of the planar technology on silicon wafer [14] turned out to be the end of the germanium era in the microelectronic field. Silicon has been the workhorse of the microelectronics industry ever since. In this respect, the 15th November of the current year it was celebrate the 40th birthday of the first Intel Si-based microprocessor. The Intel 4004 had 2300 transistors, could make 1200 calculations per second and was made of a single piece of silicon. Since the days of the Intel 4004, CPU design has made massive leaps forward and, as predicted by Moore's law (depicted in Fig. I.3), the number of transistors on, and as a consequence also the power of, microprocessors have doubled every two years. Compared to the Intel 4004, today's second-generation Intel Core processors have more than 350000 times the performance and each transistor uses about 5000 times less energy.

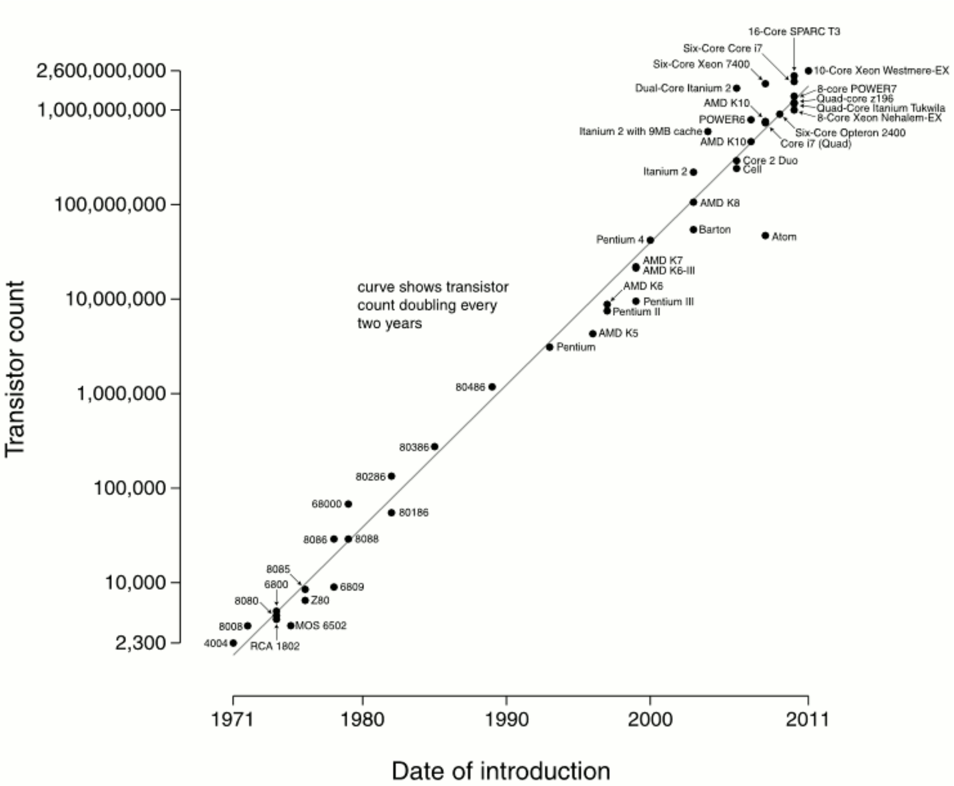

Fig. I.3 Moore's law for microprocessor from 1971 to 2011 [15].

In spite of this, recently, the progressive device shrinking has lead to new technological and fundamental limits of scalability of Si devices, before detrimental effects (e.g. leakage current) compromise the device performances [16]. This means that improvements based on fundamental properties, not only on dimensions, have to be found. So, it is essential to study new materials to further improve the performances of integrated circuits.

The introduction of high-*k* dielectrics as a replacement for SiO_2 has released many of the constraints that forced to abandon germanium as a microelectronic material and we are now facing a renewed interest in Ge. Germanium is indeed currently considered as a potential replacement for silicon [10]. The main advantage of Ge over Si is its superior electron and hole mobility, allowing to enhance the drive current of the transistors. The lower band-gap of Ge (~0.66 eV) compared to Si (~1.1 eV) should also allow further scaling of the supply voltage. Finally, the reduced thermal budget needed for dopant activation of a Ge-based MOSFET (metal-oxide-semiconductor field-effect transistor), i.e. around 500–600°C, compared to that in Si (1000–1100°C), also makes this material particularly interesting with respect to high-*k*/metal gate integration.

On the other hand, as the computational capacity of the chips increases, they need higher-bandwidth connections to send and receive data. To transmit data with lasers, by replacing conventional electrical connections, could be much more power-efficient. Nonetheless, a common platform is required to implement these powerful technology devices, that integrates both optical and electronic functionalities. Also in this case, germanium is gaining an important place. Indeed, it is known that, thanks to its structure, Ge is highly compatible with the already existent Si-based technology so that the feasibility of Ge processing in a standard Si process line has been demonstrated. Moreover, thanks to its peculiar indirect energy band structure, that shows a difference between the direct and indirect band-gap of only 136 meV, germanium seems to be very promising for the realization of an efficient coherent source of light. Indeed, it was recently observed [17] that the direct-gap emission of Ge is as efficient as that of direct band-gap semiconductors (e.g. GaAs). As a consequence, the scientific community has recently spent large efforts in developing a proper band-gap engineering in order to enhance the direct transitions, and then the optical gain, using both strain and n-type doping effects.

Despite the very promising electrical and optical properties, further studies are needed to effectively use and integrate germanium as a material for new generation, more performing, micro and optoelectronic devices. In particular, first of all, it is necessary, to have a deep comprehension not only about germanium properties but also on the behavior of foreign atoms in Ge. Unfortunately, due to the above mentioned abandon of germanium for the last 50 years, the knowledge on this semiconductor is quite incomplete. For this reason, many points are still unclear and need to be better understood. In this respect, the study presented in this thesis wants to be a step forward on the full comprehension of this material.

The plan of the present dissertation is the following.

In Chapter 1 the general concepts necessary for the comprehension of the thesis work are given. First of all, a brief overview on the similarities and differences between germanium and silicon is presented. In particular, the attention is focused on the advantage of Ge over Si, in order to realize both micro and optoelectronic devices. In this respect, a critical point is represented by doping. Indeed, a good control of dopants in Ge is essential for the realization of new generation microelectronic devices. It is crucial to take into account several processes related to germanium doping, such as diffusion, electrical activation and precipitation, as well as to understand the role of the native point defects on the dopant behavior in Ge. On the other hand, an overview on the indirect band-gap properties, comparing Si and Ge, is given, focusing on Ge peculiar energy band structure and on the need to find new approaches with respect to the Si case, to obtain light emission from Ge. A brief review on Ge band-gap engineering using tensile strain and n-type doping is reported, underlying the points that need to be still understood and solved.

Starting from Chapter 2 the experimental results of our work are presented. In particular, Chapter 2 focuses the attention on the atomistic mechanism of boron diffusion in Ge. Indeed, in a general picture where almost all dopants diffuse interacting with vacancies, boron seems to be quite different. Nonetheless, its much lower diffusivity has hampered any detailed study to shed light on it. In our work, we propose a new approach based on the study of B diffusion in Ge under light ion irradiation. In particular, thanks to the defects produced during implantation B diffusion is promoted, allowing to be experimentally investigated. In particular, the dependence of B diffusion on the fluence, the flux and the temperature of the implants has been expounded and quantitatively analyzed by a proper simulation model able to obtain the main diffusion parameters (e.g. diffusion rate, diffusion length). This study, compared with B diffusion in thermal equilibrium or during the evolution of the interstitial-type defects produced by amorphizing implants, allowed to definitively evidence the role of interstitials in B diffusion and the energies involved in the related diffusion mechanism.

In Chapter 3 the results obtained in the previous chapter on the interstitial mediated mechanism of B diffusion in Ge were exploited in order to monitor the concentration and the spatial distribution of point defects in Ge. Indeed, to control point defects is of fundamental importance in the device production steps, because they are responsible, among other things, of the dopant diffusion and precipitation. A new way to perform point defect engineering in Ge is presented in this chapter. We have performed O implants in Ge to produce GeO_2 precipitates. The possibility to create GeO_2 clusters embedded in a Ge matrix overcame the problems related to the instability of the germanium oxide. Moreover, due to the different densities, the GeO_2 clusters induce stress in the lattice, that can be released, during their thermal evolution, by injecting interstitials through the matrix. The original results reported in Chapter 3 open the way to get a significant change in the basic properties of crystalline Ge, usually dominated by vacancies, that can be exploited in the device design.

The last chapter (Chapter 4) is dedicated to the new perspective to use Ge as an active medium in order to realize a Si-compatible light source. To do this, several methods have been tried. Our innovative approach is based on the use of a highly Sb doped Ge layer as a virtual substrate for tensile strained Ge, where both strain and doping would be simultaneously employed to properly engineer Ge bands to obtain light emission. In particular, in this chapter, the preliminary studies related to obtain a very high concentration of Sb in Ge are reported. As far as this point is concerned, the use of laser annealing as alternative process to conventional thermal annealing allows to incredibly increase the Sb incorporation and electrical activation in Ge. A detailed structural and electrical analysis is hence reported, evidencing the possibility to obtain Sb active substitutional concentration (~$1\text{x}10^{21}$) higher than those ever obtained before, much higher than the solid solubility limit in Ge. Moreover, original results on damage recovery, high substitutional and active Sb concentration and thermal stability of Sb in Ge are discussed. These results open the way for a real application of Ge for Si-compatible light emitting devices.

---

1. E.E. Haller, Mat. Sci. Semicon. Proc. **9**, 408 (2006).
2. R.W. Cahn, Nat. Mater. **1**, 3 (2002).
3. R. Bray, *The origin of semiconductor research at Purdue*, Purdue University Physics Department Website: http://tesla.physics.purdue.edu/about_us/history/semi_conductor_research.shtml .
4. U.S. Patent 2,402,661.
5. U.S. Patent 2,402,839.
6. U.S. Patent 2,441,603.
7. S.M. Sze, *Semiconductor devices: pioneering papers* (World Scientific Publishing Co., Singapore,1991).
8. U.S. patent 879,532.
9. W.B. Shockley, J. Bardeen, W.H. Brattain, Nobel lectures, Physics 1942–1962. (Elsevier, Amsterdam, 1964).

10. C. Claeys, E. Simoen, *Germanium-based technologies – from materials to devices* (Elsevier, Great Britain, 2007).
11. G.K. Teal, J.B. Little, Phys. Rev. **78**, 647 (1950).
12. J. Kilby Nobel lectures, Physics 1996–2000. (World Scientific Publishing Co., Singapore, 2002).
13. K. Prabhakaran and T. Ogino, Surf. Sci. **325**, 263 (1995).
14. J.S. Kilby, IEEE Trans. Electron Dev., **23**, 648 (1976).
15. http://www.intel.com .
16. International Technology Roadmap for Semiconductor, 2009 Edition, PROCESS INTEGRATION, DEVICES, AND STRUCTURES.
17. J. R. Haynes and N. G. Nilsson, Proceedings of VIIth International Conference on Physics of Semiconductors, (Paris: Dunod, 1964).

Chapter 1

Germanium for micro and optoelectronics

This chapter presents an overview of the main properties of germanium as a material to improve micro and optoelectronic devices.
Germanium was the first element used to realize microelectronic devices. Indeed, the first transistor was created in 1947 on a Ge substrate. Subsequently, several problems principally related to the instability and low quality of germanium oxide lead to a slow abandon of this semiconductor in favor of Si. Nonetheless, recent advantages on high-k materials to be used in Metal Oxide Semiconductor (MOS) structures overcome the issues related to germanium oxide. Then, the high charge carrier mobility or the particular band-gap structure, together with the high compatibility with the already existing Si-based technology, have lead during the last years to a renewed interest towards Ge. With this in mind, in paragraph 1.1 the principal similarities and difference between Ge and Si are analyzed pointing the attention to the advantages of Ge over Si, as for example, Ge higher carrier mobility that can be useful in order to realize new generation microelectronic devices with very high performances. However, in order to realize micro and optoelectronic devices a crucial point is represented by doping. In this process several aspects, such as diffusion, electrical activation and precipitation must be taken into account in order to opportunely design the devices. A brief review on these aspect is presented in paragraph 1.2. Furthermore in paragraph 1.3 the crucial points necessary to realize a Ge-based light emitting device are analyzed engineering Ge bands structure by applying strain ad n-type dopant. Finally, paragraph 1.4 points out those aspects unclear and on which the experimental study of this thesis is focused.

1.1 Ge *vs* Si : similarities and differences

A deep knowledge of chemical and electrical properties of semiconductors is of fundamental importance to create and improve electronic devices. From this point of view, the knowledge of the Si properties and the behavior of foreign atoms in the Si matrix stems from more than 50 years of study and research. During the last decades, indeed, Si has been the most investigated element of the periodic table of elements and has become the base of the whole electronic industry. The Si supremacy is principally due to three important properties. The first regards its abundance and then a low cost, indeed Si is the second most abundant element in the Earth's crust only after O, with a percentage of 27.72%. The second concerns the stability of SiO_2, which protect device surfaces and acts as an effective mask in device manufacturing. The third, instead, is the extremely low surface state density at Si/SiO_2 interface. It is the latest property which allows millions of metal-oxide-semiconductor field effect transistors (MOSFET) to be built simultaneously on a Si wafer. Unfortunately, nowadays the shrinking of microelectronic devices led to the achievement of the physical limit in SiO_2 dimension below which currents due to tunneling effect increase drastically, leading to higher power consumption and reduced device reliability. For this reason several studies on new materials with high dielectric constant (high-k) have been performed in the last years. Replacing the SiO_2 with a high-κ material allows to increase gate capacitance without the concomitant leakage effects. On the other hand, the progressive device shrinking is leading also to the achievement of the physical limit of scalability of Si. For this reason, in order to scale CMOS (Complementary MOS) to and beyond the 16 nm technology generation it is necessary to develop new materials to replace silicon to create alternative channels and source/drain regions. This is of fundamental importance in order to increase the saturation velocity and maximum drain current in MOSFETs while minimizing leakage currents and power dissipation [1]. One approach is to replace the strained silicon MOSFET channel (and the source/drain regions) with an alternating material offering a higher potential quasi-ballistic-carrier velocity and higher mobility than silicon. A very good candidate material in this respect seems to be Ge. It must be noted, however, that the knowledge on Ge properties and on the behavior of foreign atoms in Ge is still incomplete because the studies on this semiconductor was almost completely abandoned in the early ‘60s in favor of Si mainly because the Ge oxide is particularly unstable. In this respect, the high-k materials developed recently, compatible with Ge, eliminate problems due to germanium oxide opening a new way in the microelectronic industry and a renewed scientific interest on Ge. In fact, Ge is characterized by better electrical and optical properties than Si, like the carrier mobility well higher than Si or the characteristic quasi-direct band-gap. Moreover also the high compatibility with the already existing Si-based technology, make Ge one of the most promising materials for the realization of future ultra fast and highly efficient electronic and optoelectronic devices. Nonetheless, many points of the Ge behavior are still unclear and need to be understood for its successful use and integration. In this chapter, a review of the main properties of Ge is reported, starting from its similarities and differences with Si and hence the high potentiality of this material, that can be exploited in the realization of micro and optoelectronic device with ever high performance.

1.1.1 Crystalline configurations and band structures

One of the most important characteristics that nowadays makes Ge an attractive material in order to improve micro and optoelectronic devices is its high compatibility with the currently used Si-technology. This stems from the similarities of these two semiconductors that makes it possible to use for Ge the same production steps already used for Si tecnology. It is well known, indeed, that Si and Ge have the same crystalline structure: the diamond structure [2]. As illustrated in Fig. 1.1, this kind of structure can be considered as two interpenetrated face-centered cubic (FCC) lattices and it is characterized by the lattice parameter represented in Fig. 1.1 with the symbol *a*. It is known that *a* is related to the atomic radius of the constituent element [3] and so it differs for each material. In particular, the lattice parameters experimentally obtained for Ge and Si are 0.5657 nm and 0.5431 nm respectively [3]. The relatively small lattice mismatch (~4%) allows, for instance, to have Si and Ge within the same device (producing SiGe alloys or Si/Ge/SiGe heterostructures), where both Si and Ge are located in substitutional position within the sites of the FCC structure. These similarities are also reflected in the main p- and n-type dopant behavior in both the semiconductors, that for example are substitutionally dissolved through the matrix and need to interact with native defects to go out from their sites and diffuse as will be described in the next section. Also as far as the bond structures are concerned many similarities are present.

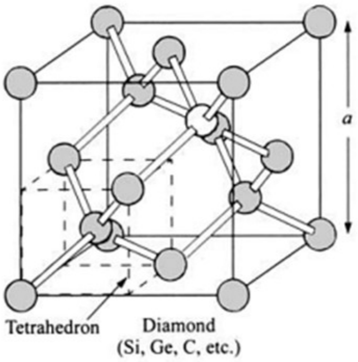

Fig. 1.1 Primitive cell relative to the diamond lattice characteristic of Si and Ge crystals. In this configuration each atom is bonded with other four identical atoms placed at the corner of a tetrahedron. The lattice constant of the cell is indicated with *a*. [2]

The band structures obtained with the k • p method for Si and Ge are represented in Fig. 1.2 (a) and (b), respectively [4]. In particular it can be noted that for both Si and Ge there is a forbidden energy range in which allowed states cannot exist evidenced by a red strip in Fig. 1.2. The energy value of the gap is characteristic of each structure, and in particular it assumes a value of 1.12 eV and 0.8 eV in Si and Ge, respectively.

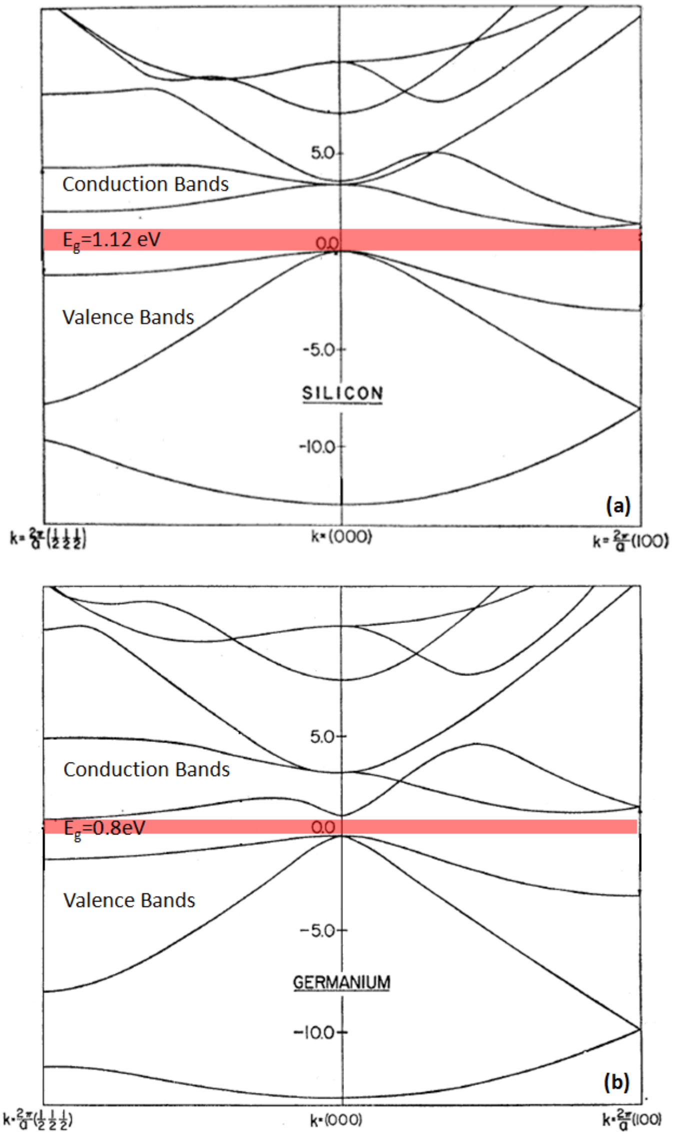

Fig. 1.2 Representation of the E-k relation of Si (a) and Ge (b) calculated by the k•p method.

The energy regions permitted above and below this energy gap are called the conduction bands, and valence bands, respectively. It can be noted that the upper limit of valence band occurs at k=0, instead the bottom of the conduction band occurs at k≠0 for both Si and Ge, so they are classified as indirect band-gap semiconductors.

1.1.2 Carrier mobility

Electrons and holes in semiconductors can be considered as quantum mechanical waves propagating through the solid under the influence of the crystal, applied and scattering potentials. Nonetheless, when the scale of the device is large enough, the charge carriers can be treated much as a classical particle. As one applies an electric field ε to a semiconductor, the electrostatic force causes the carriers to first accelerate and then reach a constant average velocity called drift velocity $|\boldsymbol{v}_{drift}|$ in the direction of the electric field. The ratio of the velocity to the applied field is known as mobility: $\mu = \frac{|v_{drift}|}{\varepsilon}$. Despite this, the carriers inside the crystal do not follow a straight path because they constantly collide both with defects (as neutral or ionized impurities or dislocations inside the crystal) and with lattice vibrations (as optical and acoustic phonons). These carrier scattering are the result of short-range forces and must be quantum mechanically treated. It is known that for both Ge and Si, the presence of acoustic phonons and ionized impurities results in the carrier scattering processes that most significantly affects the mobility [2]. Fig. 1.3 shows the dependence of carrier mobility on the impurity concentration in Ge and Si at a fixed temperature of 300K [2]. It can be immediately noted that both electron and hole mobilities are well higher in Ge with respect to Si. This is due to the fact that the effective mass is strictly connected to the E-k relationship through the relation:

$$\frac{1}{m^*} = \frac{1}{\hbar^2}\frac{\partial^2 E(k)}{\partial k^2}$$

Eq. 1.1

The different curvature of the energy bands in Ge with respect Si induces a lower m* for electrons and holes in Ge resulting in higher carrier mobility compared with the ones in Si.

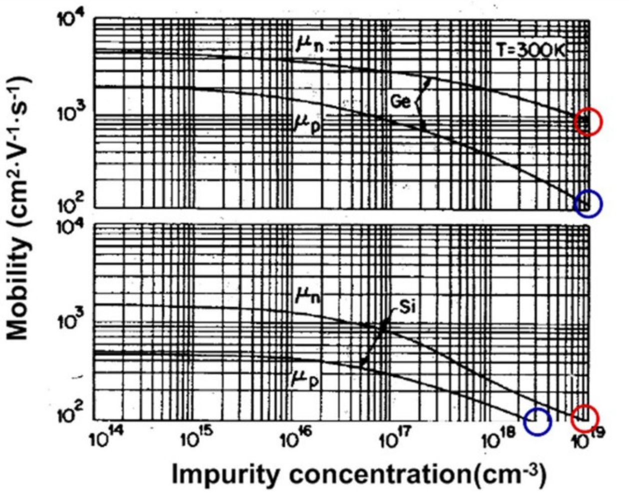

Fig. 1.3 Impurity dependence of electron (μ_n) anh hole (μ_p) mobility in Ge (upper graph) and in Si (lower graph) [2].

For example at a doping level of about ~10^{15} at/cm^3 it can be noted that the electron mobility is more than two times higher in Ge than in Si, and even in the case of hole mobility Ge value is more than four times higher than in Si. This feature is important in microelectronics because conductivity is proportional to the product of mobility and carrier concentration. These values hence emphasize that Ge will be better than Si in order to fabricate new generation high speed microelectronics devices with high mobility channels. These aspects, indeed, are recently becoming more important because in conventional Si channel devices the saturation trend of the on-current is going to be reached due to the increase in substrate impurity concentration near the source region caused by high dopant implantation. As far as this point is concerned Ge higher mobility can lead to increase drift velocity near the source region, without the need of extremely high doping level, which is essential to the increase of the on-current. Furthermore, Ge higher mobility can lead to the higher carrier velocity even in short channel devices [5]. In this respect, many research groups have already used Ge as a substrate for microelectronic devices in order to take advantage of its properties. As an example, recently Le Royer et al. [6], have reported for the first time the fabrication and electrical operation of a Ge and Si based CMOS planar scheme with Ge On Insulator (GeOI) p-Field Effect Transistors (FETs) and Silicon On Insulator (SOI) n-FETs, taking advantage of the best mobility configuration for holes in Ge and electrons in Si. In Fig. 1.4 indeed, the measured mobility values of electrons and holes in the SOI and GeOI dices are summarized. It confirms that the best holes/electrons mobility configuration is obtained with Ge for holes and with Si for electrons (180 and 375 cm^2/Vs respectively)[7].

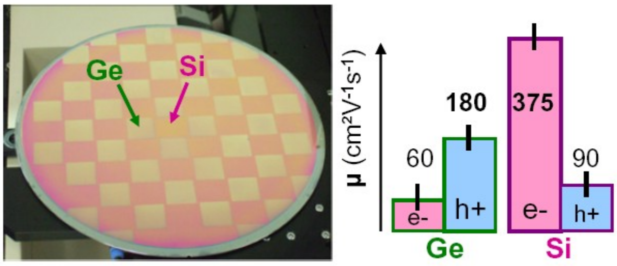

Fig. 1.4 On the left: picture of the 200 nm Si substrate after local Ge enrichment. On the right the corresponding electron and hole mobility values of Ge and Si Metal-Oxide-Semiconductor Field Effect Transistors[6].

Although high hole mobility in pFETs has been demonstrated by many research groups [8,9], electron mobility in nFETs is not very good in spite of high electron mobility in bulk Ge. This is due principally to the density and distribution of interface traps on the Ge/gate interface and also to the low activation level of n-type dopants in Ge.

Understanding and properly controlling the doping processes is a crucial point also as far as the device size is concerned, since dopant diffusion and hence dopant profile broadening hamper the creation of ultra shallow junction in devices fabrication steps. Nevertheless, the knowledge about the basic properties of defects and dopants diffusion, of fundamental importance in engineering Ge, are limited due to the fact that the studies on it was almost abandoned in early ‘60s in favor of Si, as already said. Furthermore, the oldest studies are often incomplete because of the lack of many experimental techniques developed subsequently. So, many open points are still present in the comprehension of the various mechanism involved, like, for example, B diffusion or Sb incorporation and electrical activation both in equilibrium and non-equilibrium processes. However an overview on the data present in literature on incorporation, diffusion and electrical activation of dopants will be done in the next sections, emphasizing the topics for which further studies are necessary.

1.2 Doping of Ge and related issues

As previously observed, a full comprehension of the dopant behavior in Ge is of fundamental importance to successfully use Ge for both micro and optoelectronic devices.

It is well known that in order to modulate the charge carrier concentration inside a semiconductor (crystalline Ge in our case) is it necessary to introduce doping species such as B, Ga, P or Sb. Ion implantation is the most commonly used technique to introduce dopants. Nonetheless, the passage of an energetic ion through the lattice initiates a sequence of displacement events that produce defects within the crystal. Furthermore these defects can heavily affects the dopant behavior as it will described in the following. Thus it is important to understand how they are produced and how they interact with dopants, making them diffuse or precipitate, not only during the doping themselves but also during the subsequent thermal annealing aimed to eliminate the implant damage and electrically activate the implanted dopants. For this reason this section will try to give a vision as comprehensive as possible of the data presents in literature on the diffusion and activation mechanisms of dopant in Ge and the role that defects can have in it.

1.2.1 Native point defects

A point defect in a crystal is represented as a variation of the lattice periodicity. The two basic types of intrinsic point defects are called vacancies (*V*) and interstitials (*I*) and are depicted in Fig. 1.5. A vacancy is a lattice site with a missing atom, while self-interstitials are atoms of the matrix that lie in positions that differ from the lattice sites. The vacancy-interstitial pair is called Frenkel defect.

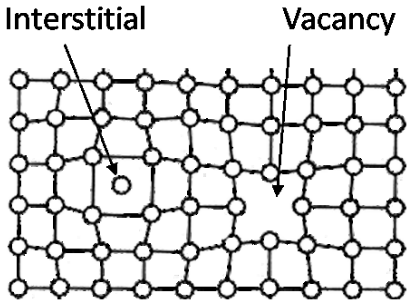

Fig. 1.5 Scheme of intrinsic defect in a semiconductor matrix.

The defects just mentioned are called native defects because they are always present inside a real crystal above the absolute zero temperature for thermodynamic reasons. In fact, their presence lowers the Gibbs free energy of the system with respect to a defect-free crystal. The formation of N_x defects (where the subscript *x* indicates *V* or *I*) induces a free energy variation that can be written as [10]:

$$\Delta G = N_x G_x^f - k_B T \ln \frac{N!}{N_x!(N-N_x)!}$$

Eq. 1.2

where *N* is the number of lattice sites of the considered crystalline cell, k_B is the Boltzmann constant and $G_x^f = H_x^f - T\Delta S_x^f$ represents the Gibbs free energy related to the defect formation that can be considered as the sum of the formation enthalpy H_x^f (associated to the lattice distortion) and the formation entropy ΔS_x^f (associated to the lattice vibrations).

Minimizing Eq. 1.2 with respect to the number of intrinsic defects, the equilibrium concentration of defects can be found:

$$c_x^{eq}(T) = A\exp\left(\frac{-G_x^f}{k_B T}\right) = c_x^0 \exp\left(\frac{-H_x^f}{k_B T}\right)$$

Eq. 1.3

where the constant *A* is related to both the lattice sites and the degrees of internal freedom of the considered defect.

Furthermore, thermal excitation not only induces the formation of point defects, but also it allows such defect to move inside the lattice host. The diffusion coefficient, or diffusivity (D_x), is universally defined by the Fick's law $J_x = -D_x \frac{\partial c_x}{\partial x}$ as the proportionality factor between the flux (J_x) and the concentration gradient ($\frac{\partial c_x}{\partial x}$). So, the equilibrium diffusion coefficient for point defects could be expressed as follows:

$$D_x = g_x a^2 \upsilon_x exp\left(\frac{-G_x^m}{k_B T}\right)$$

Eq. 1.4

where, g_x is a geometry factor depending on the crystal structure ($g_I = 1/4$ and $g_V = 1/8$ for interstitials and vacancies in a diamond lattice, respectively), a is the Ge lattice constant, υ_x is the attempt frequency ($\upsilon_x \sim 10^{13}\ s^{-1}$), and finally $G_x^m = H_x^m - T\Delta S_x^m$ is the Gibbs free energy related to the defect migration being H_x^m and ΔS_x^m point defects migration enthalpy and entropy, respectively.

It is well known that the behavior of microelectronic devices is strongly influenced by the presence of point defects in the substrate [11,12], so the study of their formation and diffusion energies is of fundamental importance in order to suitably design the production steps of devices.

In this regards first-principle calculations based on density functional theory [13-17], molecular dynamics calculations based on empirical interatomic potentials [18-22], and ab initio calculations, provide valuable information about formation and migration enthalpies of thermodynamically stable defects. In particular, an overview of recent theoretical results is given in Table 1.1.

H_V^f [eV]	H_V^m [eV]	H_I^f [eV]	H_I^M [eV]	References
Molecular dynamic simulation				
2.46	0.4	3.41	0.87	[22]
2.21	0.38	2.97	0.76	[22]
2.06	0.28	2.92	0.62	[22]
Density functional theory				
2.56		3.5		[16]
2.6	0.4			[17]
ab initio				
2.56	0.25	3.50		[23]

Table 1.1 Formation and migration energies (in eV) for vacancies and interstitials, obtained, through molecular dynamic simulation, density functional theory and ab-initio calculations.

As can be seen from Table 1.1, the calculated migration enthalpies for both vacancies and interstitials assume values generally less than 0.4 eV and 0.8 eV, respectively. This means that once generated, vacancies can migrate easier than interstitials inside the crystal. Furthermore, it can be seen that H_V^f is always lower than H_I^f. This means that in equilibrium conditions the vacancy concentration in Ge is higher than the interstitial one. Regarding this, several experimental studies have confirmed that the greater number of vacancies present in Ge over all temperatures is decisive in dopants behavior [12, 24, 25]. This feature has also hampered experimental studies on interstitials in Ge because they are based on an indirect approach that analyze defect behavior by monitoring dopant diffusion. Knowing that in Ge almost all dopants diffuse through a mechanism mediated by vacancies, as will be described in the next section, the values on formation and migration enthalpies experimentally obtained are available only for vacancies, as reported in Table 1.2.

H_V^f [eV]	H_V^m (eV)	References
Experimental		
2.01	1.08	[26,27]
2	1	[28,29]
1.9	1.2	[30]
1.9		[31]
	0.2	[32]

Table 1.2 Vacancy formation H_V^f and migration energies H_V^m (in eV) experimentally measured.

However, to obtain experimental information on interstitial equilibrium concentration is a crucial point that needs to be deepened studied in order to better understand also the behavior of those dopants whose diffusion, segregation and precipitation microscopic mechanisms are less known yet.

1.2.2 Dopants diffusion mechanisms

After knowing what kind of defects are present in Ge, it is important to know how they can affect dopant behavior. Experimental and theoretical studies performed on dopant diffusion in Ge, have demonstrated that the comprehension of the dopant diffusion phenomenon is more complex than that described by the Fick’s law and driven only by dopant concentration gradient [3]. Indeed, dopants diffusion involves mechanisms in which point defects play a key role. In this perspective, Fig. 1.6 shows the indirect diffusion mechanisms of an external element A inside a crystalline lattice like Ge [33].

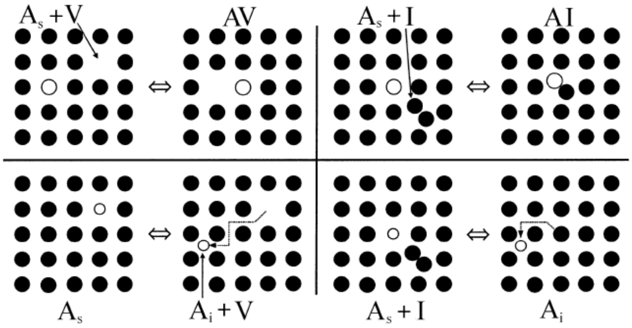

Fig. 1.6 Schematic bi-dimensional representation of indirect diffusion mechanisms of an element A in a crystal. In the figure, are indicated with *V* and *I* the vacancy and interstitial defects; Ai and As represent the foreign atom placed in an interstitial or in a lattice site respectively, instead AV and AI represented the species formed when the foreign atom A binds with a point defect (*V* or *I*) [33].

The diffusion of a substitutional impurity A_s is very often mediated by point defects and the possible mechanisms involved, illustrated in Fig. 1.6 , can be schematized in [33]:

1) $A_s + V \Leftrightarrow AV$
2) $A_s + I \Leftrightarrow AI$
3) $A_s \Leftrightarrow A_i + V$
4) $A_s + I \Leftrightarrow A_i$

The first two mechanisms occur when a vacancy or an interstitial joins together with a substitutional impurity creating a diffusing species (AV or AI). This process occurs because the pairing is favoured by Coulomb interaction or lattice deformation minimization. In the first case diffusion occurs with a partial dissociation of the AV pair, conversely the AI pair must bond in order to diffuse.

The relations 3) and 4) are named Frank-Turnbull and kick-out mechanism, respectively. They describe the diffusion behavior of elements that are mainly dissolved on substitutional sites as before, but that move as interstitial defects. It is not possible to determine *a priori* the diffusion mechanism of an element. For this reason over the years, there have been many experimental [34-42] and theoretical [43-50] studies to achieve a good comprehension about the mechanisms involved in dopant diffusion under equilibrium and non-equilibrium conditions.

In Ge quite all dopants diffuse through a mechanism mediated by vacancies [24, 51-53]. Indeed, as previously observed, vacancies are dominant over interstitial in Ge [23]. This is supported also by the binding energies between vacancy and different dopant atoms, calculated on the basis of the generalized gradient approximation, reported in Table 1.3 [45,46]. In particular, the binding energy is defined as $E_b = E_{cluster} - \sum E_{isolated\ defect}$, so the negative values of binding energies implies that the AV pair is stable for P, As and Sb, with respect to its constituent point defect components. Furthermore, as can be noted, the stability of AV cluster increase with the atomic radius of the dopant. This behavior can be explained considering that bigger foreign atoms induce a tensile stress inside the lattice that can be reduced by a vacancy.

	B	*P*	*As*	*Sb*
E_b [eV]	0.33	-0.52	-0.60	-0.70

Table 1.3 Calculated binding energy (in eV)for a foreign atom-vacancy pair in a Ge matrix [45,46]

The anomaly in Ge seems to be represented by B, as can be seen in Table 1.3. In this case, indeed, the BV pair is not stable, so a vacancy mediated B diffusion is unlikely.

For almost all the other dopants the diffusion mechanism can be depicted as following. When a vacancy encounters a dopant atom, the latter moves onto the vacant site and the vacancy is translated in the opposite direction. Such repeated exchanges, where the dopant and the vacancy simply swap place, do not lead to the net displacement of the dopant atom. For the displacement of a dopant through Ge, the vacancy must move away to at least the third nearest neighbor site and return along a different path, as represented in Fig. 1.7.

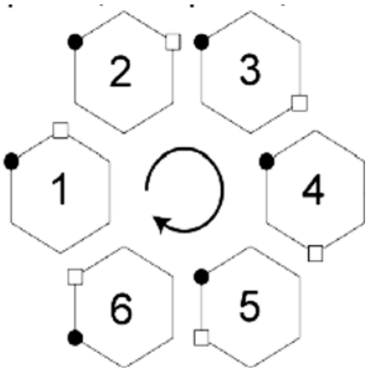

Fig. 1.7 Representation of the ring mechanism of diffusion for the AV pair, in which the dopant atom and the vacancy are represented as black circles and open squares, respectively

In an analysis of vacancy-mediated diffusion in Ge, Chroneos et al. defined the activation enthalpy of diffusion E_D as:

$$E_D = H_V^f + E_b + H_{AV}^m,$$

Eq. 1.5

where H_V^f is the vacancy formation enthalpy, E_b is the binding energy of the AV pair and H_{AV}^m is the greatest migration enthalpy barrier of a V near the dopant atom A, that is different to the bare migration barrier of an isolated V and was calculated for different dopants [46]. Comparing the calculated values for activation enthalpies with experimental results recently obtained (Table 1.4) it can be seen that they are in clear agreement.

Furthermore, the obtained values for activation enthalpy of P, As and Sb are consistent with the trend experimentally observed that evidences a decreasing in E_D increasing donor size. These results confirm that donor diffusion in Ge is mediated by vacancies differently from B for which the measured activation enthalpy of diffusion in Ge (~4.65 eV [39]) is incompatible with E_D calculated by Eq. 1.5.

Defect complex	E_D *calculated [eV]*	E_D *measured [eV]*
PV	2.98	2.85
AsV	2.64	2.71
SbV	2.41	2.55

Table 1.4 Predicted activation enthalpies E_D for impurity diffusion via a vacancy mediated mechanism, compared to results from SIMS analysis of impurity diffusion profiles obtained in [47].

The dopant diffusion process is than strictly related to the defect concentration inside the lattice, so a deep knowledge on damage induced during dopant implantation is of fundamental importance in order to understand the better solution for device fabrication processes. A large discussion on these aspects is presented in the next section.

1.2.3 Damage generation in Ge and related effects on doping

As said before, ion implantation of dopant elements in Ge is relevant for the application of this material in high-mobility MOS devices. In the process of ion implantation each ion, during its slowing down, interacts anelastically with electrons and elastically with the other target atoms. If the kinetic energy transferred to the host atoms is higher than their threshold displacement energy, the knock-on atom leaves its lattice site and, according to the residual kinetic energy, can move for a certain path length [10]. The total of all such displacement events is commonly referred to as the collision cascade of the ion and it is able to produce defects inside the implanted matrix. Since defects strongly affect dopant behavior (e.g. diffusion, precipitation and electrical activation) understanding how implantation damage in Ge depends on the implanted ion mass and then how it interacts with the implanted dopant themselves is of fundamental importance. Furthermore, the relative softness of Ge with respect to Si [54] is an issue when processing is performed using standard Si-compatible equipment. For this reason a careful study on implant induced damage is of fundamental importance in this matrix.

It was found that the heavier is the implanted atom the more defects are generated [10]. In this respect a light atom such as B, even if implanted at a fluence of $3x10^{15}$ B^{+}/cm^{2} creates only an extended damage inside the crystal, with only small amorphous regions alternating with crystalline zones, as shown by the cross sectional transmission electron microscopy (XTEM) in Fig. 1.8 (a) [41]. Nonetheless in this case, low temperature annealing (400°C, 60 s) is sufficient to recover the Ge crystalline phase, although some residual defects, due to B precipitation, seem to remain. Moreover, Impellizzeri et al. observed that a residual damage persist also after post implant annealing at 550°C, 1 h [55]. On the other hand, if the B implant is performed at liquid-nitrogen temperature the ion damage is accumulated in the form of an extended amorphous layer since the dynamic annealing during the implantation at this temperature is essentially absent [55]. In this case, however, after a post-implant annealing at 360°C for 1 h a typical free-of-defects crystal can be observed with a ~95*%* and ~85*%* of B atoms substitutionally positioned in the samples implanted with $2.8x10^{15}$ and $7.6x10^{15}$ B^{+}/cm^{2}, respectively [55].

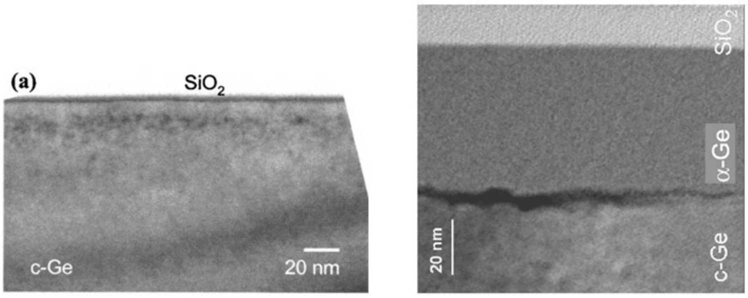

Fig. 1.8 Cross sectional Transmission Electron Microscopy micrographs of crystalline Ge implanted with $3x10^{15}$ at/cm^{2} of (a) B at 6keV [41], and (b) P at 25 keV [56]. It can be seen how the same dose leaves Ge in crystalline form in B case, instead generates a ~50 nm-thick amorphous layer in P case.

The creation of n^{+}-p junctions is more problematic due to the heavier mass of group-V dopants. In several cases, dopant implantation at room temperature creates by itself a continuous amorphous layer. As an example, Fig. 1.8 (b) shows XTEM of a Ge sample (with a 10-nm SiO_2 cap) implanted with $3x10^{15}$ P^+/cm^2 at 25 keV. It can be seen that an about 50-nm-thick amorphous layer is created by the implant. A similar damaging is induced in Ge by an implant of $3x10^{15}$ As^+/cm^2 at 50 keV [56]. In some cases the precipitation of impurities can also cause a retardation on the Ge regrowth [56-58], with consequences on dopant activation into the matrix.

Furthermore, the process of doping implantation leads to an increase in the surface roughness of the sample that is detrimental for the realization of Ge-based micro and optoelectronic devices because it creates a great number of surface defects that degrade device performances. Fig. 1.9 shows that there is a nearly linear relation between the root mean square of the surface roughness measured in Ge samples and the mass of the implanted ions [59].

A potential explanation for this roughness can be obtained considering the sputtering mechanism that occurs during implantation. So, in order to prevent surface roughness, dopant implantation is often performed in samples covered with a SiO_2 cap layer to protect the surface. In this condition, as shown in Fig. 1.9 (open circles), the surface rougness is almost completely eliminated. The only exception is represented by Sb [59].

Indeed, high dose Sb implantation not only leads roughening but also the formation of large subsurface structures of voids in a honeycomb pattern as shown in the image obtained by scanning electron microscopy in Fig. 1.10. This kind of structures have been observed in the past also for other heavy elements such as In, Bi, and Sn implanted in Ge at high fluence [60].

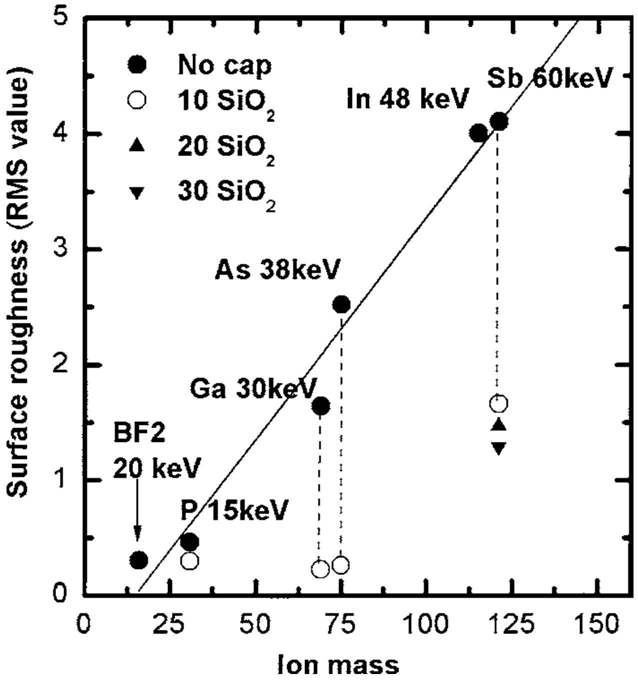

Fig. 1.9 Root mean square (RMS) surface roughness values determined with Atomic Force Microscopy after 3x10^{15} at/cm^2 implants of different ions in Ge without and with different thick $Si0_2$ cap[59].

Recently [61] the creation of this peculiar damage was attributed to the formation of voids in the early stage of implantation, followed by an effective cluster of vacancies beneath the surface at room temperature, with consequent void growth in the direction perpendicular to the surface. This is the reason why also in the case of Sb implantation in Ge through a SiO_2 cap the surface roughness persists. Moreover, the damage produced is so high that it is not recovered by any post-implant thermal annealing. This clearly limits the usefulness of Sb implantation for n^+-p shallow junction formation in Ge [58].

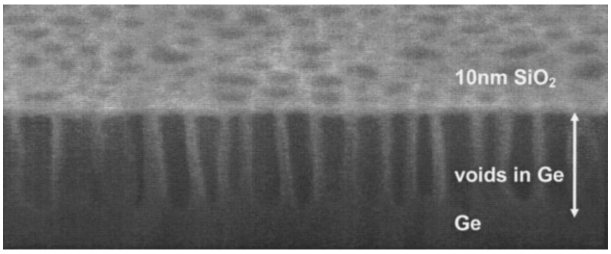

Fig. 1.10 Cross sectional Scanning Electron Microscopy of a Ge sample capped with 10 nm of SiO_2 and then implanted with Sb at 70keV at a fluence of $1x10^{15}$ Sb^{+}/cm^{2}. It can be seen the formation of a porous structure with a typical "honeycomb" pattern on Ge surface [59].

1.2.4 Electrical activation of dopants and related issues

After controlling damage generation during dopant implantation, in order to control the electrical properties of Ge and to realize micro and optoelectronic devices is it necessary to electrically activate the implanted dopants. Fig. 1.11 reports the maximum equilibrium solid solubility for the major dopant elements (closed squares) in Ge and the theoretical lower limit of the sheet resistance calculated (closed stars) from the solid solubility [56]. The experimental results are also shown in Fig. 1.11 (open stars). The differences between the theoretical and measured values that can be observed, are principally related to several issues due to the damage effects as will be detailed in the following.

First of all, in fact, it can be noted that the measured sheet resistance data are higher than the calculate ones (except for the B case). This implies a lower active dopant concentration with respect to the maximum equilibrium solid solubility. This is strictly related to the ion implantation damage [56]. Thus, damage removal is the key to achieve highly activated, low-leakage current junctions [63]. In this respect, indeed, the case of B is different from the other dopants because of its very light mass that reduce damage generation inside the matrix as discussed in the previous section.

Furthermore, B in Ge is the lowest diffuser [36, 39] and induces dynamic defect annealing and dopant activation already during its implantation [64, 65]. As a result, it has been demonstrated that after low dose B implantation in Ge at room temperature, full activation can be obtained without further thermal annealing [36]. In addition, several groups have demonstrated that after rapid thermal annealing (RTA) an active B concentration of 1x10^{19} B/cm^{3} can be achieved [38, 40, 41, 66].

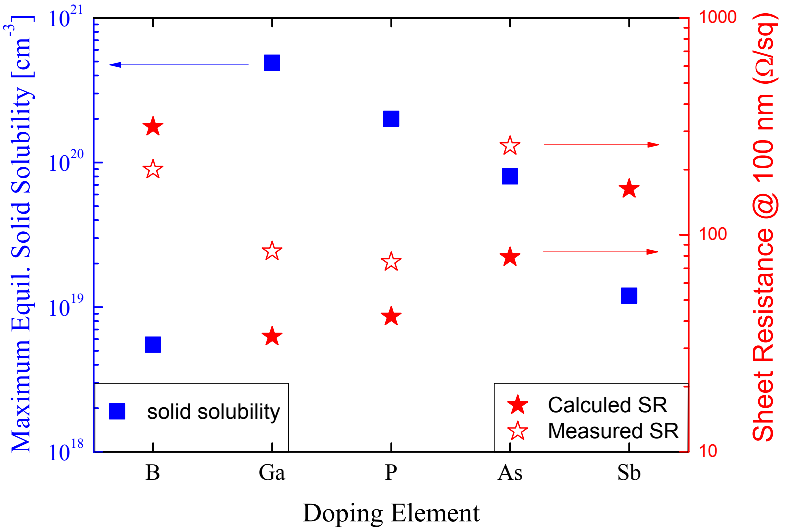

Fig. 1.11 Maximum solid solubility (blu closed squares, left scale) for the common doping elements in Ge [62] and calculated sheet resistance (red closed stars, right scale) corresponding with the junction depth around 100 nm. For comparison are plotted also the measured sheet resistance (red open stars, right scale) after 600°C 1 s rapid thermal anneal of samples implanted with fluencies varying from 1 to 5x10^{15} at/cm^{2} in order to obtain chemical concentration above equilibrium solid solubility[56].

A way to eliminate the crystal damage during implantation while avoiding any channeling effect that lead to undesired long tails in the implanted profiles, is to implant dopants in pre-amorphized Ge. This process is also useful in order to obtain a higher dopant activation during post-implant annealing inducing the solid phase epitaxial regrowth of the amorphous layer. As it is shown for example for B in Fig. 1.12 (open square), indeed, the active B concentration is higher than the solid solubility indicated with the red line. Moreover, Fig. 1.12 shows that with the use of Ge pre-amorphization implant (PAI) an even higher level of activation can be achieved (2.6×10^{20} B/cm^3 after a RTA at 650°C, 10 s) [67]. Concentration of active B up to 5.7×10^{20} B/cm^3 was subsequently achieved by optimizing implant and annealing parameters [68]. This is due to the fact that in the PAI samples, B atoms can be swept into substitutional lattice sites during epitaxial regrowth [63].

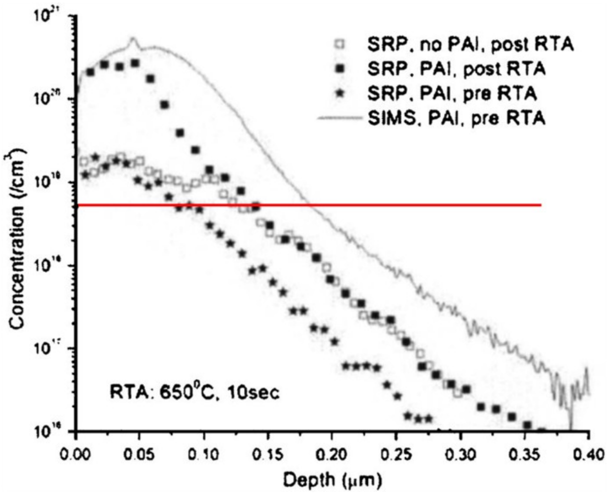

Fig. 1.12 Active dopant concentration obtained from Spreading Resistance Profilometry measurement of a Ge sample implanted with 20 keV 4×10^{15} B^+/cm^2 of B in crystalline Ge (open squares) and in pre-amorphized (PAI) Ge (closed square) after a Rapid Thermal Annealing (RTA) process of 10 s at 650°C. The B active profile before RTA process (closed stars) and the chemical B profile obtained by Secondary Ion Mass Spectrometry (continuous line) are plotted as a reference. The PAI is realized with a 1×10^{15} Ge^+/cm^2 Ge implant at 45 keV. The red line indicated the B solid solubility in Ge [62]. An order of increase of electrically activated concentration in PAI Ge sample with respect the no PAI one, is clearly shown [67].

More difficult is the realization of n^+-p shallow junctions in Ge done to their heavier mass that induce more damage than B, as said above. In this case, indeed the implantation of dopants creates an amorphous layer that could be advantageous in the electrical activation also without preamorphiation, but can cause also detrimental effects because, during the post implant annealing necessary to restore the sample crystallinity, dopant diffusion occurs hampering the realization of high doped ultra-shallow junctions (as seen in Fig. 1.11). Furthermore several problems derive also from the low solid solubility of n-type dopants in Ge.Moreover, in the case of P, that seems to be the best n-type dopant form Fig. 1.11, the out-diffusion plays also a significant role, making more difficult an high activation [38, 42].

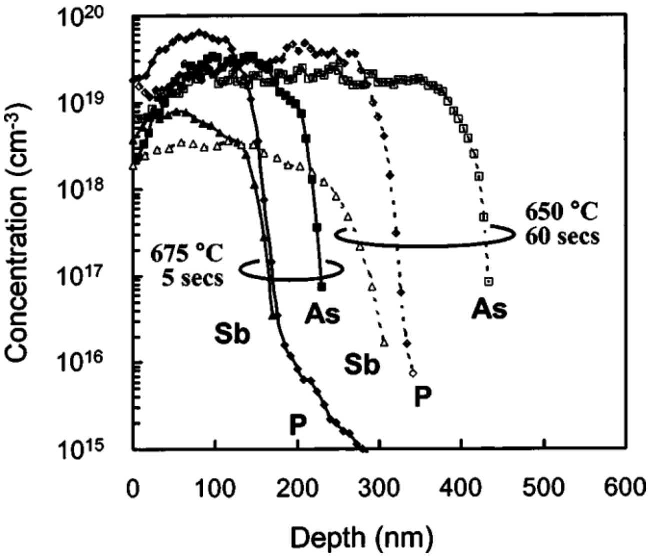

Fig. 1.13 Concentration of active dopant obtained by Spreading Resistance Profilometry of various n-type dopants in Ge after two different Rapid Thermal Annealing treatments (650°C 60 s and 675°C 5 s). The different n-type dopants were implanted in Ge with the same dose (4x10^{15} at/cm^2) and different energies corresponding to a similar projected range around 170-180 Å (18 keV, 30 keV and 45 keV for P, As and Sb respectively) [38].

In Fig. 1.13 the active concentration for P, As and Sb after two different RTA treatments are shown. It can be easily seen that, lowering the thermal budget, the dopant diffusion is reduced and so the active dopant concentration is increased favoring the realization of ultra shallow junctions [63]. The idea is that for short annealing times the donor atoms can reach a lattice position in the amorphous phase and become trapped there when the recrystallization front passes through [63]. Based on these observation it can be concluded that ultra-fast annealing can be successful in activating n-type dopants above the solid solubility. In spite of this in the case of Sb a very low active concentration was measured (more than 1 order of magnitude lower than the solid solubility) even after pre-amorphization. Moreover, in the case of Sb the high limit is principally represented by the vacancy clusters and porosity generated during high implanted dose, as discussed in the previous section. This feature has strongly hampered the use of Sb as a good dopant, limiting the active concentration obtainable in Ge.

1.3 Ge: optoelectronics perspectives

It is known that the light is the fastest way to exchange information. Thus a very important goal in new generation telecommunication system is represented by the realization a Si-based light emitter to be integrated within the electronic circuits. In spite of the fact that stimulated emission was predicted in 1917 by Albert Einstein in his famous paper “Zur Quantentheorie der Strahlung” (On the quantum theory of radiation) [69], the development of lasers started only in the early 1960s . In those years, indeed, the conditions of lasing action in semiconductors were also derived [70]. The characteristic indirect band-gap of Si and Ge have hampered up to now the realization of efficient light emitters with these materials, shifting the focus on III-V semiconductors that present a direct band-gap. Recently, a very large effort has been made in order to manipulate the Ge band structure in such a way to enhance the direct transitions and then the optical gain using both strain and n-type doping effects. This studies are very innovative and could lead to a new telecommunication era.

1.3.1 Light emission properties of Ge over Si

The possibility to obtain a Si-compatible laser for integrated silicon photonics has long been and it is still under study as it represents a turning point in the telecommunication field. However, it is known that energy bands similarity lead to classifying both Ge and Si as indirect band-gap semiconductors. This is related to the fact that in Ge as in Si the minimum of the conduction band and the maximum of the valence band occur at different k-values. This feature has a deep influence on their suitability use in light emitting devices. Indeed, it is well known that the luminescence from a semiconductor is generally the result of an electron-hole pair radiative recombination. Knowing that the photon momentum is negligible, its emission requires either direct transition or generation (absorption) of a phonon to conserve the momentum. It is clear, in fact, that a vertical transition in the k-space can occur in direct band-gap semiconductors (e.g. GaAs), in which the minimum of the conduction band and the maximum of the valence band occur at the same k-value as schematically illustrated in Fig. 1.14 (a). However, in the case of indirect semiconductors such as Ge and Si, radiative recombination requires a phonon as depicted in Fig. 1.14 (b). Since this becomes a three-particle interaction, the transition probability is significantly reduced, resulting in a radiative lifetime of about milliseconds in Ge and in Si (at 300 K) that is at least three orders of magnitude higher than the one characteristic of direct band-gap semiconductors [71].

Indeed the radiative lifetime is given by:

$$\tau_{rad} = \frac{1}{B(n_0 + \Delta n)}$$

Eq. 1.6

where n_0 is the dopant density for p-type or n-type materials, Δn is the injected carrier density and B the coefficient for radiative recombination that is of the same order of magnitude both for Ge and Si (B_{Si}=1.1x10^{-14}

cm^3/s, B_{Ge}=6.4 x10^{-14} cm^3/s at room temperature), more than three orders of magnitude lower than the one in direct gap semiconductors (e.g. B_{GaAs}=7.2x10^{-10} cm^3/s) [72]. This feature, similar in Ge and Si, prevents these two semiconductors to act as light emitters because the competitive nonradiative processes, such as Shockley-Hall-Reed recombination through deep traps or Auger processes, are characterized by shorter lifetimes ($\tau_{nonrad} \approx \mu s$) than the radiative one. In this respect, in order to increase the efficiency of light emission ($\eta = \frac{\tau_{nonrad}}{\tau_{rad}+\tau_{nonrad}}$) it is necessary either to reduce the radiative lifetime (τ_{rad}) or to increase the non-radiative lifetime (τ_{nonrad}).

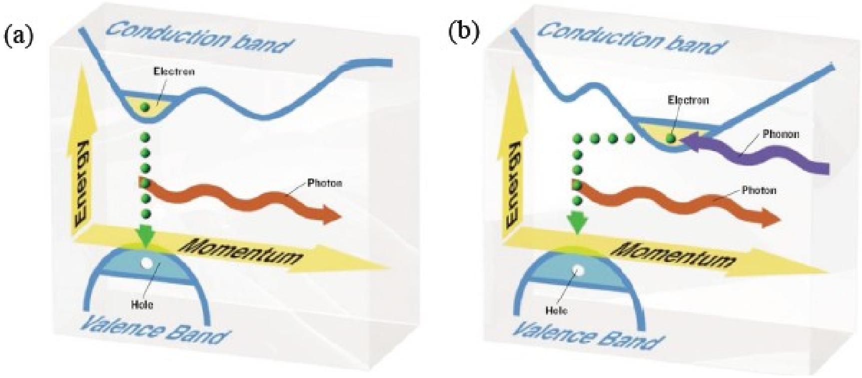

Fig. 1.14 Schematical representation of electron-hole radiative recombination in (a) direct and (b) indirect band-gap semiconductors.

Several methods have been exploited in the quest to get light out of silicon. Some 35 years ago Gnutzmann and Clausecker [73] conjectured that the Brillouin zone folding in thin layer SiGe superlattices, where the layer thicknesses were of the order of the unit cell dimensions, could result in a direct band-gap structure. The ability to grow Si$_m$Ge$_n$ superlattice (being the subscripts m and n the number of monolayers of Si and Ge, respectively) by molecular beam epitaxy [74], led impetus to this concept that was subsequently revised by theoretical studies [75]. It was observed, however, that although for certain Si$_m$Ge$_n$ superlattice periods direct energy gap is expected, the direct transition probability is still several orders of magnitude below that of direct band-gap semiconductors (e.g. GaAs) because the electronic properties of the band-edge states are not sensibly modified by the zone-folding. Thus, from a device point of view, it is most likely that these atomic layer superlattices find use as infrared detectors rather than as light emitters [76, 77].

Many other studies focused on low-dimensional silicon systems, such as porous silicon [78, 79], silicon nanocrystals [80], silicon/insulator superlattices [81], silicon nano-pillars [82], were performed in order to obtain a Si-based light emitter. In these kind of structures, indeed, quantum confinement effects occur due to the fact that electron/hole pairs are physically restricted to a small area (typically less than 30 square nanometers). This effect implies a band engineering that relaxes the problems related to the momentum conservation [83], increasing the probability that injected electrons will recombine with holes producing photons. Despite many studies have led to a possible role for silicon in photonic applications, yet a silicon injection laser remains difficult to obtain principally because the free carrier absorption cross-section still remains large enough to prevent net gain in light emission [84].

On the other hand, despite its indirect band-gap, Ge shows some peculiarities that makes it more promising than Si for optoelectronic applications, so attracting the attention of the scientific community. In particular, differently from Si, in Ge the direct optical transition is a very fast process with a radiative recombination rate five orders of magnitude higher than that of the indirect transition [85]. This means that the direct-gap emission of Ge is as efficient as that of direct band-gap semiconductors. The issue is that the injected electrons occupy preferentially the indirect valley characterized by lower energy states, as evident from the schematic of the band structure of bulk Ge reported in Fig. 1.15. However in Ge the difference between indirect and direct band-gap is of only 136 meV as can be seen in Fig. 1.15, much lower than in the Si case (880 meV).

So the idea of founding a method to overcome this small difference has attracted the interest of a lot of studies. Indeed, also noteworthy it is the fact that the direct band-gap of Ge is 0.8 eV, that is equivalent to a wavelength of exactly 1550 nm. This value corresponds to an minimum of attenuations in SiO_2 optical fibers [87, 88]. Therefore, it would be ideal to obtain light emission from the direct band-gap of Ge in order to implement it with the already existing Si-based technology.

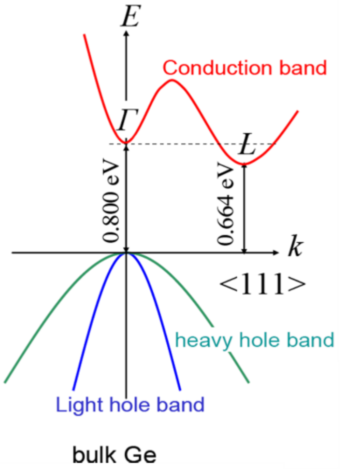

Fig. 1.15 Schematic band structure of bulk Ge, showing a 136 meV difference between the direct gap and the indirect gap. With the symbols Γ and L are indicated the direct and indirect conduction valley respectively [86].

To achieve this goal, it is important to enhance the direct recombination, properly engineering the band structure. Several studies have been performed in this field, principally based on strain effects and proper n-type doping of Ge, as will be discussed in the following.

1.3.2 Energy band structure engineering: strain effect

As discussed above, to obtain light emission from a semiconductor characterized by an indirect band-gap, such as Si or Ge is a great challenge. Indeed, several studies on band-gap engineering have been performed until the first ‘90s. In this respect Van de Walle [89] developed a theoretical model to predict the band offset in strained-layer. This theory is based on the local density functional pseudopotential formalism and the model-solid approach. In particular this method allows the generation of an accurate band structure and the alignment of this band structure to an absolute energy scale. The Van de Walle approach considers that applying a stress to a matrix, there is a variation in the volume of each unit cell. This variation causes a deformation in the periodic potential, that induces a variation in the energy bands. According to this theory, it was established that applying a tensile strain to the Ge matrix, the minimum of direct conduction valley (Γ) lowers faster than the indirect valley (L) [90-94] as illustrated in Fig. 1.16 with red and blue lines respectively. This leads to a transition of Ge from indirect to direct band-gap in correspondence of a tensile strain of about 2% (marked with a dashed black line in Fig. 1.16) and above.

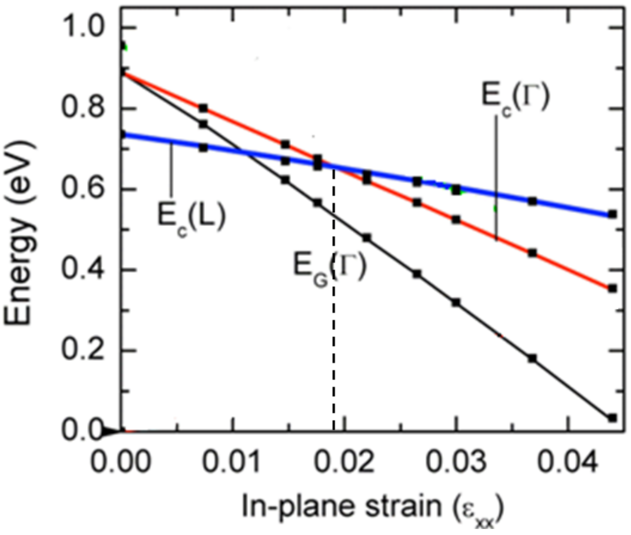

Fig. 1.16 Variation of the energy minimum of direct (Γ, red line) and indirect (L, blue line) conduction band valleys as a function of biaxial strain in Ge crystals. The variation of the direct band-gap energy $E_G(\Gamma)$ is also indicated (black line). The curves corresponding to $E_C(\Gamma)$ and $E_C(L)$ cross for a strain of 1.9%, which indicates the transition of Ge from indirect to direct band-gap [94].

It can also be noted from Fig. 1.16 that the variation induced by tensile strain causes a shrinking of the gap to the value of ~0.5 eV when Ge becomes a direct band-gap material. So, in this condition the light emission is at ~2500 nm, far away from the telecommunication standard wavelength of 1550 nm.

Different techniques have been used in order to obtain Ge strained but without reaching the value of 2%. In particular, a small tensile strain of 0.25% has been obtained by directly depositing relaxed Ge on Si and taking advantage of their different thermal mismatch coefficients [95-97]. Conversely, Bay et al obtained Ge tensile strained of about 0.5%, by epitaxially grown Ge on a material with a larger lattice constant as $In_{0.11}Ga_{0.89}As$ [98], while several studies have been performed also on the use of GeSn and SiGeSn alloys as virtual substrate [93, 99-101]. A third option is to apply mechanical external tensile stress to generate the required strain [102-106]. Nonetheless, even if the theoretical limit before fracture of about 2.7% was predicted [107], the maximum strain experimentally obtained by mechanical stress of Ge is around 0.7% [102].

Thus, considering both the difficulty to obtain such a high tensile strained Ge and the excessive shrinkage in direct band-gap, it is evident that an alternative approach must to be developed in order to obtain light emission from Ge.

1.3.3 Energy band structure engineering: n-type doping effects

An alternative way to theoretically induce direct recombination is based on n-type doping of Ge. Indeed, with heavy n-type doping, the excess electrons in the conduction band first fill the indirect (L) valley and after that they fill also the direct one (Γ), thus potentially promoting direct electron-hole recombination. The spontaneous emission spectrum for direct transition R_{sp} can be calculated considering the equation:

$$R_{sp} \propto \frac{1}{\tau_{rad}} f_c(h\upsilon)[1 - f_v(h\upsilon)]\alpha(h\upsilon)$$

Eq. 1.7

where, τ_{rad} is the radiative lifetime, $f_c(h\upsilon)$ and $f_v(h\upsilon)$ are the conduction and valence Fermi-Dirac distribution at room temperature and $\alpha(h\upsilon)$ is proportional to the absorption spectrum through the expression $\alpha(h\upsilon) = A\sqrt{h\nu - E_g^{\Gamma}}$, being $E_g^{\Gamma} = 0.8\, eV$ the Ge direct band-gap energy. The calculated emission spectra for undoped Ge (black line) and doped Ge with 2.6x10^{19} P/cm^3 (red line), 3.6x10^{19} P/cm^3 (green line) and 5.6x10^{19} P/cm^3 (blue line), are reported in Fig. 1.17 [108]. It is found that the spontaneous emission rates increase up to 30 times in this doping level range, which is consistent also with experimental results [108].

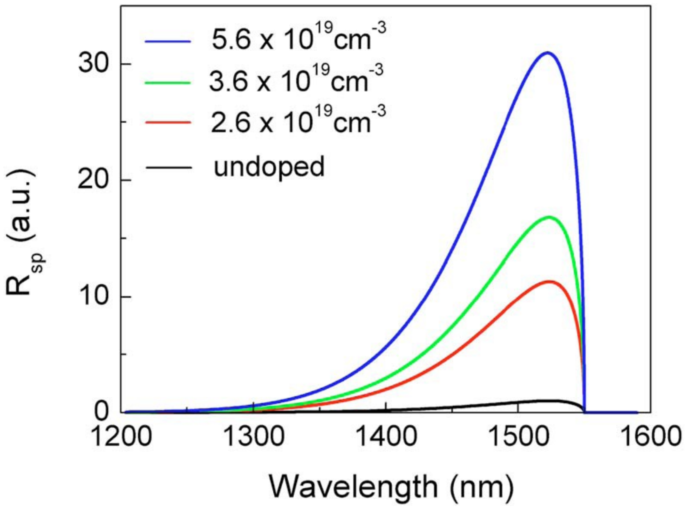

Fig. 1.17 Spontaneous emission spectra of undoped (black line) and *n*-doped Ge with donor concentrations of 2.6x10^{19} at/cm^3 (red line), 3.6x10^{19} at/cm^3 (green line) and 5.6x10^{19} at/cm^3 (blue line) at room temperature and for an identical excitation density, calculated through Eq. 1.7. The maximum of the undoped sample spectrum is set equal to one. [108]

So, with this approach it is possible to enhance the room temperature direct band-gap recombination of Ge, but at the same time the high free carrier absorption could cause some difficulties to achieve an electrically pumped laser. Also impurities themselves present within the Ge layers can have negative effects, since they can lead to charge carrier scattering phenomena. Anyway, this method is highly hindered by the low solubility limit of n-type dopants in Ge that hamper a complete shift of electron recombination from non radiative to radiative recombination in the direct valley.

It is worth noting that also doping causes a little shrinkage of the energy gap [72], but it is negligible with respect the one caused by strain effect. However the major limit that hampered the use of n-type doping in order to obtain Ge-based light emitter is principally due to the low dopant solubility.

The solution, to overcome the problems related to both strain and doping seems to be in joining the effects of little tensile strain with n-type doping as will be discussed in the next section.

1.3.4 Energy band structure engineering: strain and doping combined effects

As previously observed, the band-gap shrinkage obtained by applying strain in Ge can lead practical disadvantage in terms of emission wavelength. On the other hand, a moderate tensile strain of about 0.25% only shrinks the direct band-gap from 0.8 eV (1500 nm) to 0.76eV (1630 nm) which is still favorable in telecommunication transmissions. However in this configuration, Ge does not completely become a direct band-gap material. Therefore, additional effects are needed for efficient direct-gap light emission. In order to solve this problem, a proposed way is represented on n-type doping. In this way, as depicted in Fig. 1.18, the rest of the energy difference not compensated by strain, is compensated by n-type doping that makes it possible to fill electrons into the indirect valley (L) up to the level of the direct valley (Γ) [97, 103, 104].

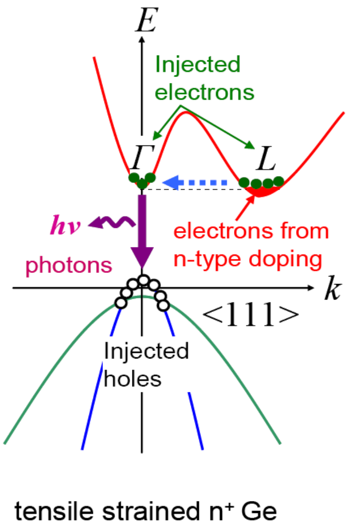

Fig. 1.18 Schematic band structure of Ge in which the difference between the direct and the indirect band-gap is partially decreased by tensile strain and partially compensated by filling electrons into the indirect band-gap [105].

The calculated equilibrium Fermi level as a function of active n-type doping concentration in a 0.25% tensile-strained Ge is showed in Fig. 1.19. It can be seen that the active dopant concentration for which the Fermi level position is equal to the minimum of direct valley is 7x10^{19} at/cm^3. So with this doping level nearly all energy states below the Γ valley minimum are occupied with equilibrium extrinsic electrons. This could make Ge to act as an effective direct band-gap material since it forces the injected electrons to occupy higher energy states with respect the Γ minimum, in both Γ and L valleys. Accordingly the injected electrons in the Γ valley are depleted much faster than the ones in L valley, since the radiative recombination rate of the direct transition in Ge is five orders of magnitude higher than the indirect one as discussed above [85]. So, to maintain the quasi-equilibrium of electrons in the conduction band, the electrons in L valley populate the Γ valley. This process results in further radiative recombination via efficient direct transitions.

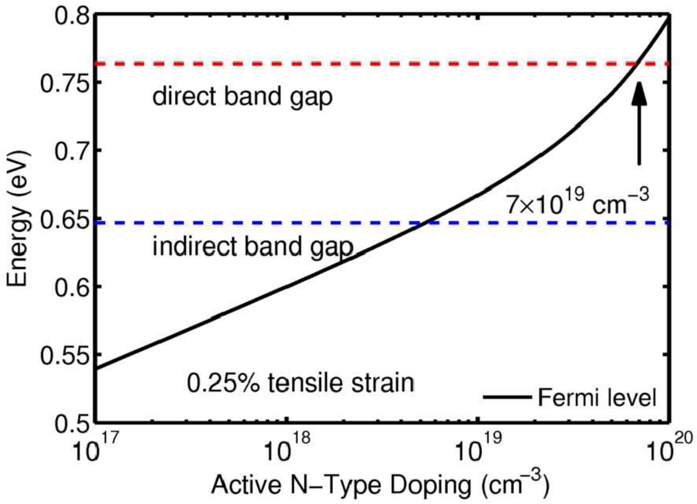

Fig. 1.19 Equilibrium Fermi level at room temperature as a function on active n-type doping concentration in 0.25% tensile-strained Ge. Choosing the maximum of valence band (light-hole band) as the zero energy reference, the energy values of direct (red dashed line) and indirect (blue dashed line) are also represented.

The results on tensile strained n-type doped Ge discussed above support the hypotesis that Ge is a very good candidate to realize a semiconductor laser compatible with Si-thecnology. In particular, the most recent effort on this field will be briefly discussed.

Indeed, recently Ge-based materials on Si have already been applied to advanced electronic devices such as high mobility CMOS transistors [109, 6], as observed above in section 1.1.1. Moreover, also integrated photonic devices such as waveguide-coupled photodetectors [110], electroabsorption modulator [111], and light emitting diode integrates with a microdisk cavity [112], that are CMOS compatible have been recently realized. In this landscape an high-performance Ge-on-Si light source makes it potentially possible the monolithic electronic-photonic integration process. In order to reach this goal great progress has been made in the last years.

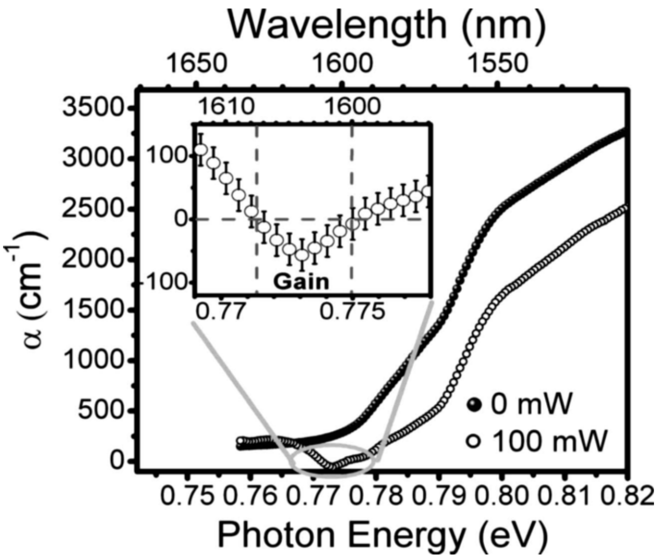

Fig. 1.20 Absorption spectra of the n-type doped Ge strained under 0 mW (closed circles) and 100 mW (open circles) optical pumping. The inset represent a zoom on the negative absorption coefficient, corresponding to optical gain observed in the wavelength range of 1600-1608 [114].

Thanks to this band-gap engineered Ge on Si materials, direct-gap photoluminescence [86, 97], and electroluminescence [113] at room temperature have already been demonstrated. Furthermore, Liu et al [114] have measured absorption spectra of *n*$^+$ Ge strained (0.23%) under 0 and 100 mW optical pumping. As can be observed by Fig. 1.20, negative absorption coefficients corresponding to optical gain are observed in the wavelength near the direct band-gap of the band-engineered Ge (1600-1608 nm), as also shown in the inset of Fig. 1.20 [114].

On the basis of this impressive experimental results a weak lasing action from the direct gap transition of Ge on Si at room temperature, using an edge-emitting waveguide device have been obtained [115]. The light emission spectra under different optical pumping level is shown in Fig. 1.21. It can be seen that for low pump power the emission shows a broad band typical of spontaneous emission. As pump power increases to 50 µJ/pulse, the widths of the emission peaks (at 1594 nm, 1599 nm and 1605 nm) decrease, that indicating a predominance of stimulated emission and so a lasing action.

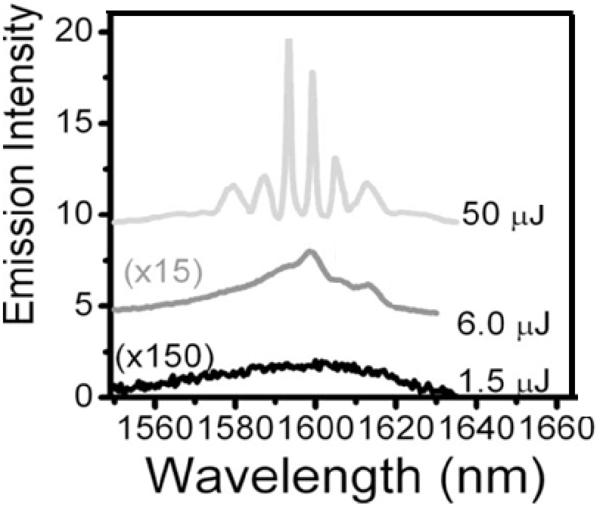

Fig. 1.21 Emission spectra of a Ge waveguide exited froma a 1064 nm Q-switched laser with a pulse duration of 1.5 ns and a repetition rate of 1 Hz. The spectra resolution is 2 nm. The three spectra at 1.5, 6 and 50 μJ/pulse pumping power correspond to the spontaneous, threshold for lasin and laser emission [115].

Nonetheless, in this kind of device a problem related to the very high pump power threshold (6 μJ/pulse) in order to obtain lasing action is present. This threshold is expected to decrease by increasing n-type doping [86], however this can lead to an enhancement of defect level that can contribute to non-radiative emission. This means that the doping related issues are very important in optoelectronics as in microelectronics. For this reason new approaches in order to obtain at the same time high level n-type doped and strained Ge are necessary in order to reach this important goal. All the studies presented above support the hypothesis that Ge is a very good candidate to realize Si-compatible laser.

1.4 Open points

As largely discussed above, in the last years germanium has acquired a renewed scientific interest thanks to its properties that makes it a very good candidate in micro and optoelectronics. This scientific interest is also testified by the large number of recent studies on this material that tend to shed light on numerous unclear aspects principally related to the diffusion and activation of dopants, very important both in microelectronic fields, and on the light emission property useful for optoelectronics. In this framework, the objective of this thesis is to understand some unclear points related to the diffusion of B and the incorporation and strain induced by Sb in Ge. The importance of these points is to be found, as discussed above, on the role that these dopants can have in improving micro and optoelectronic devices. First of all, B is the most used p-type dopant, but the mechanism of its diffusion inside Ge matrix is still unclear. This lack is especially related to the fact that B is a very slow diffuser in Ge. So, a systematic study in order to understand the microscopic mechanism of B diffusion has not yet been made. On the other hand Sb has a very large mass, and the formation of a porous structure during its implantation has hampered its use. A detailed study on the incorporation of this dopant is than more than necessary.

1.5 References

1. International Technology Roadmap for Semiconductor, 2009 Edition, PROCESS INTEGRATION, DEVICES, AND STRUCTURES.
2. S. M. Sze, *Physics of Semiconductor Devices* (Wiley, New York, 1981).
3. C. Kittel, *Introduction to Solid State Physics* (John Wiley & Sons, New York,1996).

4. M. Cardona and F. H. Pollak, Phys. Rev. **142**, 350 (1966).
5. S. Takagi, T. Tezuka, T. Irisawa, S. Nakaharai, T. Numata, K. Usuda, N. Sugiyama, M. Shichijo, R. Nakane, S. Sugahara, Solid State Electron. **51**, 526 (2007).
6. C. Le Royer , J.-F. Damlencourt, B. Vincent, K. Romanjek, Y. Le Cunff, H. Grampeix, V. Mazzocchi, V. Carron, F. Némouchi, J.-M. Hartmann, C. Arvet, C. Vizioz, C. Tabone, L. Hutin, P. Batude, M. Vinet, Solid State Electron. 59, 2 (2011).
7. Q.T. Nguyen, J.F. Damlencourt, B. Vincent, V. Loup, Y. Le Cunff, P. Gentil, S. Cristoloveanu, IEEE International SOI Conference Proceedings, 103 (2008).
8. C. Claeys, J. Mitard, G. Eneman, M. Meuris, E. Simoen, Thin Solid Films **518**, 2301 (2010).
9. E. Batail, S. Monfray, C. Tabone, O. Kermarree, J.F. Damlencourt, P. Gautier, G. Rabille, C. Arvet, N. Loubet, Y. Campidelli, J.M. Hartman, A. Pouydebasque, V. Delaye, C. Le Royer, G. Ghibaudo, T. Skotnicki, S. Deleonibus, IEDM Tech. Dig., 397 (2008).
10. E. Rimini, *Ion Implantation: Basics to device fabrication* (Kluwer, USA, 1995).
11. P.M. Fahey, P.B. Griffin, and J.D. Plummer, Rev. Mod. Phys. **61**, 289 (1989).
12. C. Claeys, E. Simoen, *Germanium-based technologies – from materials to devices* (Elsevier, Great Britain, 2007).
13. A. Janotti, R. Baierle, A.J.R. da Silva, R. Mota, A. Fazzio, Physica B **273-274**, 575 (1999).
14. A. J. R. da Silva, A. Janotti, A. Fazzio, R. J. Baierle, and R. Mota, Phys. Rev. B **62**, 9903 (2000).
15. A. Fazzio, A. Janotti, and A. J. R. da Silva, R. Mota, Phys. Rev. B **61**, R2401 (2000).

16. K. Sueokaa, J. Vanhellemont, Mat. Sci. Semicon. Proc. **9**, 494 (2006).
17. H.M. Pinto, J. Coutinho, V.J.B. Torres, S. Öberg, P.R. Briddon, Mat. Sci. Semicon. Proc. **9** (2006) 498.
18. K. Ding, H.C. Andersen, Phys. Rev. B **34**, 6987 (1986).
19. K. Nordlund, M. Ghaly, R.S. Averback, M. Caturla, T. Diaz de la Rubia, J. Tarus, Phys. Rev. B **57**, 7556 (1998).
20. W. Yu, Z.Q. Wang, D. Stroud, Phys. Rev. B **54** 13946 (1996).
21. J. Lauwaert, S. Hens, P. Śpiewak, D. Wauters, D. Poelman, I. Romandic, P. Clauws, J. Vanhellemont, Physica B **376–377**, 257 (2006).
22. P. Śpiewak, M. Muzyk, K.J. Kurzydłowski, J. Vanhellemont, K. Młynarczykc,P. Wabiński, I. Romandic, J. Cryst. Growth. **303**, 12 (2007), and references therein.
23. J. Vanhellemon, P. Śpiewak, K. Sueoka, J. Appl. Phys. **101**, 036103 (2007).
24. S. Brotzmann and H. Bracht, J. Lundsgaard Hansen and A. Nylandsted Larsen, E. Simoen, E. E. Haller, J. S. Christensen, P. Werner, Phys. Rev. B **77**, 235207 (2008).
25. J. Vanhellemont, and E. Simoen, J. Electrochem. Soc. **154**, H572 (2007).
26. A. Giese, N.A. Stolwijk and H. Bracht, *Appl. Phys. Lett.* **77**, 642 (2000).
27. S. Mayburg, *Phys. Rev.* **95**, 38 (1954).
28. R.A. Logan, *Phys. Rev.* **101**, 1455 (1956).
29. H. Letaw, W.M. Portnoy, L. Slifkin, Phys. Rev. **102**, 636 (1956).
30. A. Hiraki, J. Phys. Soc. Jpn. **21**, 34 (1966).
31. L.F. Konorova, *Soviet Phys. –Solid State* **10**, 2233 (1969).

32. J.A. Van Vechten, *Phys. Rev. B* **10**, 1482 (1974).
33. H. Bracht, MRS Bull., 22 (2000).
34. W.C. Dunlap Jr., Phys. Rev. **94**, 1531 (1954).
35. R.L. Minear, D.G. Nelson, and J.F. Gibbons, J. Appl. Phys. **43**, 3468 (1972).
36. S. Uppal and A.F.W. Willoughby, J.M. Bonar and A.G.R. Evans, N.E.B. Cowern, R. Morris and M.G. Dowsett, J. Appl. Phys. **90**, 4293 (2001).
37. S. Uppal, A.F.W. Willoughbya, J.M. Bonar, A.G.R. Evans, N.E.B. Cowern, R. Morris, M.G. Dowsett, Physica B **308–310**, 525 (2001).
38. Chi On Chui, K. Gopalakrishnan, P.B. Griffin, J.D. Plummer, and K.C. Saraswat, Appl. Phys. Lett. **83**, 3275 (2003).
39. S. Uppal, and A. F.W. Willoughby, J.M. Bonar, N.E.B. Cowern, T. Grasby, R.J.H. Morris, and M.G. Dowsett, J. App. Phys. **96**, 1376 (2004).
40. Chi On Chui, L. Kulig, J. Moran, and W. Tsai, K.C. Saraswat, Appl. Phys. Lett. **87**, 091909 (2005).
41. A. Satta, E. Simoen, T. Clarysse, T. Janssens, A. Benedetti, B. De Jaeger, M. Meuris, and W. Vandervorst, Appl. Phys. Lett. **87**, 172109 (2005).
42. A. Satta, T. Janssens, T. Clarysse, E. Simoen, M. Meuris, A. Benedetti, I. Hoflijk, B. De Jaeger, C. Demeurisse, and W. Vandervorst, J. Vac. Sci. Technol. B **24**, 494 (2006).
43. A. Chroneos, D. Skarlatos, C. Tsamis, A. Christofi, D.S. McPhail, R. Hung, Mat Sci Semicon Proc **9**, 640 (2006).
44. P. Delugas and V. Fiorentini, Phys. Rev. B **69**, 085203 (2004).
45. A. Chroneos, B. P. Uberuaga, R. W. Grimes, J. Appl. Phys. **102**, 083707 (2007).

46. A. Chroneos, H. Bracht, R. W. Grimes, and B. P. Uberuaga, Appl. Phys. Lett. **92**, 172103 (2008).
47. A. Chroneos, R. W. Grimes, B. P. Uberuaga, H. Bracht, Phys. Rev. B **77**, 235208 (2008).
48. C. Janke and R. Jones, S. Öberg, P. R. Briddon, Phys. Rev. B **77**, 075208 (2008).
49. P. Tsouroutas, D. Tsoukalas, I. Zergioti, N. Cherkashin, and A. Claverie, J. App. Phys. **105**, 094910 (2009).
50. S.Y. Park, Y.K. Kim, T. Won, Microelectron. Eng. **86**, 430 (2009).
51. M. Werner, and H. Mehrer, H. D. Hochheimer, Phys. Rev. B **32**, 3930 (1985).
52. H. Bracht, S. Brotzmann, Mat. Sci. Semicon. Proc. **9**, 471 (2006).
53. E. Hüger, U. Tietze, D. Lott, H. Bracht, D. Bougeard, E. E. Haller, and H. Schmidt, Appl. Phys. Lett. **93**, 162104 (2008).
54. T. E. Haynes and O. W. Holland, Appl. Phys. Lett **61**, 61 (1992).
55. G. Impellizzeri, S. Mirabella, E. Bruno, A. M. Piro, and M. G. Grimaldi, J. Appl. Phys. **105**, 063533 (2009).
56. A. Satta, E. Simoen, T. Janssens, T. Clarysse, B. De Jaeger, A. Benedetti, I. Hoflijk, B. Brijs, M. Meuris, and W. Vandervorst, J Electrochem. Soc. **153**, G229 (2006).
57. K. Benourhazi and J .P. Ponpon, Nucl. Instrum. Meth. B **71**, 406 (1992).
58. I. Suni, G. Göltz and M.A. Nicolet, S. Lau, Thin Solid Films **93**, 171 (1982).
59. T. Janssens, C. Huyghebaert, D. Vanhaeren, G. Winderickx, A. Satta, M. Meuris, and W. Vandervorst, J. Vac. Sci. Technol. B **24**, 510 (2006).
60. O.W. Holland, B.R. Appleton, and J. Narayan, J. Appl. Phys. **54**, 2295 (1983).

61. B. Stritzker, R.G. Elliman, J. Zou, Nucl. Instrum. Meth. B **175-177**, 193 (2001).

62. F. A. Trumbore, Bell Syst. Tech. J., **39**, 205 (1960).

63. E. Simoen, A. Satta, A. D'Amore, T. Janssens, T. Clarysse, K. Martens, B. De Jaeger, A. Benedetti, I. Hoflijk, B. Brijs, M. Meuris, W. Vandervorst, Mat. Sci. Semicon. Proc. **9**, 634 (2006).

64. K.S. Jones, and E.E. Haller, J. Appl. Phys. **61**, 2469 (1987).

65. P.J. McDonald, D.W. Palmer, Inst. Phys. Conf. Ser. **23**, 504 (1975).

66. Y.S. Suh, M. S. Carroll, R.A. Levy, G. Bisognin, D. De Salvador, M. Alper Sahiner, and C.A. King IEEE T. Electron. Dev. **52**, 2416 (2005).

67. Y.-L. Chao,a_ S. Prussin, and J. C. S. Woo, R. Scholz, Appl. Phys. Lett. **87**, 142102 (2005).

68. S. Mirabella, G. Impellizzeri, A. M. Piro, E. Bruno, and M. G. Grimaldi, Appl. Phys. Lett. **92**, 251909 (2008).

69. A. Einstein: Phys. Z. **18**, 121 (1917).

70. M. G. A. Bernard, G. Duraffourg: Phys. Status Solidi **1**, 699 (1961).

71. L. Pavesi, D.J. Lockwood, *Silicon Photonics* (Springer, Berlin, 2004).

72. http://www.ioffe.ru/SVA/NSM/Semicond/

73. U. Gnutzman, K. Clausecker: Appl. Phys. **3**, 9 (1974).

74. T. P. Pearsall, *Strained-Layer Superlattices: Materials Science and Technology*. Semiconductors and Semimetals **33** (Academic Press, Boston 1991).

75. S.A. Jackson, R. People: Mat. Res. Soc. Symp. Proc. **56**, 365 (1986).

76. H. Presting, H. Kibbel, M. Jaros, R. M. Turton, U. Menczigar, G. Abstreiter, H.G. Grimmeiss: Semicond. Sci. Technol. **7**, 1127 (1992).

77. T. P. Pearsall: Prog. Quantum Optics **18**, 97 (1994).

78. L. T. Canham, Appl. Phys. Lett. **57**, 1045 (1990).

79. A. G. Cullis, and L. T. Canham, Nature **353**, 335 (1991).

80. L. Pavesi, L. Dal Negro, C. Mazzoleni, G. Franzò, and F. Priolo, Nature **408**, 440 (2000).

81. Z. H. Lu, D. J. Lockwood, and J.-M. Baribeau, Nature **378**, 258 (1995).

82. A. G. Nassiopoulos, S. Grigoropoulos, D. Papadimitriou, Appl. Phys. Lett. **69**, 2267 (1996).

83. O. Bisi, S. Ossicini, and L. Pavesi, Surf. Sci. Rep. **38**, 1 (2000)

84. P. M. Fauchet, J. Lumin. **80**, 53 (1999).

85. J. R. Haynes and N. G. Nilsson, Proceedings of VIIth International Conference on Physics of Semiconductors, (Paris: Dunod, 1964).

86. J. Liu, X. Sun, D. Pan, X. Wang, L.C. Kimerling, T.L. Koch, and J. Michel, Opt. Express **15**, 11272 (2007).

87. T. Miya, Y. Terunuma, T. Hosaka & T. Miyashita, Electron. Lett. **15**, 108 (1979).

88. E. Desurvire, *Erbium-doped fiber amplifiers: s: principles and applications* (John Wiley & Sons, New York, 1994).

89. C.G. Van de Walle, Phys. Rev. B **39**, 1871 (1989).

90. R. A. Soref, L. Friedman, Superlattice Microst. **14**, 189 (1993).

91. J. Liu, D.D. Cannon, K. Wada, Y. Ishikawa, S. Jongthammanurak, D. T. Danielson, J. Michel, and L.C. Kimerling, Appl. Phys. Lett. **84**, 660 (2004).

92. F. Zhang and V.H. Crespi, P. Zhang, Phys. Rev. Lett. **102**, 156401 (2009).

93. S.W. Chang and S.L. Chuang, IEEE J Quantum Elect. **43**, 249 (2007).

94. M. El Kurdi, T.-P. Ngo, X. Checoury, S. Sauvage, G. Fishman, T. Kociniewski, D. Débarre, J. Boulmer, P. Boucaud, J. F. Damlencourt, O. Kermarrec, D. Bensahel, R. Jakomin, I. Sagnes, IEEE **978**, 259 (2009).

95. Y. Ishikawa, K. Wada, D.D. Cannon, J. Liu, H. –C. Luan, and L.C. Kimerling, Appl. Phys. Lett. **82**, 2044 (2003).

96. D.D. Cannon, J. Liu, Y. Ishikawa, K. Wada, D.T. Danielson, S. Jongthammanurak, J. Michel, and L.C. Kimerling, Appl. Phys. Lett. **84**, 906 (2004).

97. X. Sun, J. Liu, L.C. Kimerling, and J. Michel, Appl. Phys. Lett. **95**, 011911 (2009).

98. Y. Bai, K.E. Lee, C. Cheng, M.L. Lee, and E.A. Fitzgerald, J. Appl. Phys. **104**, 084518 (2008).

99. R. A. Soref and C.H. Perry, J. Appl. Phys. **69**, 539 (1991).

100. J. Menéndez and J. Kouvetakis, Appl. Phys. Lett. **85**, 1175 (2004).

101. J. Kouvetakis, J. Menendez, and A.V.G. Chizmeshya, Annu. Rev. Mater. Res. **36**, 497 (2006).

102. M. El Kurdi, H. Bertin, E. Martincic, M. de Kersauson, G. Fishman, S. Sauvage, A. Bosseboeuf, and P. Boucauda, Appl. Phys. Lett. **96**, 041909 (2010).

103. T.-H. Cheng, C.-Y. Ko, C.-Y. Chen, K.-L. Peng, G.-L. Luo, C. W. Liu, and H.-H. Tseng, Appl. Phys. Lett. **96**, 091105 (2010).

104. C. Li, Y. Chen, Z. Zhou, H. Lai, and S. Chen, Appl. Phys. Lett. **95**, 251102 (2009).

105. J. Liu, X. Sun, R. Camacho-Aguilera, L.C. Kimerling, and J. Michel, ECS Transaction **33**, 539 (2010).

106. H.-S. Lan, S.-T. Chan, T.-H. Cheng, C.-Y. Chen, S.-R. Jan, and C. W. Liu, Appl. Phys. Lett. **98**, 101106 (2011).

107. P.H. Lim, S. Park, Y. Ishikawa, and K. Wada, Opt. Express **18**, 16358 (2009).

108. M. El Kurdi, T. Kociniewski, T.-P. Ngo, J. Boulmer, D. Débarre, P. Boucaud,,J. F. Damlencourt, O. Kermarrec, and D. Bensahel, Appl. Phys. Lett. **94**, 191107 (2009).

109. M.L. Lee and E.A. Fitzgerald, M.T. Bulsara, M.T. Currie, and A. Lochtefeld, Appl. Phys. Lett. **97**, 011101 (2005).

110. D. Ahn, C.-Y. Hong, J. Liu, W. Giziewicz, M. Beals, L.C. Kimerling, and J. Michel, J. Chen and F.X. Kärtner, Opt. Express **7**, 3916 (2007).

111. J. Liu, M. Beals, A. Pomerene, S. Bernardis, R. Sun, J. Cheng,L.C. Kimerling, J. Michel, Nature Photonic **2**, 433 (2008).

112. S.-L. Cheng, G. Shambat, J. Lu, H.-Y. Yu, K. Saraswat,T.I. Kamins, J. Vuckovic, and Y. Nishi, Appl. Phys. Lett. **98**, 211101 (2011).

113. X. Sun, J. Liu, L.C. Kimerling, J. Michel, Opt. Lett. 34, 1198 (2009).

114. J. F. Liu, X. C. Sun, L. C. Kimerling, and J. Michel, Opt. Lett. **34**, 1738 (2009).

115. J. Liu, X. Sun, R. Camacho-Aguilera, L.C. Kimerling, and J. Michel, Opt. Lett. **35**, 679 (2010).

Chapter 2

B diffusion in Ge

Boron diffusion understanding in Ge is of fundamental importance in microelectronics. Indeed B is the most used p-type dopant, but its behavior in Ge is not well known yet. In this respect, in paragraph 2.1, an overview of the studies present in literature on B diffusion in Ge are reported, showing, in particular, the characteristic very low B diffusivity that up to now has hampered its study and comprehension. In order to overcome this problem our new approach, presented in paragraph 2.2, is based on the study of B diffusion under light ion irradiation. It is known, indeed, that ion implantation induces the formation of point defects along the ion tracks inside the matrix. This leads to a supersaturation of point defects that could enhance B diffusion inducing RED (radiation enhanced diffusion), allowing its detailed study. An accurate study on this phenomenon by varying the implant parameters, such as fluence, flux and temperature of the implants (as described in section 2.2.1) is reported on a qualitative point of view in section 2.2.2. These analysis shows that an enhancement of B diffusion during irradiation occurs also at room temperature. Furthermore, in order to perform a quantitative study, the B experimental diffused profiles were simulated with a proper model, described in details in section 2.2.3. The results obtained from simulations are related to the rate g through which B become mobile after interacting with a point defect, and the migration path λ that a mobile B travels inside the matrix before stopping. The g and λ values obtained are analyzed in detail as a function of implant flux and fluence in section 2.2.4 and as a function of temperature in section 2.2.5 and 2.2.7 in low and high temperature regimes, respectively. Moreover, in section 2.2.6 the dependence of B diffusion on free carrier generation was attentioned. Finally, a direct comparison between RED and thermal diffusion *in the high temperature regime allowed us to conclude that the mechanism of B diffusion is the same in the two cases, leading to a comprehensive description of its atomistic mechanism. Finally, in paragraph 2.3, the specific role of interstitials over vacancies in B diffusion is unambiguously demonstrated by relating B diffusion with the interstitial-made End of Range (EOR) defects produced by amorphizing implants.*

2.1 Introduction

Doping in semiconductors is a crucial point in the micro and optoelectronic industry. Unfortunately, as largely discussed in the previous chapter, while the dopant properties in Si are now well assessed [1], in Ge the picture is still controversial [2]. Nonetheless, a comprehensive knowledge of how dopant behave in Ge is essential to successfully model, design and hence realize devices with more reduced dimension while increasing their performances. Among all dopants, a key role is occupied by boron. Indeed it is the most used p-type dopant in Ge as in Si. For this reason, a good understanding of B diffusion in Ge is essential to predict profile redistribution during the thermal treatments necessary in the device production steps. The dominance of interstitials in the diffusion of B in Si is well established from different studies [1], and this behavior is confirmed also for B in Si-Ge alloys up to 20% Ge contents [3]. In spite of this, there are only a few studies on B diffusion in pure Ge. This is principally due to the very low diffusivity of B in Ge, that implies the need of using very high thermal budgets (very high temperature and long annealing times) in order to appreciate its diffusion and study its mechanism. This difficulty has lead to a large discrepancy in the various B diffusivity evaluation over the years. Indeed, recently, Uppal et al. [4-6] obtained B diffusivity (D_B) values which are at least two orders of magnitude lower than the lowest values previously reported in literature as can be seen in Fig. 2.1. Unlike older studies, based on sheet resistance [7] and junction depth [8] measurements in order to obtain the D_B values, Uppal et al. results [4-6]are based on Second Ion Mass Spectrometry analysis that allow to observe not only the active part but the effective B elemental profile. In this way the D_B values obtained are more accurate than before.

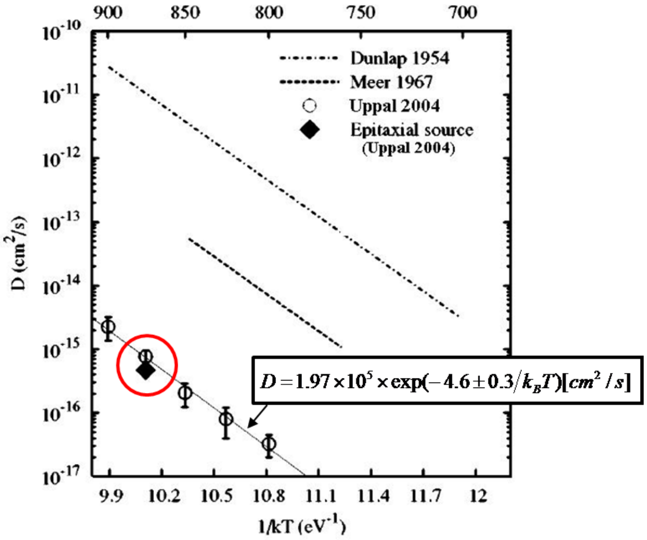

Fig. 2.1 Arrhenius plot for B diffusion in Ge from Uppal et al. studies performed by SIMS analysis (points) in comparison to previous data of Dunlap et al. (dash-dotted line) [7] and Meer et al. (dashed line) [8] performed by sheet resistance and junction depth measurement, respectively. The red circle shows that the diffusivity values obtained at 875°C in both cases in which B is put into the matrix by implant or by epitaxial growth, are indistinguishable within experimental error [6].

Comparing the diffusivities of self and foreign atoms in Ge as shown in Fig. 2.2 it is evident that B is the lowest diffuser in Ge. Moreover, unlike all the other common dopants (e.g. Ga, P, Sb, As), the activation energy of B diffusion in Ge obtained by Uppal et al. (reported in Fig. 2.1), is ~ 1.5 eV higher than that for self-diffusion (2.95 – 3.14 eV [2, 9-11]). This confirms that B is a special case in the dopant diffusion picture in Ge. Indeed it is well assessed, without any doubt, that almost all dopants in Ge and also Ge self-diffusion occur through a vacancy mediated mechanism. Indeed, according to Hu’s analysis [12] of diffusion mediated by a vacancy mechanism, the activation energy for impurity diffusion shoud be smaller or at least equal than that for self-diffusion. This consideration, as well as the very high activation energy (~ 6 eV) for vacancy mediated B diffusion obtained by ab initio calculations [13], lead to affirm that B in Ge cannot diffuse via a vacancy mediated mechanism. This is supported also by the positive binding energy between B and *V* (as reported in section 1.2.2 Table 1.3) calculated by Chroneos et al. [14,15], that suggests a repulsion between these two species.

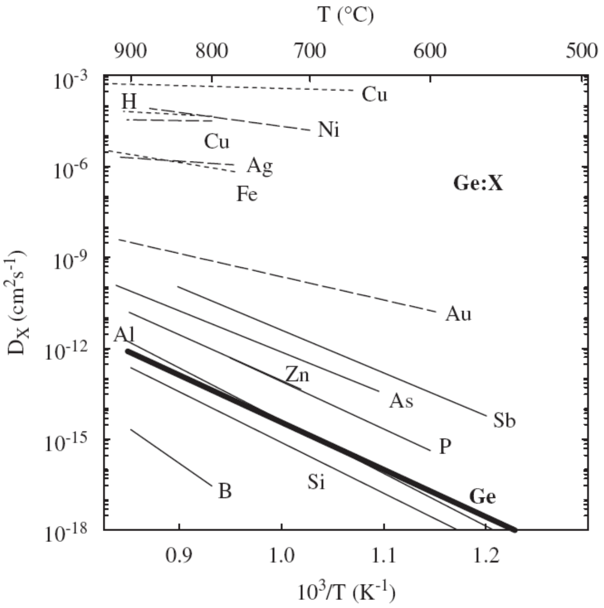

Fig. 2.2 Arrhenius plot of the diffusion of foreign atoms in Ge (thin lines) compared with self-diffusion (thick line). Solid lines represent diffusion data of elements that are mainly dissolved on substitutional lattice sites. Long-dashed lines illustrate diffusion data of hybrid elements, which are mainly dissolved on substitutional sites, but diffuse in an interstitial configuration via the dissociative mechanism. The short-dashed lines indicate the diffusion of mainly interstitial dissolved elements [18].

On the other hand, a direct mechanism of B diffusion can also be excluded, because the diffusivity is too low and the activation energy (of ~ 4.6 eV, as reported in Fig. 2.1) is too high compared with the one (~ 0.5-1 eV) usually related to a direct hope [16]. These considerations suggest that probably B diffuses in Ge through an interstitial mediated mechanism. This deduction is supported also by Delugas and Fiorentini theoretical calculations [17]. Indeed, an energy activation value of ~ 4.3 – 4.53 eV is obtained for the B-interstitial complex, in good agreement with the experimental value obtained by Uppal et al. [6]. However up to now there is no experimental study that unambiguously confirm these hypothesis.

Furthermore, few investigations have been done on the possible effect of implantation induced defects on the diffusivity. The B diffusion after an annealing at 875°C for 12 h (note the high temperature only 62 °C below the Ge melting point and the long duration of the annealing) in two different samples in which B doping is obtained by implant or growing a B doped epitaxial Ge layer by Molecular Beam Epitaxy (MBE) are shown in Fig. 2.3 (a) and (b) respectively.

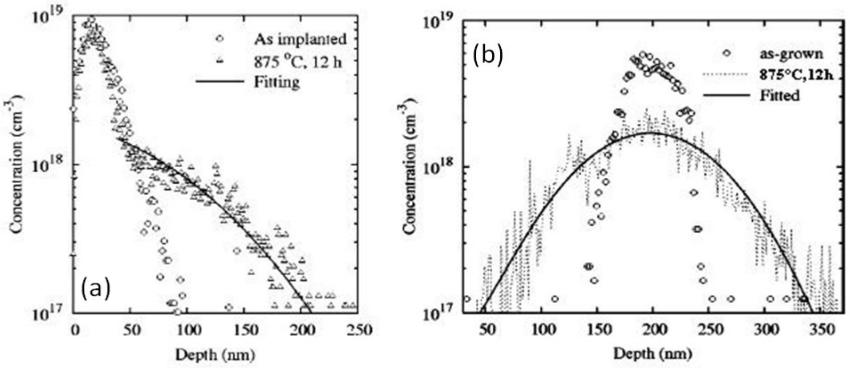

Fig. 2.3 (a) Boron concentration profiles after 3x10^{13} B^{+}/cm^{2}, 5 keV implantation (open circles), and annealing at 875°C, 12 h (open triangles). (b) B concentration profiles of the as-grown (open circles) and annealed (875°C,12 h, dashed line) samples. Continuous lines are the result of the fitting to the annealed profile [6].

The diffusion seems very similar in the two cases as confirmed by D_B values obtained simulating the two profiles (indicated with a red circle in Fig. 2.1) that are indistinguishable within the experimental error. Nonetheless, the low concentration gradient hampers a clear investigation of the phenomenon.

Then, further systematic studies on B diffusion are necessary to already understand its atomistic diffusion mechanism.

2.2 A new approach: diffusion during proton irradiation

In order to experimentally study B diffusion in Ge, a new approach has been used. A scheme of the experiment is reported in Fig. 2.4. An high energy implant was performed on a Ge sample containing four B narrow profiles. The defects created by the implants, indeed, induce a radiation enhanced diffusion (RED) of B in Ge.

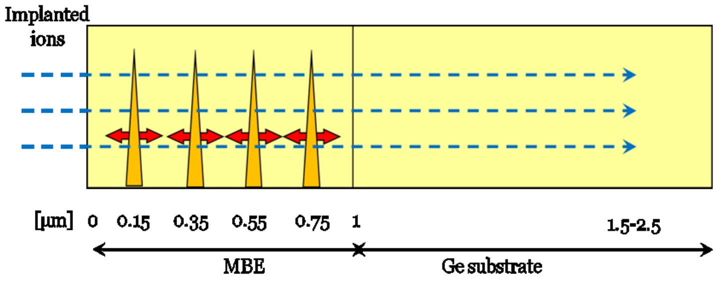

Fig. 2.4 Scheme of the RED experiment. The sample with four B deltas located at 150 nm, 350 nm, 550 nm and 750 nm respectively is epitaxially grown by MBE on a Ge substrate. Then the sample is irradiated with H^+ at high energy in order to have the R_p of the implant very far from the B-δs. Finally the B diffusion is investigated with SIMS analysis.

This phenomenon, already observed in the first seventies [19, 20], was recently invoked [5] to explain the anomalous tails in B implanted profiles with respect the profile obtained as a results of Lindhand-Scharff-Schiøtt calculations as reported in Fig. 2.5. Since the channeling contribution to these tails has been estimated to be only around 20%, the principal phenomenon that occurs in this case has been demonstrated not to be related to a channeling effect but to RED [5]. The excess of point defects generated during the implants promote B diffusion even at those temperatures otherwise forbidden to any appreciable diffusion.

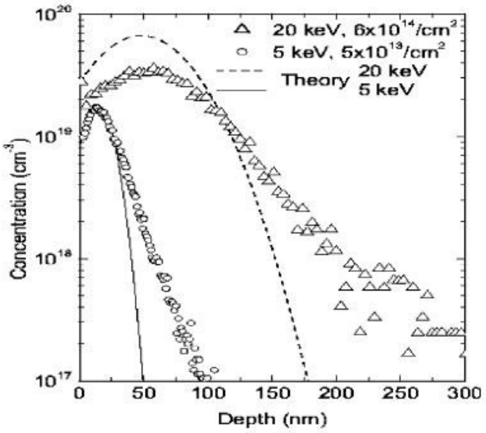

Fig. 2.5 Concentration profiles of as implanted B in <1 1 1> Ge for different energies: 20 keV, $6x10^{14}$ B^+/cm^2 (open triangles) and 5 keV, $5x10^{13}$ B^+/cm^2 (open circles) . The profiles obtained using LSS calculations for the two energies are also shown as dashed and continuous lines, respectively [5].

Exploiting the effect of RED, we have been able to analyze B diffusion in a wide range of temperatures, that allowed us to make an accurate study of B in Ge. Moreover, also a direct comparison between RED and thermal diffusion (TD) was performed in order to shed light on eventual difference in the B diffusion mechanism.

2.2.1 Experimental

Experiments were performed on a <100> Ge thin film containing a B multidelta structure grown by Molecular Beam Epitaxy (MBE). B profile of the as-grown sample obtained by Second Ion Mass Spectrometry (SIMS) is shown in Fig. 2.6 (dashed line). The MBE sample is ~1 µm thick and contains four 3-nm-thick B deltas (B-δs) characterized by a peak concentration of ~3x10^{18} B/cm^3. Each B-δ was used as a marker for the B diffusion, as previously done in Si crystals [21, 22].

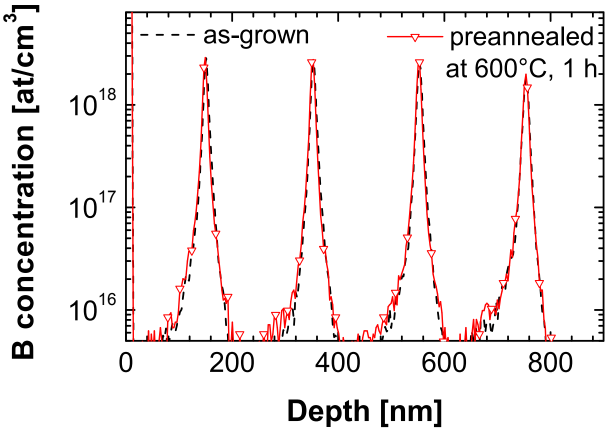

Fig. 2.6 Boron SIMS profiles of the sample grown by MBE containing four B-δs located at 150 nm, 350 nm, 550 nm and 750 nm respectively, just after growth (back dashed line) or after an annealing at 600°C for 1 h (red line puls triangles).

In fact, the sample design allows to have a very high B concentration gradient that is essential to discriminate even nanometric dopant diffusion. All samples were then preannealed at 600°C for 1 h under N_2 flux to eliminate any possible postgrowth defect. As can be seen in Fig. 2.6 (line plus triangles) B diffusion during preannealing is negligible. In the rest of the thesis we refer to the preannealed sampled as “starting sample”.

Subsequently the sample was cut and irradiated with H^+ in different experimental conditions in order to study the RED of B in Ge by varying the implant parameters. In particular implant energies of 200 or 300 keV were chosen so that the projected range (R_p) of the different implants (calculated by SRIM [23]) is always, much deeper than the B doped shallow region at 1.5 µm and 2.5 µm respectively. In this way, any direct interaction between

B and the implanted species is prevented. Moreover, these passing implants allow to have a quite uniform nuclear energy loss (i.e. point defects production) in the B-δ region.

In particular, the dependence of B diffusion on the fluence (1-10 x10^{15} H^+/cm^2), flux (6-35 x10^{11} H^+/cm^2s) and temperature (from liquid nitrogen temperature to 800°C) of the implant have been studied. In particular, the implants at temperatures above 550°C were performed at Surrey University.

In order to make implant at a fixed temperature, during the implantation the substrates were held on a 2 inch copper holder heated by means of an electrical resistance. The temperature was monitored by a thermocouple mounted in twin Ge samples held on the holder together with the implanted ones. Conversely in order to implant at liquid-nitrogen-temperature (-195°C) the substrates were held on a liquid-nitrogen cooled sample holder. All the thermal contacts were ensured by means of a silver paste. Moreover, in order to compare RED and B diffusion in equilibrium conditions, during some implantations, a twin sample was mounted on the implanted heater and covered from the ion beam. In this way the twin samples underwent only the annealing without any implantation and then they are used as reference samples.

Furthermore, to investigate B diffusion, the B concentration profile has been measured by secondary ion mass spectrometry (SIMS) using a CAMECA IMS 4f instrument (at the University of Padova), with a 3 keV O_2^+ analysing beam. Some measurements were repeated in selected samples at -70°C showing that, contrary to what observed in Si [24], sputtering by SIMS induces no significant migration of B at RT. This can be ascribed to the larger ion damage occurring in Ge with respect to Si, causing a complete amorphization of the Ge surface during the SIMS analysis which hampers the injection of interstitials [25].

2.2.2 Radiation Enhanced Diffusion of B

In Fig. 2.7 the SIMS profiles of the starting sample and the one irradiated with 300 keV H^+ at 350°C with a fluence of $1x10^{16}$ H^+/cm^2 and a flux of $1.9x10^{12}$ H^+/cm^2s are shown. The profiles of a twin sample that has undergone the same thermal treatment but without being irradiated is also reported as a reference of thermal diffusion (TD). It can be immediately seen that under irradiation B suffers an evident enhanced diffusion with respect to the equilibrium diffusion. Indeed, while the B profile after thermal diffusion observed at 350°C (blue open circles) is superimposed to the starting profile, the irradiated sample present a much lower concentration peak and a consequent enlargement of each B-δ.

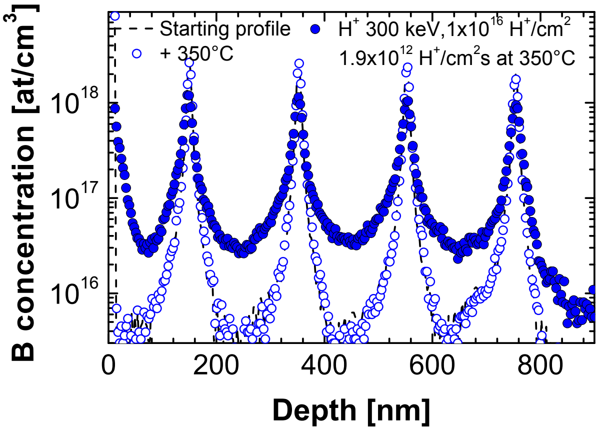

Fig. 2.7 Boron SIMS profiles of the starting sample (i.e. the as-grown sample after the 1 h, 600 °C annealing, dashed line) and after irradiation at 350°C with H^+ 300 keV, $1.9x10^{12}$ H^+/cm^2s, and $1x10^{16}$ H^+/cm^2 (blue closed circles). A reference for thermal diffusion at 350°C is also plotted (blue open circles).

This diffusion occurs even at room temperature. In Fig. 2.8, the detail of the B-δ at 550 nm is shown. The sample implanted at room temperature (green triangle) at 300 keV with the same fluence and flux as before is shown together with the starting B profile (dashed line) as a reference. It can be observed that the B profile strongly enlarges even at such a low temperature when irradiated with protons.

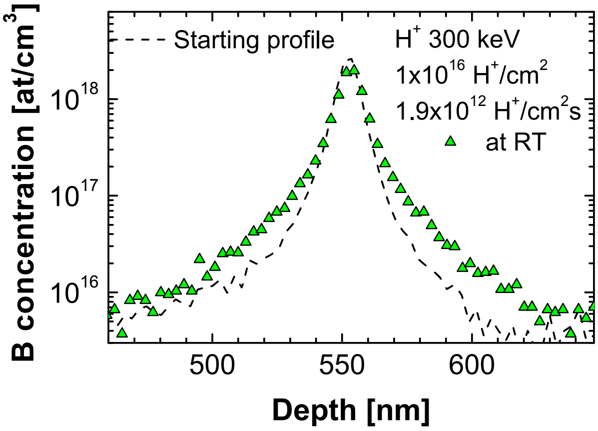

Fig. 2.8 Boron SIMS profiles of the starting sample (i.e. the as-grown sample after the 1 h, 600 °C annealing, dashed line) and after irradiation at room temperature (RT) with H$^+$ 300 keV, 1.9x10^{12} H$^+$/cm^{2}s, and 1x10^{16} H$^+$/cm^2 (green closed triangles).

Nonetheless, the radiation enhanced diffusion is not observed at temperatures as low as the liquid nitrogen temperature (LN$_2$T), as can be seen in Fig. 2.9 where B profiles of the starting sample (dashed line) and the one of the sample implanted at LN$_2$T (yellow diamond) are compared. This behavior can be related to the fact that the defects produced during the implant are totally frozen at this temperature. Indeed at LN$_2$T the defects have a very low mobility and for this reason they cannot interact with B present in the sample to promote its diffusion.

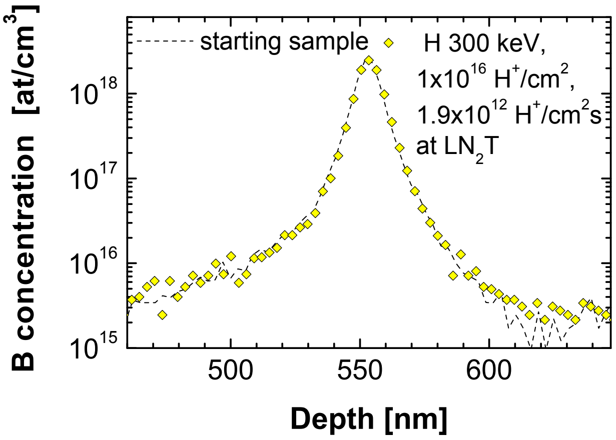

Fig. 2.9 Boron SIMS profiles of the starting sample (i.e. the as-grown sample after the 1 h, 600 °C annealing, dashed line) and after irradiation at liquid nitrogen temperature (LN$_2$T) with H$^+$ 300 keV, 1.9x10^{12} H$^+$/cm^{2}s, and 1x10^{16} H$^+$/cm^2 (yellow closed diamonds).

In order to understand how point defects generated during proton irradiation can influence B diffusion, a systematically study varying the implanted parameters (fluence, flux and temperature) has been done. Fig. 2.10 (a) and (b) show B diffusion in different samples irradiated varying H$^+$ flux or fluence, respectively. In Fig. 2.10 (a) the B profiles in the three samples irradiated wih H$^+$ 300 keV at a fixed fluence of 1x10^{16} H$^+$/cm^2, at 350°C and at different fluxes (6 – 35 x10^{11} H$^+$/cm^{2}s) are plotted. The different profiles don't show appreciable difference, evidencing a low dependence of B diffusion on the rate through which ions impinge on the sample, i.e. the point defects generation rate. On the other hand a difference in B diffusion is observed in Fig. 2.10 (b), where the profiles of the samples implanted with H$^+$ 300 keV at a fixed flux of 1.9x10^{12} H$^+$/cm^{2}s, at 350°C and at different fluences (1 – 10 x10^{15} H$^+$/cm^2) are plotted. It is evident that the profile broadening and hence the peak concentration lowering increase with the implanted fluence. Since all the implants are in a low rate regime, where collision cascade interactions can be negligible, this can be related to an increased total amount of point defects available to generate mobile B.

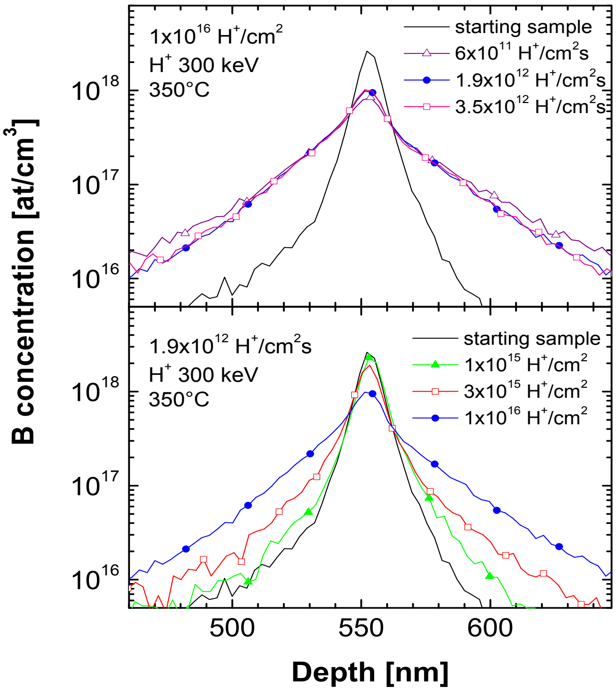

Fig. 2.10 Boron SIMS profiles of the starting sample (i.e. the as-grown sample after the 1 h, 600 °C annealing, dashed line) and samples implanted with H$^+$ 300 keV at 350°C. In particular in panel (a) the profiles are from samples irradiated with fixed fluence (1x10^{16} H$^+$/cm^2) and varying the ion flux at 6x10^{11} H$^+$/cm^{2}s (violet line plus open triangles), 1.9 x10^{12} H$^+$/cm^{2}s (blue line plus closed circles) and 3.5 x10^{12} H$^+$/cm^{2}s (pink line plus open squares). Indeed in panel (b) are plotted the profiles of samples implanted with fixed flux (1.9 x10^{12} H$^+$/cm^{2}s) and varying fluence: 1x10^{15} H$^+$/cm^2 (green line plus closed triangles), 3x10^{15} H$^+$/cm^2 (red line plus open squares), 1x10^{16} H$^+$/cm^2 (blue line plus closed circles).

The analysis of B diffusion profiles in samples implanted at fixed fluence (1x10^{16} H$^+$/cm^2) and flux (1.9x10^{12} H$^+$/cm^{2}s), varying the temperature (from LN$_2$T to 800°C) is more complex as can be seen in Fig. 2.11. In particular, in panel (a) B profiles after implant at 200°C (line plus squares) and 400°C (lines plus triangles) are shown, whereas in panel (b) the B profiles irradiated at 750°C (line plus triangles) and 800°C (line plus circles) are plotted together with the one of a sample annealed at 800°C without implantation as a reference for the thermal diffusion (open circles). The starting B profile is also plotted in both panels as a reference (dashed line).

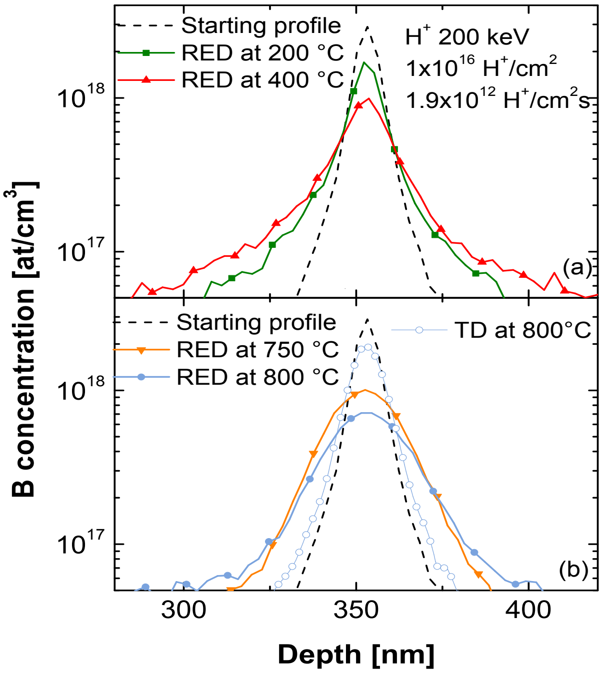

Fig. 2.11 Boron SIMS profiles in the starting sample (i.e. the as-grown sample after 600°C 1h, dashed line) and after 200 keV H$^+$ implant (1.9x10^{12} H$^+$/cm^{2}s, 1x10^{16} H$^+$/cm^2) performed (a) at 200°C (dark green line plus closed squares) and 400°C (red line plus closed triangles) and (b) at 750°C (orange line plus closed triangles) and 800°C (blue line plus closed circles). A reference for thermal diffusion at 800°C is also plotted in panel (b) (blue line plus open circles).

It can be observed that B diffusion increases with temperature. Indeed, as shown in Fig. 2.11, the peak lowers from 1.7x10^{18} B/cm^{2} in the sample irradiated at 200°C, to 1x10^{18} B/cm^{2} in the sample irradiated at 400°C indicating an higher number of diffusion events.

When the temperature is increased beyond 600°C, the B diffusion changes, as testified by a modification in the shapes of the B peak after diffusion in the two different thermal regimes. This trong modification in shape is quite clear comparing the profiles in Fig. 2.11 (a) (low temperatures) and Fig. 2.11 (b) (high temperatures). However, the difference between B diffusion at 800°C in equilibrium and non-equilibrium condition confirms that RED of B in Ge is still occurring also in the high temperature regime.

So, in order to better understand the B diffusion in Ge as a function of the implanted parameters, it is necessary to quantitatively study the RED phenomenon in Ge developing a simulation code. This is of fundamental importance also to understand the microscopic mechanism of B diffusion in Ge and to calculate the energies that characterize this process. The details on the simulation code are summarized in the next section.

2.2.3 The g-λ model

In order to implement a simulation code useful to reproduce B diffusion in Ge it is of fundamental importance to speculate on the microscopic mechanism of diffusion. In Fig. 2.12 the B SIMS profiles of the starting sample (dashed line) and the one diffused during 300 keV H^{+} implant at 350°C (fluence 1x10^{16} H^{+}/cm^{2} and flux 1.9x10^{12} H^{+}/cm^{2}s) are shown. It can be seen that the Gaussian fit (red line) is not able to reproduce the experimental peak broadening caused by diffusion events. This is a clear evidence that Fick’s law is not applicable in this case, so the B diffusion is driven not only by the B concentration gradient. Indeed, the exponential tails that characterize B diffusion indicate that the microscopic mechanism involved is mediated by point defects.

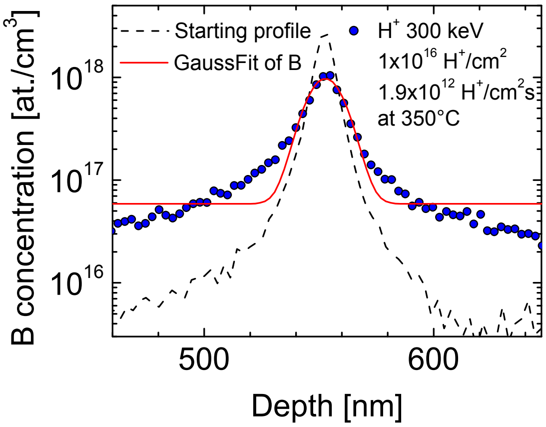

Fig. 2.12 Boron SIMS profiles of the starting sample (i.e. the as-grown sample after the 1 h, 600 °C annealing, dashed line) and after irradiation at 350°C with H$^+$ 300 keV, 1.9x10^{12} H$^+$/cm^{2}s, and 1x10^{16} H$^+$/cm^2 (blue closed circles). The red line is the Gaussian fit of the data.

The simulation model used in this thesis to quantitatively study B diffusion in Ge was developed at the University of Padua. It is based on Cowern's formalism [26, 27] which supposes that the diffusion of dopants occurs through a point defects mediated mechanism. In particular, in the boron case, it can be considered that the substitutional B atom (B_s) becomes mobile with a rate g and then diffuses for a mean path λ until it returns substitutional with a rate r. This model holds for example for the kick-out process, as schematized in Fig. 2.13, where an interstitial (*I*) interacts with a B_s creating the mobile species BI that diffuses through the matrix until it breaks down and B return substitutional. Nonetheless this model is applicable to any diffusion mechanism mediated by a point defect (vacancy or interstitial).

The fitting model is generated by a set of rate equations that describe the B diffusion according to the Fick's law, but considering also the terms related to the concentration of point defects that are involved in the diffusion mechanism. The model is based on discrete time and space intervals δt and δx , in such a way that the error introduced by the simulation code is lower than the experimental error.

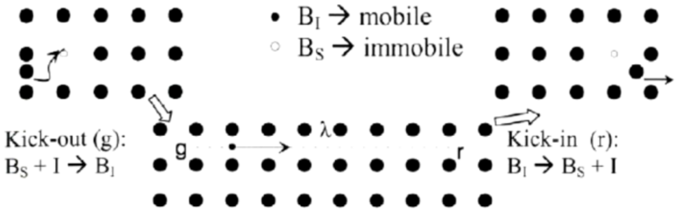

Fig. 2.13 Schematization of B diffusion. On the left an interstitial Ge atom (*I*) interact with a B atom in order to form the mobile species BI in the kick-out process, with a rate g. Then, the mobile species diffuses into the matrix along a mean path λ, before breaks and B return substitutional (kick-in process) with a rate r.

Indeed the starting B profile obtained by SIMS is hence divided in N intervals. The B diffused profiles are simulated by the model from the starting profile through a series of iterations. The B dose in each layer centered at x_i is calculated considering the B concentration $c_B(x,0)$ obtained from the experimental starting profile at that depth, according to the expression: $\delta B(x_i,0) = \int_{x_i-\frac{\delta x}{2}}^{x_i+\frac{\delta x}{2}} c_B(x,0)dx$. Then, due to the B diffusion, the B dose in each layer i-th decreases by an amount equal to (gδt)δB(x_i,0) per each time interval δt (being gδt the number of B diffusion events in the considered time interval). This quantity is then redistributed in the neighbor layers with an exponential profile. So, if δB(x_i,t) indicates the B dose in the layer centered at x_i at a generic time t, the corresponding dose in the same layer at each successive time interval δt+t can be expressed as:

$$\delta B(x_i, t+\delta t) = \delta B(x_i,t)[1-(g\delta t)] + \frac{g\delta t}{2\lambda}\delta x \sum_{\substack{j=1 \\ j\neq i}}^{N} \delta B\,(x_j,t)exp\left(-\frac{|x_i-x_j|}{\lambda}\right)$$

Eq. 2.1

The first term of Eq. 2.1 represents the lowering of the B dose due to the diffusion of B atoms from the i-th layer towards the close layers, while the second term indicates the increase in the B dose in the layer “i” due to the contributions of the B diffused atoms coming from all the other j-th layers (with j≠i).

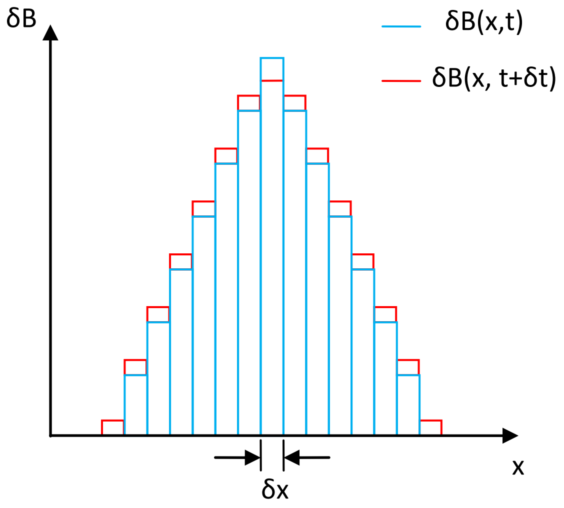

Fig. 2.14 Schematic representation of B diffusion simulation through the model used in this thesis. Sky blue lines represent B concentration profile at time t in each layer δx in which the profile is divided. Whereas, the variations of the profile calculated by the model in each layer δx at time t+δt are represented by the red lines.

Thanks to this approach, in order to calculate the B profile present inside the sample at the time t+δt it is necessary to calculate Eq. 2.1 for each layer in which the sample is divided. This process is schematically depicted in Fig. 2.14.In this way it is possible to obtain the final B profile inside the sample after the whole diffusion time, iterating this calculation from t=0 to the final t for each time interval δt.

The simulation procedure optimizes the diffused profiles by a comparison with the experimental diffused profile obtained by SIMS through a χ^2 optimization procedure. This allows the estimation of the g and λ parameters characteristic of the considered B diffusion. Then it is possible to calculate the B diffusivity according to the relation $D = g\lambda^2$ [26, 27]. The continuous line in Fig. 2.15 accounts for the quality of all the fits obtained by the model. It can be noted that this simulation, differently from the Gaussian one showed in Fig. 2.12 reproduces quite well the B diffused profile obtained experimentally.

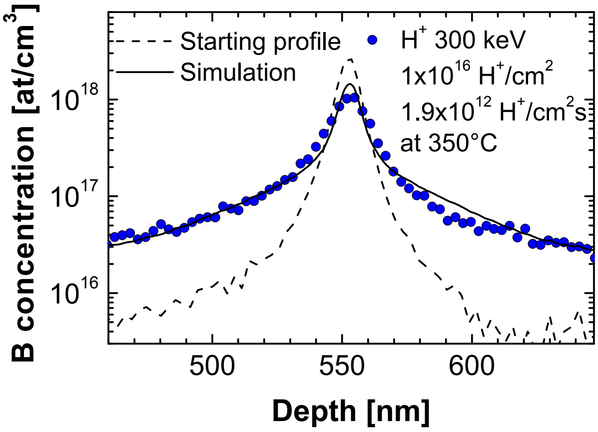

Fig. 2.15 Boron SIMS profiles of the starting sample (i.e. the as-grown sample after the 1 h, 600 °C annealing, dashed line) and after irradiation at 350°C with H^+ 300 keV, 1.9×10^{12} H^+/cm^2s, and 1×10^{16} H^+/cm^2 (blue closed circles). The solid line is the simulation of the data based on the kick-out model.

A deep analysis of the g and λ dependence on the different parameters varied in the samples processing will be developed in the next section in order to correlate B diffusion with the defects present in the sample and to clarify its atomistic diffusion mechanism.

2.2.4 RED dependence on implant flux and fluence

On the basis of the parameters g and λ obtained through the simulation model described above, it is possible to better understand the microscopic mechanism of B diffusion during irradiation.

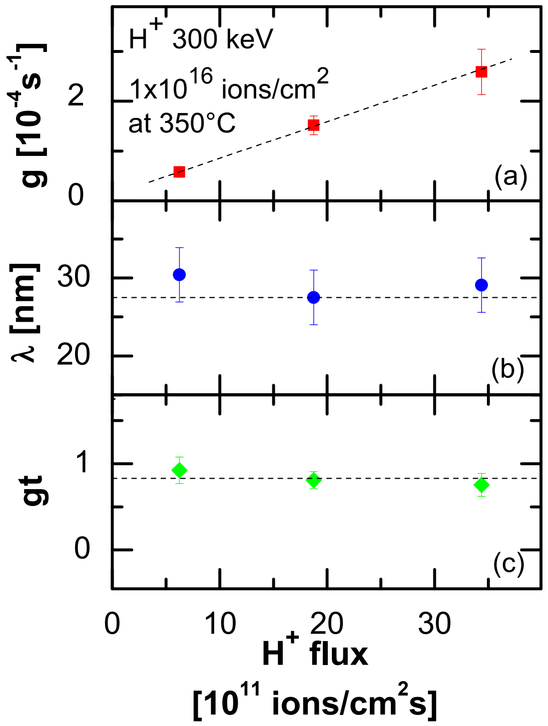

Fig. 2.16 Values of g (a), λ (b), and gt [where t is the diffusion time,(c)] are reported as a function of the H^+ flux (6-35 $x10^{11}$ H^+/cm^2) for samples implanted at 350°C, by fixing the fluence at $1x10^{16}$ H^+ /cm^2. The dashed lines are guidelines for the eye.

In Fig. 2.16 (a) and (b) the values of g and λ obtained by fitting the B diffused profiles after irradiation with 300 keV H^+ at 350°C with a fluence of $1x10^{16}$ H^+/cm^2 are reported as a function of the ion beam flux varied between 6 and 35 $x10^{11}$ H^+/cm^2s. The dashed lines are guidelines for the eye. Furthermore, Fig. 2.16 (c) shows the values of gt in the same samples, being t the diffusion time (e.g. the implant time), this quantity is related to the total number of diffusion event that occur during the implant for each B atom present into the sample. From panel (a) of Fig. 2.16 it can be observed that the generation rate of the mobile species g linearly increases with the ion flux, while the migration length λ remains constant. The same trend is observed in the case of gt indicating that the total number of diffusion events does not depend on the implant flux.

On the other hand, the g and λ values obtained in a sample irradiated at the same temperature with 300 keV H^+ with a flux of $1.9x10^{12}$ H^+/cm^2s but varying the fluence from $1x10^{15}$ to $1x10^{16}$ H^+/cm^2 show that both g and λ seem to be unaffected by the fluence variation (Fig. 2.17 (a) and (b) respectively), while the number of diffusion events gt linearly depends on the fluence [Fig. 2.17 (c)].

It can be seen, in fact, that gt is 0.15 for an implant fluence of $1x10^{15}$ H^+/cm^2, so only 15% of the B atoms undergo a diffusion event during the implant time. Increasing the implant fluence up to $1x10^{16}$ H^+/cm^2, gt approaches the unity, meaning that almost all B atoms have suffered at least a diffusion event.

This means that the RED phenomenon is related only to the total amount of implanted ions. It is known, indeed, that during ion implantation, point defects in excess with respect to the equilibrium are generated within each collision cascade. This induces an enhancement in the interaction probability between the implant produced defects and the B present inside the matrix. The *I* and *V* concentration are then limited by their diffusion and subsequent annihilation, returning to the equilibrium value after a certain transient time. Then, the observed trend for g and gt as a function of implant flux and fluence can be ascribed to the action of uncorrelated collision cascades, each of which extinguishes before being spatially superimposed to another cascade. Indeed, this indicates that a steady state for point defect population is never reached during implantation. In fact, under pure athermal beam-induced interstitial and vacancy generations, and diffusion-limited annihilation, the point defect populations (and as a consequence g) in steady-state conditions should have increased with a square-root trend as predicted by Shneider et al. [28]. Thus, the total observed diffusion of the B delta is the sum of many uncorrelated transient phenomena due to the fraction of point defects that can interact with B before annihilating. Therefore, the total number gt of migration events per B atom in the diffusion time t only depends on the implanted fluence [Fig. 2.17(c)], while the ion flux simply changes the frequency of migration events [Fig. 2.16 (c)].

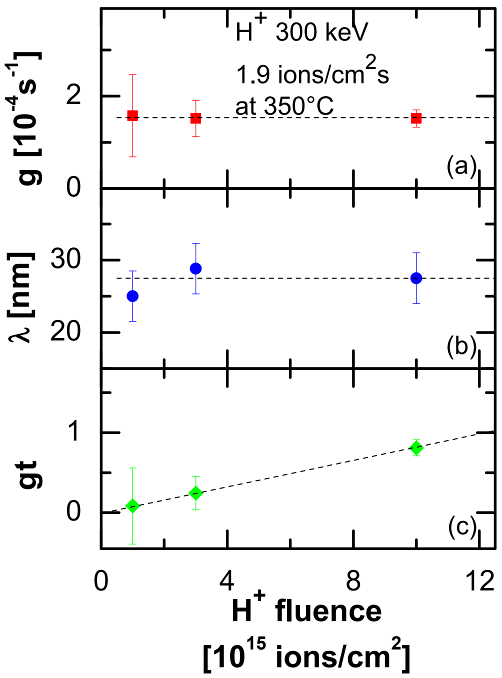

Fig. 2.17 Values of g (a), λ (b), and gt [where t is the diffusion time,(c)] are reported as a function of the H^+ fluence (1-10 x10^{15} H^+/cm^2) for samples implanted at 350 °C, by fixing the flux at 1.9x10^{12} H^+ /cm^{2}s. The dashed lines are guidelines for the eye.

Under the above picture, the measured λ is the projection of the mean free path perpendicular to the sample surface made by a B atom under the effect of many independent collision cascades. It is straightforward that at a given temperature λ must be constant, independently of both fluxes and fluences, as clearly evidenced by the experimental data in Fig. 2.16 (b) and Fig. 2.17 (b). Moreover, the constant trend of λ for all the H^+ implanted fluences also demonstrates that the B diffusion process is not affected by the presence of H atoms. In fact, if any H diffusion from its projected range region would have occurred, different amount of H would be present around the B delta affecting λ. This is not the case.

It is worth noting that the observed B diffusion is certainly not due to a direct knock-on phenomenon on B atoms generated by the impinging ion beam. In fact, at 350°C the threshold fluence to have each B atom involved in at least one migration event (i.e. to have $gt \sim 1$) is $\sim 1\times10^{16}$ H^+/cm^2 [Fig. 2.17(c)]. On the other hand, if we calculate the displacements per Ge atom in Ge after a 300 keV 1×10^{16} H^+/cm^2 implantation at the depth of the B-δ, we obtain $\sim1\times10^{-2}$ [23]. Indeed, the displaced B atoms for the same H^+ implant would be even much lower, because the knock-on inversely depends on the square of the atomic number. Thus, such calculations confirm our assumption that the observed broad B profiles are due to B diffusion indirectly caused by the interaction of B with the point defects generated by the implant.

2.2.5 RED dependence on implant temperature: low-T regime

As previously observed by the different shapes of the B diffused profiles, the temperature seems to play a dramatic role in the B diffusion mechanism. In order to shed light on this point a deep investigation was made as a function of temperature in both the low (<600°C) and high (>600°C) temperature regimes. Focusing the attention on the low temperature (low-T) implants, we observe that irradiation is able to promote a consistent B diffusion in spite of the fact that in this thermal regime the B diffusion is negligible. In Fig. 2.18 the Arrhenius plot of B diffusivity (D_B) experimentally obtained (closed triangles) for the samples implanted with 300 keV H^+, 1×10^{16} H^+/cm^2, 1.9×10^{12} H^+/cm^2s versus temperature from room temperature up to 550°C are shown. The continuous line is the fit of the data. It is well evident from Fig. 2.18 that under H^+ irradiation B diffusivity is many orders of magnitude higher than the equilibrium one obtained by Uppal and coworkers at temperatures higher than 800°C [4], and here extrapolated at lower temperatures [dashed line in Fig. 2.18]. We also measured a D_B value for thermal equilibrium diffusion at 755°C on similar samples containing a δ-B structure, indicated with an open triangle in Fig. 2.18. This value is in good agreement with Ref. [4] data. It is worth nothing that to obtain this point, an annealing with times as long as 90 h was necessary. Then, under irradiation D_B shows a weak dependence on the temperature, characterized by a very low (almost athermal) activation energy of E_D=0.10±0.01 eV.

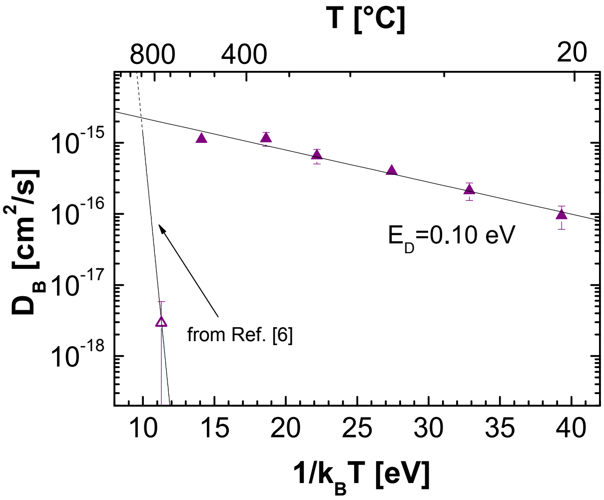

Fig. 2.18 Arrhenius plot of D_B (purple closed triangles) for samples implanted with $1x10^{16}$ H^+/cm^2 and $1.9x10^{12}$ H^+/cm^2s. The open triangle is relative to B thermal diffusion after an annealing at 755°C for about 90 h. The continuous line is the fit of the experimental data through which the activation energies E_D=0.10 eV is obtained. Dashed line in is the thermal diffusivity extracted from [6].

The observed trend for D_B can be understood considering the different diffusion steps by which B moves under the assumption that its diffusion is defect-mediated and, hence, $D_B=g\lambda^2$. The Arrhenius plot of the rate of generation of the mobile species, g, in the same temperature range, is shown in Fig. 2.19. It can be observed that the migration rate shows a single Arrhenius slope with a very low activation energy (Eg=0.06±0.01 eV), appearing essentially an athermal process. The low dependence of g on temperature can be explained considering that it results as a balance among different phenomena.

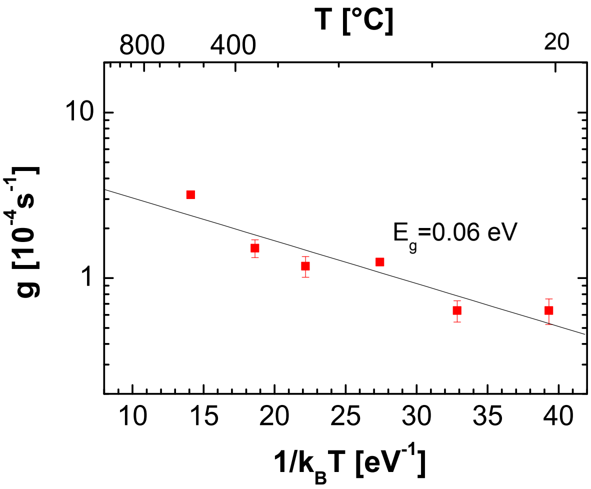

Fig. 2.19 Arrhenius plot of *g* (red closed squares) for samples implanted with 300 keV H^+, 1x10^{16} H^+/cm^2 and 1.9x10^{12} H^+/cm^2s. The continuous line is the fit of the experimental data through which the activation energies E_g=0.06 eV is obtained.

Under the assumption, based on theoretical studies [13-15, 17], as previously reported, that B diffuses by interacting with self-interstitials, g is a measure of the probability of *I*-B interactions forming the BI mobile species and, therefore, it depends on the amount of interstitial defects and on their diffusivity. Interstitials are athermally generated by the ion beam while resulting more mobile at higher temperatures. This increases the probability that the kick-out process occurs, i.e. that the mobile complexes

BI forms. On the other hand, it also favors the annihilation process $I + V \to 0$, reducing the interstitial concentration and, hence, the g value. Moreover, we cannot exclude that a small barrier for the formation of the BI pair exists.

It is worth noting that the absolute values of D_B and g in Fig. 2.18 and Fig. 2.19 could be scaled up and down by modifying the defect generation rate through the ion flux. In fact g, depending linearly on the ion flux [Fig. 2.16 (a)], gives an ion-assisted diffusivity D_B, which is also a linear function of the flux ($D_B = g\lambda^2$).

Moreover, under proton irradiation, the migration length λ reported in Fig. 2.20 (closed circles) also shows a negligible dependence on temperature in this thermal regime (see the dotted line in Fig. 2.20), while assuming very high values around 20 nm. This value is much higher than that obtained after B diffusion under thermal equilibrium condition (at 755 °C for 90 h) that is of only a few nanometers.

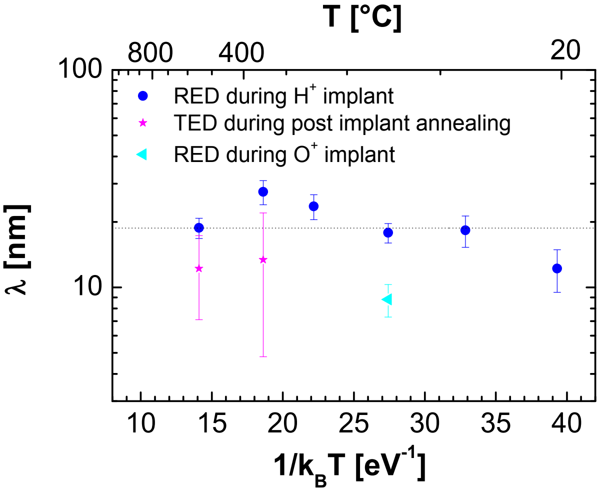

Fig. 2.20 Arrhenius plot of g (red closed squares) for samples implanted with 300 keV H$^+$, 1x10^{16} H$^+$/cm^2 and 1.9x10^{12} H$^+$/cm^{2}s (blue closed circles), 3 MeV O$^+$, 8×10^{13} O$^+$/cm^2, or 1.9×10^{12} O$^+$/cm^{2}s (cyan closed triangle), and after post-implant (300 keV H$^+$, 1x10^{16} H$^+$/cm^2 and 1.9x10^{12} H$^+$/cm^{2}s at RT) annealing (pink stars). Dotted line in is an eye guide.

The very high migration paths observed in this temperature range during irradiation could be related to an ionization-enhanced diffusion of B occurring under proton irradiation through a more diffusive charged mobile species, reminding that $\lambda = \sqrt{D_{B_m}/r}$, as previously proposed in Si [29]. In fact, a charge state dependent diffusion has been recently evidenced for Ga in Ge [30]. This aspect will be analyzed in details in the next section.

2.2.6 Dependence on free carrier generation

In order to ascertain if proton irradiation affects the B migration through free carrier generation, we have performed two experiments. First of all we have studied the diffusion of B by annealing samples previously implanted at room temperature (H^+ 300 keV, $1x10^{16}$ H^+/cm^2, $1.9x10^{12}$ H^+/cm^2s) at 350°C and 550°C for 1h, as schematized in the inset of Fig. 2.21.We clearly observed a post-implant enhanced diffusion, as reported in Fig. 2.21 with respect to the equilibrium diffusion (negligible at this temperature), similar to the well-known transient-enhanced diffusion (TED) of B in Si [31]. It is worth noting that the gt values observed after post-implant annealing (0.4 and 0.2 at 550°C and 350°C, respectively) are lower than those obtained under irradiation (1.7 and 0.8 at 550°C and 350°C, respectively). This clearly indicates that not all the point defects generated by the proton implant participate to the transient enhanced B diffusion during the post-implant annealing, being partially annihilated during the implant itself or even during the annealing ramp. However, since diffusion is now occurring without irradiation, ionization effects are absent.

The migration paths obtained by simulating the B diffused profiles after post implant annealing are reported as stars in Fig. 2.20. It can be seen that the obtained values for λ during annealing are very close to those found under irradiation. Therefore, ionization effects do not play a relevant role in the kick-in process of B diffusion under irradiation.

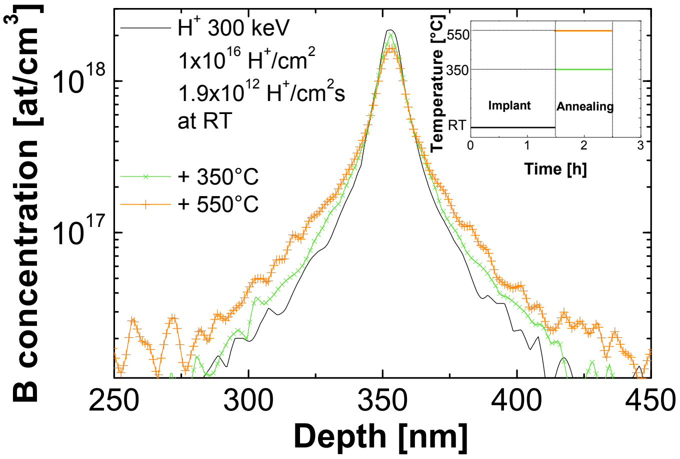

Fig. 2.21 Boron SIMS profiles of the starting sample irradiated at room temperature (RT) with H$^+$ 300 keV, 1.9x10^{12} H$^+$/cm^{2}s, and 1x10^{16} H$^+$/cm^2 (continuous black line) ant the ones after isochronal post-implant annealing for 1 h at 350°C (green line plus 'ics') and 550°C (orange line plus crosses). The inset of the figure is a schematic representation of the experimental procedure that involve the proton irradiation for the first 1.5 h and the subsequent 1 h annealing.

In order to further verify if the ionization effects do not affect even the kick-out process (e.g. creation of the mobile species), the sample was implanted with 3 MeV O$^+$, at room temperature at fluence and flux of 8x10^{13} O$^+$/cm^2 and 1.9x10^{12} O$^+$/cm^{2}s, respectively.

In particular the O implant energy was chosen in order to have the same projected range of H$^+$ ions implanted at 300 keV, instead the fluence was chosen in order to produce, in the B-δ region, the same total energy loss as for the 1x10^{16} H$^+$/cm^2 implant, as shown by the SRIM simulations in Fig. 2.22 (a) (closed circles and closed squares for H and O implants, respectively).The considered implant produce a dilute and quite uniform spatially distributed point-defects distribution around the B-δs, as also simulated by SRIM, with independent collision cascades affecting B profiles

[Fig. 2.22 (a)].This means that the energy transferred to target atoms, that leads to defects creation, is the same in both cases in proximity of the B-δs.

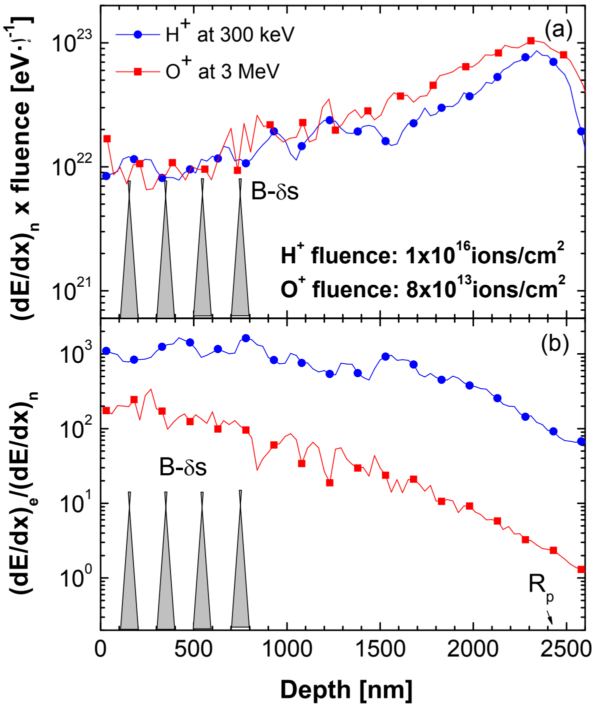

Fig. 2.22 (a) Total energy loss by nuclear collisions and (b) ratio of energy lost by interaction with electrons $(dE/dx)_e$ to that lost through elastic collisions with target ions $(dE/dx)_n$ for the 300 keV, 1×10^{16} H^+/cm^2 (blue closed circles) or 3 MeV, 8×10^{13} O^+/cm^2 (red closed squares) implants, as obtained by SRIM simulation [23].

Indeed, the amount of point defects that potentially interacts with B before recombining is the same.

On the other hand, the ratio of energy lost by interaction with electrons $(dE/dx)_e$ to that lost through elastic collisions with target ions $(dE/dx)_n$ changes with the ion mass (closed circles and closed squares for H and O implants, respectively), as shown in Fig. 2.22(b). However both hydrogen and oxygen implants we used do not amorphize the Ge wafer. Since the point defects generated by the two implants should be the same, any differences occurring in B diffusion might be related to the different carrier density available in the two cases.

In Fig. 2.23 is reported the starting B profile (i.e. the as-grown sample after 1 h 600 °C annealing, dotted line), the one further irradiated at 150°C with the 300 keV H^+ ion beam, at an ion flux of 1.9×10^{12} H^+/cm^2s with a fluence of 1×10^{16} H^+/cm^2 (closed circles) and the one for the sample implanted with O^+ at 3 MeV, at a fluence of 8×10^{13} O^+/cm^2 and flux of 1.9×10^{12} O^+/cm^2s (closed triangles). It can be observed that the B profiles after O^+ and H^+ irradiation are very similar, showing that the diffusion entity occurred in the two cases is comparable. This suggests that indeed the process is mainly driven by the energy deposited into elastic collisions.

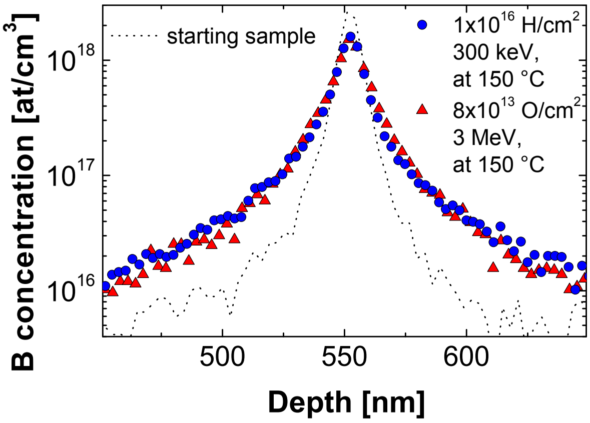

Fig. 2.23 Boron SIMS profiles of the starting sample (i.e. the as-grown sample after the 1 h, 600 °C annealing, dashed line) and after irradiation at 150°C with H^+ 300 keV, $1.9\text{x}10^{12}$ H^+/cm^2s, and $1\text{x}10^{16}$ H^+/cm^2 (blue closed circles) and with O^+ 3 MeV, at a fluence of 8×10^{13} O^+/cm^2 and flux 1.9×10^{12} O^+ /cm^2s (red closed triangles).

The values of g, λ and gt obtained by simulating with the kick-out model the B diffused profile under oxygen implantation are compared in Table 2.1 with the ones obtained under H implantation. It can be seen that the rate g of B mobile generation increases by two orders of magnitude under oxygen with respect to hydrogen irradiation as reported in Table 2.1. This increase is similar to that experienced by the energy released by nuclear interaction per incident ion $(dE/dx)_n$ which varies by more than two orders of magnitude passing from H (~$1x10^{-2}$ eV/ionÅ) to O (1 eV/ionÅ) [23]. On the other hand, the energy loss in ionization $(dE/dx)_e$ changes by a factor of 15. This is a strong evidence that g depends on the elastic collisions and is not affected by ionizations [which are very different in the two cases, as shown in Fig. 2.22(b)]. Since the total amount of the *V–I* pairs generated in the two cases is the same as a consequence, changing the ion mass only varies the frequency g by which the same point defects are generated. In fact, the average number of migration events (gt) suffered per B atom results comparable in the two cases as reported in Table 2.1. So, the mechanism through which B becomes mobile appears not-charge dependent.

	H^+ *implant*	O^- *implant*
g	$1.2x10^{-4}$ s^{-1}	$2x10^{-2}$ s^{-1}
λ	17 *nm*	9 *nm*
gt	0.7	1

Table 2.1 Comparison between g, λ, and gt values obtained by simulate with kick-out model, B diffused profile under 300keV H^+, 1.9×10^{12} H^+/cm^2s, 1×10^{16} H^+/cm^2 or under 3 MeV O^+, 8×10^{13} O^+/cm^2, 1.9×10^{12} O^+ $/cm^2s$.

Finally, the small difference in the migration path obtained under hydrogen or oxygen irradiation (reported in Table 2.1 and in Fig. 2.20) could be inferred to the different instantaneous point defects density within each collision cascade in the two cases, related to the different nuclear energy loss. In fact, the nuclear energy loss per ion per unit length calculated by SRIM differs by two orders of magnitude in the two cases in the B-delta region, as said before. In dense cascades, indeed, smaller paths can be expected.

However, found that the ionization effect does not play a role in B diffusion, it is of fundamental importance to understand if the mechanism depicted in non-equilibrium conditions is applicable also in equilibrium. This aspect will be discussed in the next section, by a direct comparison between RED and TD in the high temperature regime.

2.2.7 RED dependence on implant temperature: high-T regime

When the temperature is raised beyond 600°C, a different behavior is observed, already evident by the observation of the SIMS profiles, as reported in Fig. 2.11. In order to study this phenomenon, similar H^+ implants as before, were done at temperatures as high as 750°C and 800°C using a proper implant setup realized at the labs of Surrey University. The possibility of implanting H^+ at these very high temperatures allowed to perform a direct comparison with B diffusion under thermal conditions (i.e. without irradiation) during the same thermal annealing suffered by the irradiated samples. In fact, for temperatures as high as 800°C thermal broadening of the B-δs becomes well distinguishable even for the quite short diffusion times of the H^+ implants (~ 1.5 h). In Fig. 2.24 the λ values obtained by simulation of the experimental profiles are reported in an Arrhenius plot for the samples implanted with 200 keV H^+, $1x10^{16}$ H^+/cm^2, $1.9x10^{11}$ H^+/cm^2s (closed squares) at different temperatures (from 200 to 800°C). The λ value of a twin sample annealed together with the implanted one at 800°C but covered by the impinging H^+ ion beam is plotted as a reference of thermal diffusion (open square). The closed circle represents the data obtained during the deeper H^+ implant at 550°C (300keV, fluence$1x10^{16}$ H^+/cm^2, flux $1.9x10^{12}$ H^+/cm^2s) observed above. Furthermore, the shaded area in Fig. 2.24 indicates the range of λ values obtained previously under RED from room temperature up to 550°C under H implant at 300 keV. It can be observed that the new λ values obtained at low-T are comparable to those obtained before (Cfr. Fig. 2.20) for the 300 keV H^+ irradiation, even if the 200 keV H^+ implant produces a slightly higher point defect concentration in the B-δs region [23]. Nonetheless, when the temperature is increased above 600°C, the migration path reduces to values one order of magnitude lower than those obtained at low temperatures in both thermal and RED conditions. This behavior is similar to what happens for B in Si [22,24,27,29] in which B diffusion stops through a dissociation process, for which λ increases by decreasing the temperature.

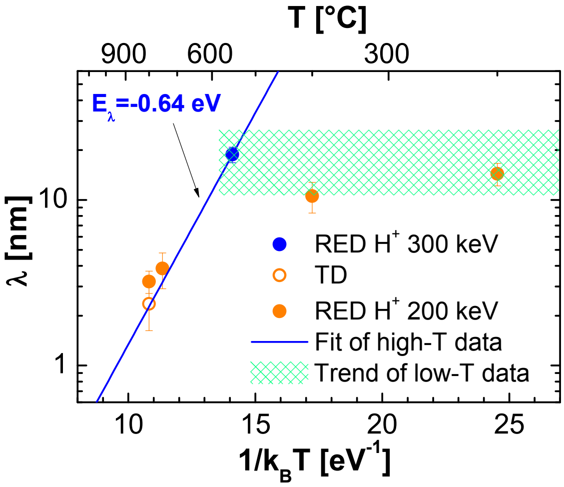

Fig. 2.24 Arrhenius plot of the mobile B diffusion length λ for samples implanted with at RT with 1x10^{16} H$^+$/cm^2, 1.9x10^{12} H$^+$/cm^{2}s at energy of 200 keV at temperature between 200°C and 800°C (orange closed circles). A value relative to B thermal diffusion at 800°C (orange open circle) is also plotted. These values are compared with those obtained previously during 300 keV H$^+$ implantation at 1x10^{16} H$^+$/cm^2, 1.9x10^{12} H$^+$/cm^{2}s performed between room temperature and 550°C (green shaded area). In particular the blue closed circle represents the λ value obtained for sample implanted at 550°C. Continuous line is a fit of λ values obtained in high-T regime (550-800°C).

Nonetheless, when the temperature decreases below 600°C, λ saturates at a value of ~ 20 nm and remains almost constant. This peculiar quite constant behaviour of λ over a very large range of the reciprocal temperature (1/kT goes from 15 to 40 eV^{-1}) can be due to the presence of some kind of traps in the sample. We remind that all samples were preannealed at 600°C to eliminate any possible post-growth defects. Indeed, the observed values of the B migration path around 20 nm correspond to an average distance between traps having a concentration of ~10^{17} at/cm^3, value comparable to the concentration of impurities like O or C present in our MBE germanium sample. Thus, the presence of O and C could be a limiting factor for B migration when the distances covered by the mobile species overcomes the average distance among traps in the sample.

By fitting the data in the temperature range of 550–800 °C (continuous line in Fig. 2.24), we obtained the energy barrier for this process (E_λ~ -0.64 eV). This negative value of the activation energy for the process of dissociation of the mobile species is also very similar to the -0.5 eV observed for B in Si [27]. The similar λ behavior both in equilibrium and RED conditions confirm that the diffusion mechanism deeply studied with the RED approach also hold for thermal diffusion. This can be supported by observing how the generation rate g changes with temperatures.

Fig. 2.25 shows the Arrhenius plot of the mobile B generation rate (*g*) calculated by simulation of the B diffused profiles in the samples implanted with 200 keV H^+, $1x10^{16}$ H^+/cm^2, $1.9x10^{12}$ H^+/cm^2s at different temperatures (from 200 to 800°C, closed squares). The thermal *g* at 800°C (open square) is also plotted as a reference. By observing the RED data, we can see that they do not follow a unique trend, while also in this case two different regimes appear. The linear trend evidenced in Fig. 2.25 with the continuous line shows a low activation energy, in the low temperature regime, comparable to that observed before (Fig. 2.19). On the other hand, at temperatures above 600°C (high-T regime) the g values deviate from the linear trend traced in the low-T regime, evidencing that a new mechanism for the B_m generation rate is occurring.

Since theoretical calculations suggest that B diffusion in Ge should be mediated by interstitials (*Is*), we can speculate that *g* measures the probability of B-*I* interaction forming the mobile species BI and thus depends on the amount and the diffusivity of *I*s. Moreover, *g* should include a barrier for the formation of the mobile species (E_F^{BI}). So, the activation energy of *g* can be written as

$$E_g = E_F^I + E_M^I + E_F^{BI}$$

Eq. 2.2

where E_F^I and E_M^I represent the formation and migration energy for *I*s, respectively. In equilibrium condition, *I*s are thermally generated and so at low–T their concentration inside the sample is negligible and, accordingly, B diffusion is not visible. On the contrary, under implantation *I*s are profusely generated into the sample also at low-T, thanks to the effect of the impinging ion beam. Hence, if *I*s are formed athermally by the irradiation process, E_F^I can be neglected in the Eq. 2.2, and thus the activation energy of *g* obtained by fitting experimental results (black line in Fig. 2.25) can be written as

$$E_g = E_M^I + E_F^{BI} \quad = 0.1 \text{ eV}$$

Eq. 2.3

in agreement with results showed for RED at low temperature in Fig. 2.19. Furthermore, this value for E_g is compatible with the migration energy of *I*s calculated in Ref. [32] and with a formation energy of BI (E_F^{BI}) close to zero as discussed in section 2.2.4.

Conversely, in the high-T regime *g* values obtained by the model for B diffusion under irradiation are much higher than those that we would expect by extrapolating the low-T g trend. Actually, we should assume that thermally generated interstitials are no more negligible in high-T regime, so they can contribute to enhance the amount of available interstitials within the sample. This causes an increase of the probability of interaction between *I*s and B_s to form BI and hence the *g* value increases. Taking into account the *I* formation energy (E_F^I) between 3.0 and 3.5 eV, according to Ref. [33-37], considering Eq. 2.2 and Eq. 2.3 we can assume that the *g* activation energy written as $E_g = E_F^I + 0.1eV$ can vary between 3.1 to 3.6 eV. Considering these two values and our experimental value for g in TD conditions (open square in Fig. 2.25), $g = g_0 \exp(-E_g/kT)$ was plotted as the two dashed lines in Fig. 2.25. According to this, we estimated g_0 in the order of $10^{12\pm1}\,s^{-1}$ that is of the same order of magnitude of the characteristic lattice vibration frequencies in Ge.

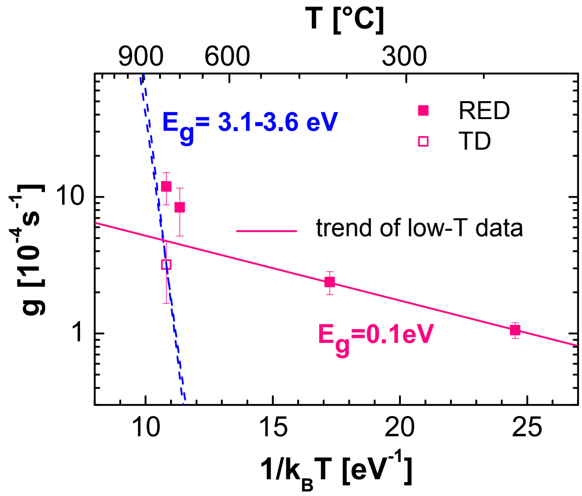

Fig. 2.25 Arrhenius plot of the mobile B generation rate, g, for samples implanted with 200 keV H^+, fluence $1x10^{16}$ H^+/cm^2, and flux $1.9x10^{12}$ H^+/cm^2s at temperatures from 200 to 800°C (pink closed squares). The g value relative to B thermal diffusion at 800°C is also plotted (pink open square). Continuous pink line is a fit of low-T data and shows an activation energy of 0.1 eV. The blue dashed lines represent the g thermal variation if only thermal *I*s are playing a role.

The found data evidence that the higher *g* values at high-T with respect to the trend at low-T could be related to the *I*s thermal generation that becomes more and more important and start to dominate over RED. This aspect does not affect the λ value at all, whose thermal variation is not related to thermal diffusion or RED conditions. These data confirm that the very low diffusivity of B in Ge could be only due to the lack of *I*s in Ge matrix, while once *I*s are furnished (e.g. by impinging ions), B undergoes diffusion processes also in the low-T regime. This last fact is supported by the evidence that once *I*s are formed, the only energetic barrier to B diffusion is represented by the migration energy for *I*s and the formation of the mobile species, both showing a very low activation energy (~ 0.1 eV).

Furthermore a clear definitive proof of the role of interstitials in mediating B diffusion will be treated in the next section.

2.3 The role of interstitials

In order to unambiguously and definitively demonstrate the role of the different point defects (vacancies or interstitials) in the B diffusion in Ge, it is necessary to observe B behavior in a Ge matrix in which a supersaturation of only one kind of defect is generated. As said above both the very low B equilibrium diffusivity in Ge and its very high activation energy of 4.65 eV [4-6] suggest that the mechanism of B diffusion is incompatible with a vacancy-assisted type.

Recently, it was clarified, after a large debate, that the end-of-range extended defects formed in Ge after a preamorfization process with Ge ions followed by a solid phase epitaxial regrowth (SPER) [38, 25] are constituted by interstitials. Indeed, Fig. 2.26 (a) and (b) show the cross sectional transmission electron microscopy (XTEM) image of a <100> Ge sample implanted with Ge^+ at 150 keV with a fluence of $1x10^{14}$ Ge^+/cm^2 at around 0°C and then annealed at 330°C for 1325 s, during which the original amorphous/crystal (a/c) interface shifted of about 35 nm.

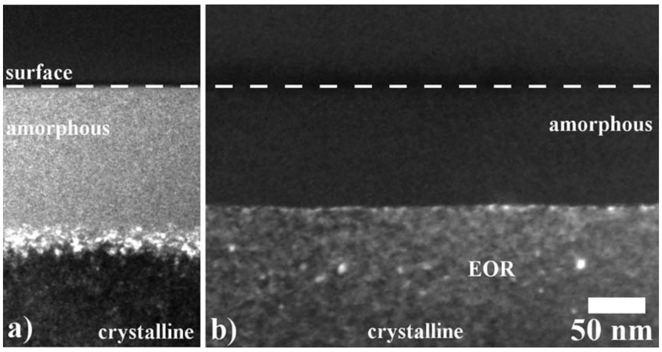

Fig. 2.26 XTEM images of a Ge layer (a) after 150 keV Ge^+ $5x10^{14}$ Ge^+/cm^2 implantation and (b) after subsequent annealing at 330 °C for 1325 s. The dashed line follows the surface of the wafer [25].

From panel (a) it can be seen that the a/c interface appears rough and heavily strained, as evidenced by the white contrast. After the annealing, instead, small white dots can be observed in the region located just below the original a/c interface [Fig. 2.26 (b)][25].

Moreover, Bisognin et al. studied this kind of defects by using high-resolution X-ray diffraction (HRXRD) [38]. Fig. 2.27 shows, in particular, the perpendicular strain profile obtained simulating the diffraction spectra of the as-implanted sample (with 300 keV Ge^+, $2x10^{15}$ Ge^+/cm^2 at liquid nitrogen temperature).

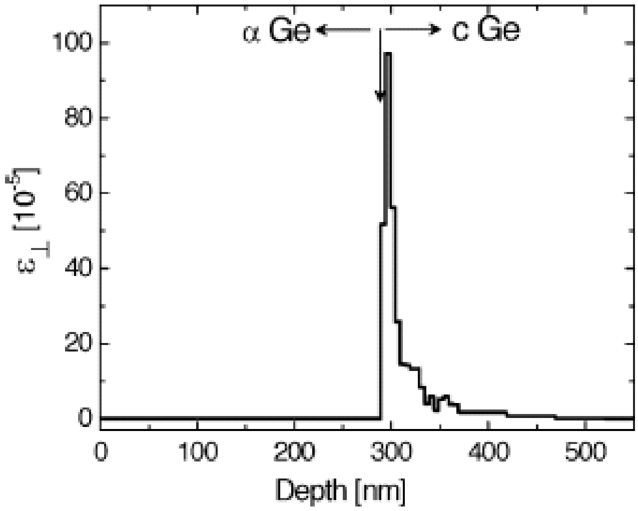

Fig. 2.27 Perpendicular strain profile of the sample implanted with 300 keV Ge^+, 2×10^{15} Ge^+/cm^2 [38].

The figure reveals that the sample can be divided into two parts: the first region, extending from the surface up to the a/c interface, where no strain is present, corresponding to the amorphized part. On the contrary, the deeper region, very shallow and located just below the a/c interface, exhibits a considerable amount of positive strain. This testifies the presence of interstitial-type defects in correspondence of the End Of Range defects region. Furthermore the evolution of these defects suggested that they completely anneal already at temperatures around 400°C. Hence, the dissolution of EOR defects can be exploited in order to observe if it induces any B diffusion. Since EOR defects release interstitials, this would demonstrate that diffusion occurs via the interaction of B with interstitials.

2.3.1 Experimental

A sample grown by molecular beam epitaxy on a <100> Ge Czochralski with a 3-nm-thick B-δ located at a depth of ~300 nm was amorphized at room temperature with a multiple Ge^+ ion implantation (440keV Ge^+, $5x10^{14}$ Ge^+/cm^2 plus 150 keV Ge^+, $2x10^{14}$ Ge^+/cm^2) at room temperature, as schematized in Fig. 2.28 (a). The amorphous layer is ~370nm-thick, as verified by Rutherford backscattering spectrometry. The sample was then annealed at 300°C for different times [Fig. 2.28 (b)] in order to gradually induce SPER of the amorphous phase [39] and promote the formation of EOR defects beyond the original a/c interface. The SPER was interrupted after 20 h when the a/c interface had reached the depth of ~ 235 nm, in order to recrystallize just the B delta while minimizing the EOR defects dissolution that might occur during the SPER annealing itself. After the above partial SPER, the sample was cut in pieces and further annealed for 1 h at different temperatures between 300°C and 550°C in order to induce the dissolution of the EOR defects and consequently inject interstitials toward the B delta, while rapidly completing the recrystallization process as illustrated in Fig. 2.28 (c). The obtained results of this kind of experiment are reported in the following.

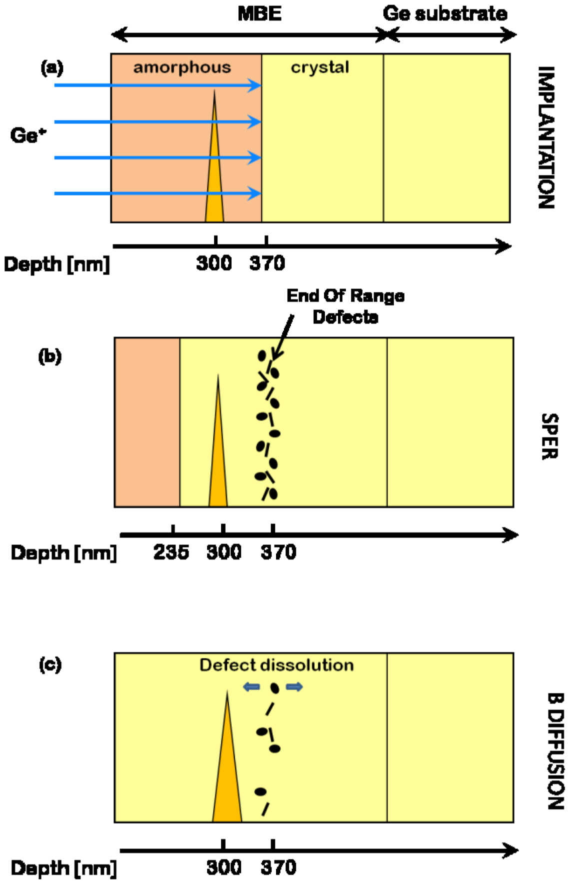

Fig. 2.28 Scheme of the experiment. (a) The sample containing a B-δ at a depth of 300 nm (grown by MBE) is implanted with 440keV Ge$^+$, 5x10^{14} Ge$^+$/cm^2 plus 150 keV Ge$^+$, 2x10^{14} Ge$^+$/cm^2 in order to create a 370 nm-thick amorphous layer. (b) Than the sample is annealed at 300°C for different times in order to induce the SPER and at the same time the formation of EOR defect in correspondence of the original a/c interface. (c) The B-δ broadening is analyzed during subsequent anneling (for 1 h, at temperatures from 300°C to 550°C) that induces the EOR defect dissolution.

2.3.2 Transient Enhanced Diffusion of B during End Of Range defects dissolution

Fig. 2.29 shows a cross-sectional TEM image of the sample after the partial SPER, whose boron SIMS profile (green line) was superimposed with the same depth scale. The a/c interface after partial SPER is clearly visible but, more importantly, the TEM image shows a band of EOR defects around the depth of 370 nm. Such defects are in the form of small dots and are similar to those observed by Koffel et al. [25]. Fig. 2.29 also reports the strain profile (blue line) related to the EOR band of the same sample that is of positive sign, indicating that these defects cause an expansion of the lattice. This fact demonstrates the interstitial nature of the EOR defects (i.e. Ge atoms in excess), as previously demonstrated [38].

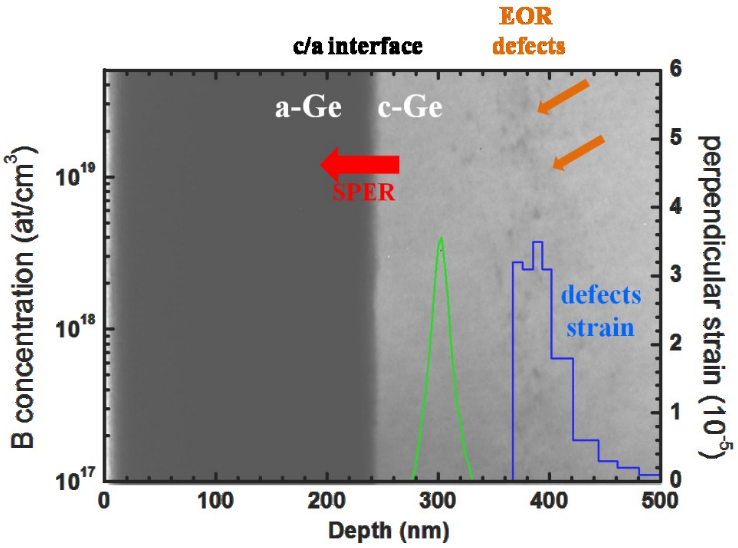

Fig. 2.29 XTEM micrograph, SIMS boron depth profile (green line), and HRXRD strain profile (blue line) of the sample after partial SPER at 300°C, superimposed with the same depth scale.

XTEM observations indicate that the above EOR defects are still present after annealing for 1h at 380°C, disappearing below the sensitivity of the technique after 1h at 420°C. These results are in agreement with the ones obtained by HRXRD showed in Fig. 2.30. Here, indeed, it can be observed that the strain present inside the sample after SPER (dashed black line) decreases with increasing the annealing temperature until almost disappearing after 1 h at 420°C (pink line). Therefore, it can be affirmed that the EOR defects dissolve within the temperature range we have investigated releasing interstitials.

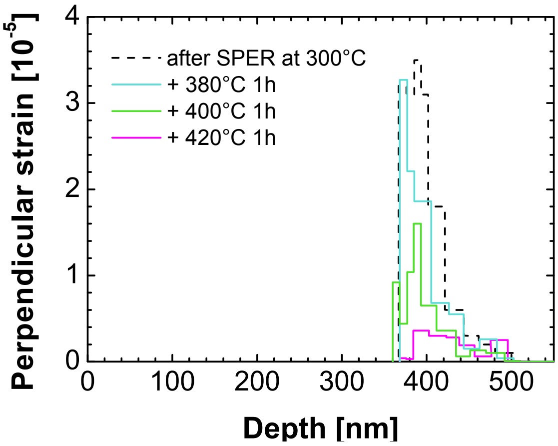

Fig. 2.30 Perpendicular strain profiles of the sample implanted with 440keV Ge^+, $5x10^{14}$ Ge^+/cm^2 plus 150 keV Ge^+, $2x10^{14}$ Ge^+/cm^2 after SPER at 300°C (dashed line) and after subsequent isochronal annealing (1 h) at 380°C (sky blu line), 400°C (green line) and 420°C (pink line).

In order to investigate the effect of interstitials released by EOR defects on B diffusion, Fig. 2.31 shows SIMS profiles of B-δ after isochronal annealing (1 h) at 380°C (light blue line), 420°C (pink line) and 450°C (violet line) compared with the starting one after the SPER at 300°C . It can be seen that B profile shows a clear broadening after 1 h at 380°C, that increases with temperature and saturates above 420°C.

Considering that the equilibrium diffusion in the above processes is expected to be negligible in this temperature range, Fig. 2.31 clearly demonstrates that B undergoes an enhanced diffusion during post-SPER annealing in amorphized Ge. As the diffusion occurs in the same temperature range of the EOR dissolution, we can conclude that it is caused by the flux generated by the EOR dissolution. This result is crucial, as it demonstrates that the dissolution of EOR in Ge promotes the diffusion of B and, therefore, that the diffusion mechanism of B in Ge is assisted by interstitials, as also confirmed by Bracht et al. by a comparison between P and B diffusion under irradiation [40].

More insights about the phenomenon can be obtained by a quantitative analysis of both delta diffusion and strain profiles.

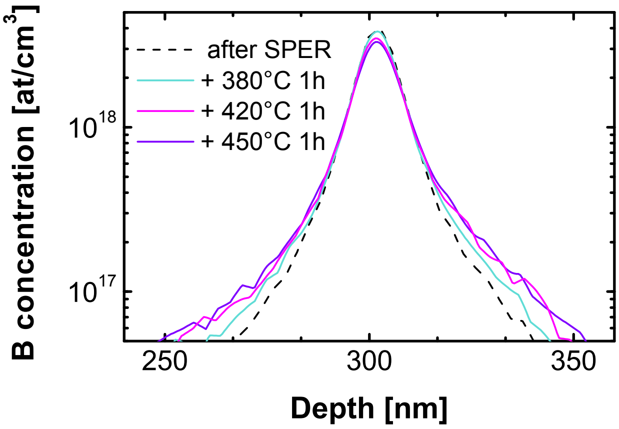

Fig. 2.31 Boron SIMS profiles of the sample implanted with 440keV Ge$^+$, 5x10^{14} Ge$^+$/cm^2 plus 150 keV Ge$^+$, 2x10^{14} Ge$^+$/cm^2 after SPER at 300°C (dashed line) and after and after subsequent isochronal annealing (1 h) at 380°C (sky blu line), 400°C (green line) and 420°C (pink line).

In particular we simulate B diffusion profiles by the above described g-λ model. The values obtained for diffusion length are constant as can be observed in Fig. 2.32 (open circles) with a mean value of 16±3 nm similar to those obtained in RED and TED after previous H$^+$ implant experiments in the same temperature range, here indicated by the shaded area. Indeed, the B diffusion mechanism is the same as before. Furthermore, the Arrhenius plot of gt (with t=1h) for the samples annealed from 300°C to 550°C is reported in Fig. 2.33 (blue squares). On the other hand, a quantitative estimation of the time evolution of the amount of interstitials contained in the EOR defects can be obtained by the strain profiles exploiting the proportionality between strain and the *I* amount [41]. So, defining S the strain integral in the EOR region, its value as a function of $1/k_BT$ is depicted in Fig. 2.33 (red squares). In particular, Fig. 2.33 shows that the trends of gt and S are complementary: up to 350 °C gt remains zero and the strain integral remains at its maximum value; then, by increasing the temperature gt increases and the strain integral decreases up to 420 °C, while gt saturates to 0.22 and the strain integral saturates at a small value close to zero. This further demonstrates the close relationship between diffusion and *I*-related defects dissolution.

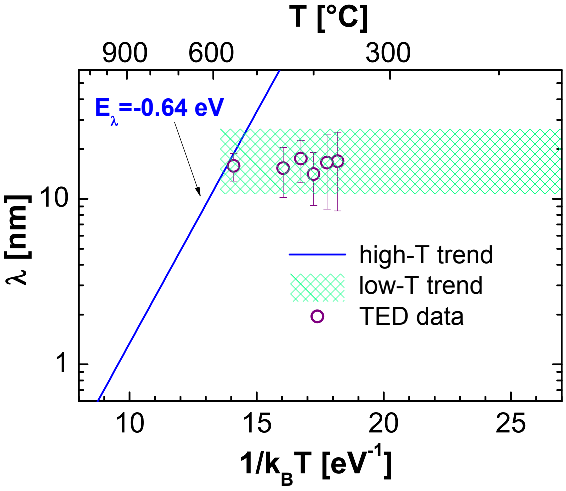

.

Fig. 2.32 Arrhenius plot of the mobile B diffusion length λ for samples implanted at RT with 440keV Ge^+, $5x10^{14}$ Ge^+/cm^2 plus 150 keV Ge^+, $2x10^{14}$ Ge^+/cm^2 and then annealed for 1 h (open circles). These values are compared with those obtained previously during 300keV H^+ implantation at $1x10^{16}$ H^+/cm^2, $1.9x10^{12}$ H^+/cm^2s performed in low-T regime (green shaded area). Continuous line is a fit of λ values obtained in high-T regime (550-800°C).

The above data can be modeled under the three following assumptions: the first is that the perpendicular strain integral S is proportional to the dose of interstitials contained in the EOR defects F_I [41]; the second is that a transient enhanced diffusion of B occurs, governed by a thermally activated release of interstitials from the EOR region with a rate α that can be written as:

$$\alpha = \alpha_0 exp\left({}^{-E_\alpha}/{}_{k_B T}\right),$$

Eq. 2.4

where E_α is the energy barrier and α_0 is the prefactor for the interstitial release. Finally the third assumption consider that the sinks for interstitials and B do not vary significantly with time and temperature. Then the equations for the strain integral S and gt as a function of $1/k_BT$ can be expressed as:

$$S = S_{sat} + (S_0 - S_{sat}) exp\left[-\alpha_0 t\, exp\left({}^{-E_\alpha}/{}_{k_B T}\right)\right]$$

Eq. 2.5

$$g = g_{sat}\left\{1 - exp\left[-\alpha_0 t\, exp\left({}^{-E_\alpha}/{}_{k_B T}\right)\right]\right\}$$

Eq. 2.6

where S_0 is the starting value of the strain integral, S_{sat} and g_{sat} are the saturation values for S and g at high temperature respectively and t is the annealing time. Eq. 2.5 and Eq. 2.6 allow to perfectly fit the data in Fig. 2.33 considering a single set of free parameters S_0, S_{sat}, g_{sat}, α_0, and E_α. This result further confirms and gives a quantitative model of the picture described above, where EOR dissolution in amorphized Ge injects interstitials in the bulk promoting B diffusion. It is worth noting that the model assumes that the EOR defects responsible for TED are formed by a single class of defects, dissolving, as reported in Fig. 2.33, with a single activation energy of (2.1±0.3) eV. and a prefactor of $\alpha_0=2\text{x}10^{(12\pm2)}$ s^{-1}. The activation energy appears significantly lower than the energy (3.8 eV) found for the dissolution of {311} defects responsible for the TED of B in Si [42]. Indeed, the temperatures for EOR dissolution in Ge results lower than the temperatures for {311} dissolution in Si even if considering homologous temperatures, consistently with the much smaller defects observed in Ge. It is worth noting that the TED in Ge is much less evident than in Si, clarifying why it was overlooked in the experiments reported so far.

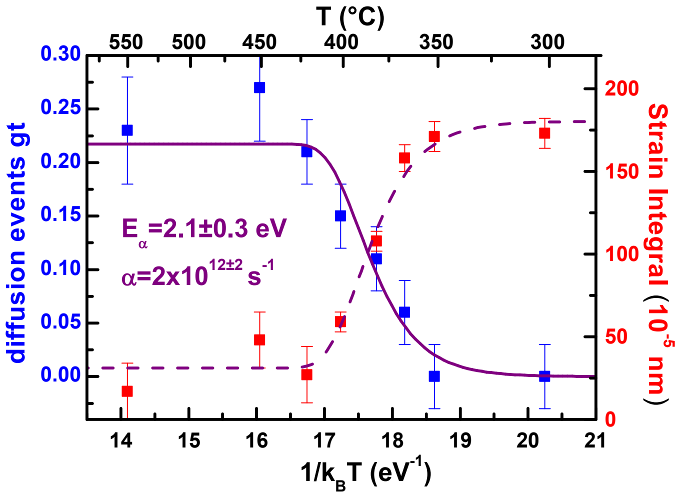

Fig. 2.33 Arrhenius plot of the strain integral (red closed squares) and diffusion events gt (blue closed squares) data extracted from the HRXRD and the simulation of the SIMS results, respectively, as reported in Fig. 2.30 and Fig. 2.31. The fits of the data obtained using Eq. 2.5 for S (dashed line) and Eq. 2.6 for gt (continuous line) are also shown. The fits were obtained assuming the same common free parameters of the activation energy E_α and prefactor α_0 describing the EOR dissolution rate as a function of temperature. The values obtained from the fit are also shown in the figure.

On the other hand, the reason for the lower TED with respect to Si is still an open point demanding for further investigation. A possibility might be a different damage accumulation mechanism in the two materials, being the strain integral after SPER much lower than in Si. A subtle but relevant observation can be made considering the *I* capture radius *a* of a B atom. It is known that the rate of generation of mobile species can be written as:

$g \propto aD_I C_I$ [26], where D_I and C_I are the diffusivity and the concentration of interstitials respectively.

Moreover we have assumed that the strain integral S is proportional to the interstitials concentration. These considerations allow us to observe that the single activation energy obtained for both gt and S means that the reaction capture radius does not significantly depend on the temperature, pointing to a very low or null barrier for the BI pair formation, in agreement with previous data obtained in RED case (see g activation energy in the low-T regime in Fig. 2.25).

2.4 Conclusions

In conclusion, we investigated the B diffusion mechanism under non-equilibrium conditions in a very large temperature range (from liquid nitrogen temperature up to 800°C). This allowed to induce a relevant B diffusion by proton irradiation or during EOR defect dissolution in a Ge preamorfized sample, even at room temperature. A direct comparison with equilibrium diffusion was also made in order to unify the different results and founding a unique atomistic mechanism for B diffusion in Ge, mediated by interstitials. Under all conditions the B migration process was simulated assuming a kick-out mechanism, according to which the single diffusion event is started by the interaction of an interstitial with substitutional B, leading, with a rate g, to a mobile B that diffuses through the matrix for a mean migration length λ. It was demonstrated that neither the mechanisms through wich B becomes mobile nor those to return into substitutional sites appears to be charge-dependent. Indeed, the irradiation increases the kick-out rate proportionally to the point defect (i.e. interstitial) concentration. On the other hand, the migration path results almost unaffected by the point defect concentration within the sample but only depends on the temperature, in both equilibrium and non-equilibrium conditions. In particular, two thermal regimes have been observed (low-T and high-T) with different features.

As far as the creation of the mobile B is concerned, it is only limited by the interstitials presence, since they are characterized by a very high formation energy. Thus thermal diffusion is negligible in the low-T regime. On the other hand, if interstitials are fournished by an external process like H^+ irradiation or EOR defects dissolution, the kick-out step becomes an athermal process, only limited by the very low energy for the BI pairing. The thermal interstitials start to play a role only for temperatures higher than 600°C, when their thermal concentration becomes comparable to the one induced by implant related damage.

On the other hand, regarding the kick-in process, it follows a thermal activated trend that makes λ to increase at lower temperatures with an activation energy of -0.64 eV similar to what happens in Si. Nonetheless, this value saturates when the λ value become comparable to the mean distance of C and O impurities within the sample (~ 20 nm), that can act as a trap for the mobile species.

All the above observation are of fundamental importance in the comprehension of dopant diffusion in Ge and can be exploited in order to realize microelectronic device of better and better performances.

2.5 References

1. H. Bracht, MRS Bull., 22 (2000).
2. C. Claeys, E. Simoen, *Germanium-based technologies – from materials to devices* (Elsevier, Great Britain, 2007).
3. J.M. Bonar, A.F.W. Willoughby, A.H. Dan, B.M. Mcgregor, W. Lerch, D. Loeffelmacher, G.A. Cooke, M.G. Dowsett, J. Mater. Sci.: Mater. Electron. **12**, 219 (2001).

4. S. Uppal and A.F.W. Willoughby, J.M. Bonar and A.G.R. Evans, N.E.B. Cowern, R. Morris and M.G. Dowsett, J. Appl. Phys. **90**, 4293 (2001).
5. S. Uppal, A.F.W. Willoughbya, J.M. Bonar, A.G.R. Evans, N.E.B. Cowern, R. Morris, M.G. Dowsett, Physica B **308–310**, 525 (2001).
6. S. Uppal, and A. F.W. Willoughby, J.M. Bonar, N.E.B. Cowern, T. Grasby, R.J.H. Morris, and M.G. Dowsett, J. App. Phys. **96**, 1376 (2004).
7. W.C. Dunlap Jr., Phys. Rev. **94**, 1531 (1954).
8. W. Meer, D. Pommerrenig, Z. Angew. Phys. **6**, 369 (1967).
9. N. A. Stolwijk, *Impurities and Defects in Group IV Elements and III-V Compounds*, Vol. 22A (Springer, Berlin, 1989).
10. H. D. Fuchs, W. Walukiewicz, E. E. Haller, W. Dondl, R. Schorer, and G. Abstreiter, Phys. Rev. B **51**, 16817 (1995).
11. A. Strohm, T. Voss, W. Frank, P. Laitinen and J. Räisänen, *Z.* Metallkde **93**, 737 (2002).
12. S. M. Hu, Phys. Status Solidi B **60**, 595 (1973).
13. C. Janke and R. Jones, S. Öberg, P. R. Briddon, Phys. Rev. B **77**, 075208 (2008).
14. A. Chroneos, B. P. Uberuaga, R. W. Grimes, J. Appl. Phys. **102**, 083707 (2007).
15. A. Chroneos, H. Bracht, R. W. Grimes, and B. P. Uberuaga, Appl. Phys. Lett. **92**, 172103 (2008).
16. W. Frank, U. Gösele, H. Mehrer, and A. Seeger, *Diffusion in Crystalline Solids*, edited by G. E. Murch and A. S. Nowick (Academic, New York, 1984).
17. P. Delugas and V. Fiorentini, Phys. Rev. B **69**, 085203 (2004).
18. H. Bracht, S. Brotzmann, Mat. Sci. Semicon. Proc. **9**, 471 (2006).

19. H. Herzer, S. Kalbitzer, in: I. Ruge, J. Graul (Eds.), Proceedings of the Second International Conference on Ion Implantation in Semiconductors, Springer, Berlin,(1972).

20. M.I. Gueseva, A.N. Mansurova, Rad. Eff. **20**, 207 (1973).

21. S. Mirabella, A. Coati, D. De Salvador, E. Napolitani, A. Mattoni, G. Bisognin, M. Berti, A. Carnera, and A. V. Drigo, S. Scalese, S. Pulvirenti, A. Terrasi, and F. Priolo, Phys. Rev. B **65**, 045209 (2002).

22. D. De Salvador, E. Napolitani, S. Mirabella, G. Bisognin, G. Impellizzeri, A. Carnera, and F. Priolo, Phys. Rev. Lett. **97,** 255902 (2006).

23. Ziegler J. F., J. P. Biresack, and U. Littmark, *The Stopping and the Range of Ions in Solids* (Pergamon, New York, 1985); http:// www.srim.org.

24. E. Napolitani, D. De Salvador, R. Storti, A. Carnera, S. Mirabella, and F. Priolo, Phys. Rev. Lett. **93**, 055901(2004).

25. S. Koffel, P. Scheiblin, A. Claverie, and G. Benassayag, J. Appl. Phys. **105**, 013528 (2009).

26. N.E.B. Cowern, K.T.F. Janssen, and G.F.A. van de Walle, D.J. Gravesteijn, Phys. Rev. Lett. **65**, 2434 (1990).

27. N.E.B. Cowern, G.F.A. van de Walle, D.J. Gravesteijn, and C.J. Vriezema, Phys. Rev. Lett. **67**, 212 (1991).

28. S. Schneider, H. Bracht, M.C. Petersen, J. Lundsgaard Hansen, and A. Nylandsted Larsen, J. Appl. Phys. **103**, 033517 (2008).

29. P. Lévêque, A.Yu. Kuznetsov, J.S. Christensen, and B. G. Svensson, A. Nylandsted Larsen, J. Appl. Phys. **89**, 5400 (2001).

30. A. Mesli, L. Dobaczewski, K. Bonde Nielsen, Vl. Kolkovsky, M. Christian Petersen, and A. Nylandsted Larsen, Phys. Rev. B **78**, 165202 (2008).

31. S. C. Jain, W. Schoenmaker, and R. Lindsay, P. A. Stolk, S. Decoutere, M. Willander, H. E. Maes, J. Appl. Phys. **91**, 8919 (2002).

32. A. Carvalho,* R. Jones, and C. Janke, J. P. Goss and P. R. Briddon, J. Coutinho, S. Öberg, Phys. Rev. Lett. **99,** 175502 (2007).

33. J. Vanhellemont, and E. Simoen, J. Electrochem. Soc. **154**, H572 (2007).

34. P. Śpiewak, M. Muzyk, K.J. Kurzydłowski, J. Vanhellemont, K. Młynarczykc,P. Wabiński, I. Romandic, J. Cryst. Growth. **303**, 12 (2007).

35. T. Soma, A. Morita, J. Phys. Soc. Jpn. **32**, 357 (1972).

36. T. Soma, M. Saeki, A. Morita, J. Phys. Soc. Jpn. **35**, 146 (1973).

37. M. Dionízio Mortira, R.H. Miwa, P. Venezuela, Phys. Rev. B **70**, 115215 (2004).

38. G. Bisognin, S. Vangelista, E. Bruno, Mat. Sci. Eng. B **154–155**, 64 (2008).

39. B. C. Johnson, P. Gortmaker, and J. C. McCallum, Phys. Rev. B **77**, 214109 (2008).

40. H. Bracht, S. Schneider, J. N. Klug, C.Y. Liao, J. Lundsgaard Hansen, E. E. Haller, A. Nylandsted Larsen, D. Bougeard, M. Posselt, and C. Wündisch, Phys. Rev. Lett. **103**, 255501 (2009).

41. S. Decoster and A. Vantomme, J. Phys. D: Appl. Phys. **42**, 165404 (2009).

42. P. A. Stolk, H.-J. Gossmann, D. J. Eaglesham, D. C. Jacobson, C. S. Rafferty, G. H. Gilmer, M. Jaraíz, and J. M. Poate, H. S. Luftman, T. E. Haynes, J. Appl. Phys. **81**, 6031 (1997).

Chapter 3

Defect engineering in Ge

It is well assessed that the design of microelectronic devices relies on semiconductor materials, whose properties strictly depend upon point defects (Cfr. paragraph 1.2). For this reason, to control the concentration and the spatial distribution of point defects is of fundamental importance. Moreover, as discussed in Chapter 1, Ge is dominated by vacancies (Vs) and almost all dopants (e.g. Ga, P, Sb, As) diffuse and precipitate via a mechanism assisted by vacancies [1]. This behavior causes detrimental effects on dopant profile during thermal annealing aimed to electrically activate the implanted dopant, hampering the formation of highly doped ultra-shallow junction. As an example, Fig. 3.1 shows the as-implanted P SIMS profile (i.e. 15 keV, 5x10^{15} *P^+/cm*^{2}*,black line), compared with the ones after annealing at 500°C for 60 s (orange line) and 120 s (purple line). It can be observed a very high P diffusion that increases with annealing time. The maximum concentration of substitutional P obtained is only 5–6x*10^{19} *P/cm*^{3} *[2] while the peak observed in the first 20 nm is most likely related to the presence of inactive P-V complexes [3].Both, the large broadening of P and its deviation seem to be related to effects produced by the vacancies, thus, a proper engineering of Vs could limit such drawbacks.*

A way to reduce or even suppress vacancies, in order to avoid these undesired effects is, hence, highly demanded for the realization of ultra-shallow junctions, for new generation devices. This can be obtained by promoting vacancies annihilation with interstitials (Is), by increasing the interstitial concentration in the Ge matrix.

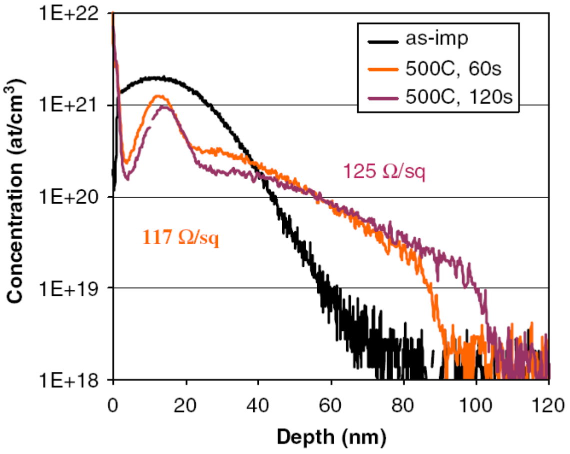

Fig. 3.1 SIMS profiles of P implanted in Ge with energy of 15 keV and fluence 5x10^{15} P$^+$/cm^2 (black line), and annealed at 500°C for 60 s (orange line), and 120 s (purple line). It can be seen that during the annealing P suffers a very high diffusion and precipitation that increases with annealing time [2, 4].

In this chapter, a way to engineering point defects in Ge is developed by using oxygen. Indeed in Si it is well assessed that during surface oxidation, a self-interstitial injection towards the bulk occurs, due to the relieve of the stress developed at Si/SiO$_2$ interface, as will be described in paragraph 3.1. This mechanism is not so effective in Ge (paragraph 3.2) due to the problems related to the instability of germanium oxide reported in section 3.2.1. In spite of this, the studies reported in section 3.2.2 reveal that I-oxygen complexes and GeO$_2$ precipitates embedded in Ge matrix may be formed. Considering that, similar to the Si case, the volume per Ge atom in the oxide is twice than in pure Ge, a mechanism of I injection from the Ge/GeO$_2$ interface, could potentially occurs. For this reason, our approach, based on O implant in Ge matrix (as described in paragraph 3.3), first of all wants to verify the formation and morphology of GeO$_2$ clusters, as reported in paragraph 3.4. Finally in paragraph 3.5, the results on the influence of these clusters on native point defects concentration, and hence on dopant diffusion, are reported.

3.1 A way to control point defects: oxygen effect in Si

Thermal oxidation process was largely studied in silicon, in the first ‘80s. It was observed that it greatly affects the impurity diffusion coefficients. These interactions are thought to arise from the oxidizing interface that acts as a source of self-interstitials. Indeed, the production of interstitials during the oxidation is a way to relieve part of the stress that develops when a unit volume of silicon turns into 2.25 unit volumes of SiO_2 [5, 6]. The atomic mechanism leading to Si emission is illustrated in Fig. 3.2. When oxygen atoms (filled circles) are inserted into Si-Si bonds, a large strain accumulates at the interface. In this situation, the Si atom (open circles) and the oxygen atom (indicated by the curved arrow) lie so near that can form a bond by breaking the bond with the Si atom in the second-layer of the substrate. Now, the Si atom which has two broken bonds can be emitted from the surface due to the lateral compressive strain [7].

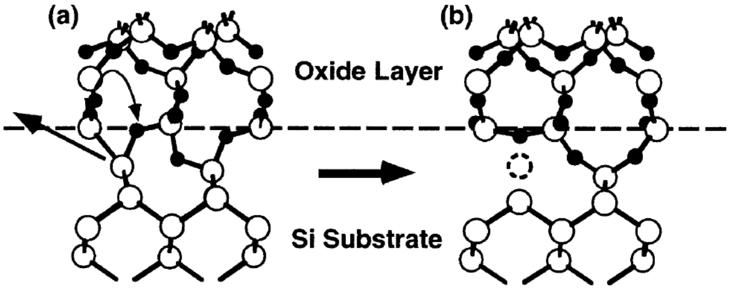

Fig. 3.2 Representation of optimized atomic structures of Si during oxidation which include three O atoms per unit cell. In particular (a) represents the structure without the interfacial Si emission, and (b) the structure after a Si atom is emitted from the interface. The dotted circle indicates the position from which the Si atom is emitted. Open circles are Si atoms and filled ones are O atoms [7].

The majority of these emitted interstitials flow into the oxide and are oxidized on its way, while a relatively small, but significant, amount flows into the substrate [8], causing an interstitial supersaturation and the so called oxidation enhanced diffusion (OED) of dopants that diffuse through a mechanism principally mediated by interstitials (i.e. B) [9]. Indeed, Fig. 3.3 shows the values of the kick-out rate (g), as described above (Cfr. section 2.2.3), extracted from B diffused profiles in inert ambient conditions (open circles) or in dry-O_2-ambient conditions (open triangles), as a function of the inverse of the temperature [10].

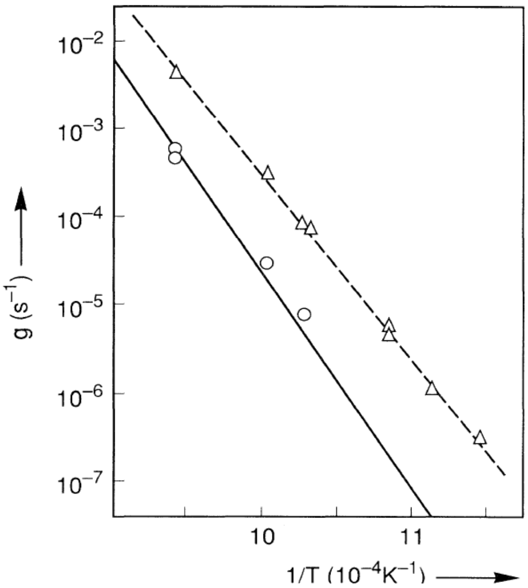

Fig. 3.3 Arrhenius plot of the kick-out rate (g) calculated for B diffusion in Si in the temperature range 600-800°C. Circles indicate inert (N_2) ambient diffusion conditions, and triangles indicate dry O_2 ambient. The solid line is a theoretical estimation while the dashed line is a guide to the eye. [10]

It can be noted that the interstitial injection process, due to the silicon oxidation, causes an increase in g by about one order of magnitude throughout the temperature range investigated (600 – 800°C). For the kick-out model, the generation rate g can be expressed as $g = g^* \, {C_I}/{C_I^*}$, where g* is the generation rate of the mobile species in equilibrium conditions, while C_I and C_I* represent the interstitials concentration in non equilibrium and equilibrium regimes, respectively. The observed increasing of g, can be ascribed to an interstitial supersaturation of ${C_I}/{C_I^*} \cong 10$.

Knowing that Ge and Si are very similar from a crystallographic point of view, as discussed in the Chapter 1, one can predict that the oxidation mechanism could be similarly used in Ge. Actually the simple oxidation process is not so effective in Ge, as will be discussed in the following.

3.2 The germanium case

Germanium oxidation was largely studied in both the past [11-14] and also recently [15-19] principally in order to investigate and minimize the active defects at the Ge/GeO_2 interface, for CMOS realization. However, there are no studies on Ge self-intestitials injection during oxidation, principally due to the instability of germanium oxide.

3.2.1 Oxidation of Ge surface and related issues

Fig. 3.4 shows the evolution of the Ge oxide thickness as a function of oxidation time during the first 120 min of thermal oxidation at low temperatures between 350°C and 450°C. A linear regime is observed, in agreement with the model developed by Deal and Grove [20] for Si oxidation, that assumes that in the early stages the oxidation process is limited by the reaction at the oxide/semiconductor interface. According to several studies [11,12,14] this initial regime represents the surface reaction between Ge and molecular oxygen:

$$Ge^{(s)} + O_2 \rightarrow GeO_2{}^{(s)}$$

where the superscript (*s)* refers to material in solid phase, at the solid-gas interface. From Fig. 3.4 it can be observed that the Ge oxidation rate increases with temperature as well as the Ge oxide thickness with the oxidation time [21].

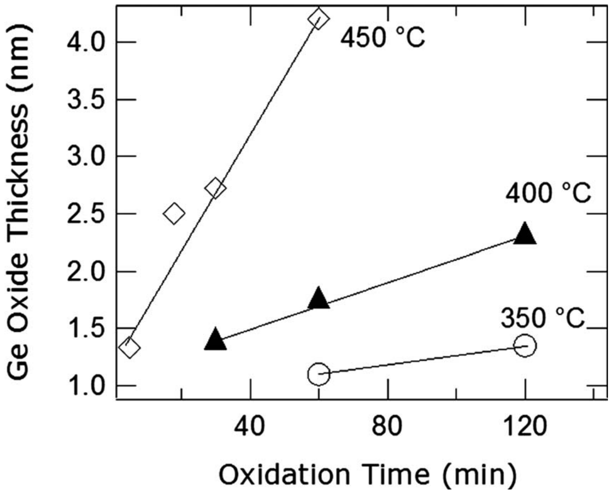

Fig. 3.4 Evolution of Ge oxide thickness as a function of oxidation time at 350°C (open circles), 400°C (closed triangles) and 450°C (open diamonds) as measured by X-ray photoelectron spectroscopy [21].

A more quantitative insight into the chemical composition of Ge oxide revealed that the as-grown layer is mainly GeO_2 with the Ge^{4+} contribution increasing with the oxide thickness, i.e., the oxidation time and temperature [21]. However in Fig. 3.5 a representative fitting of a X-ray photoelectron spectroscopy (XPS) analysis is illustrated for the oxidation at 200°C [15]. All the Ge oxidation state contributions were fitted by single Voigt functions, i.e., Gaussian functions convoluted with Lorentzian ones. It can be seen that there are four components other than that of Ge bulk (indicated with the yellow curve ‘GeB’ in the figure). In particular, the GeO_2

and the GeO components are identified by the Ge^{4+} peak and Ge^{2+} peak, respectively, while the other two Voigt functions, intermediate between the previous oxide components (identified by Ge^{1+} and Ge^{3+} peaks) indicate the occurrence of further suboxide species, namely, Ge_2O and Ge_2O_3, as suggested in Ref. [22]. This behavior is very different with respect to the Si case where only the SiO_2 component can be grown directly by oxidation of a heated substrate.

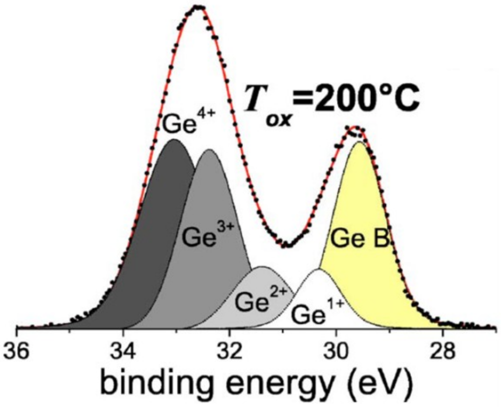

Fig. 3.5 Representative fitting analysis applied to the XPS spectrum of the oxide formed on Ge at 200 °C [15].

Unfortunately in Ge the surface quality between the Ge bulk and its native oxide tend to deteriorate during the thermal process itself because of the volatilization of GeO through the reactions:

$$Ge + GeO_2^{(s)} \rightarrow 2GeO^{(s)}$$

$$GeO^{(s)} \rightarrow GeO^{(g)}$$

where the superscript (s) refers to material in solid phase, at the solid-gas interface, as before, while the superscript (g) indicate the gaseous phase of the GeO [12]. Several studies agree that the GeO desorption process occurs even below 500°C [12, 15, 17, 23-26] with an activation energy of about 2 eV [18]. In particular, Fig. 3.6 compares the percentage of Ge oxide inside the samples during the oxidation and desorption processes as a function of the annealing temperature. The change in percentage of Ge oxides is obtained by calculating the area relative to the Ge oxide peak with respect to the total Ge area in the XPS spectrum, i.e:

$$\%Ge\ oxide = \frac{area\ (Ge\ oxide)}{area\ (Ge\ oxide + elemental\ Ge)}$$

Eq. 3.1

It can be observed that the desorption of GeO and the oxidation of Ge are likely to occur simultaneously when a Ge wafer is annealed in an oxidizing ambient. Being these two successive reactions the oxidation process causes a loss of Ge at the surface.

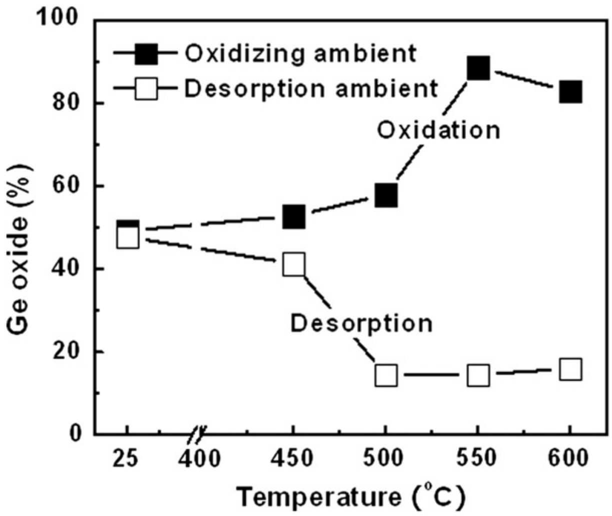

Fig. 3.6 Relative amount of germanium oxides for oxidation and desorption processes as a function of annealing temperature. [17]

This feature has hampered to employ the approach used in Si, through which a self-interstitial supersaturation is typically produced during surface oxidation as discussed above. Regarding this, several studies show that by employing an appropriate cap on top of the GeO_2 film during the annealing, the desorption process can be decreased [26]. Furthermore, the problem related to GeO desorption could be solved if it was possible to create GeO_2 complexes inside the Ge matrix. The studies present in literature on this regard will be discussed on the following.

3.2.2 Oxygen related defects Ge and GeO_2 precipitation in Ge

Recently the interaction of Ge self-interstitials (I) with interstitials oxygen atoms (O_i) in Ge crystals was both experimentally and theoretically studied [27-29]. In particular, from conventional and high resolution Laplace Deep-Level Transient Spectroscopy (DLTS) techniques Markevic et al. [28-29] observed that the defects responsible for the DLTS peaks, in electron irradiated and annealed oxygen-rich Ge crystals, can be associated with oxygen related defects. Indeed, since they are detectable at temperatures above ~ -93°C (180 K), that correspond to the temperature at which self-interstitials become mobile [30], these defects can be attributed to I-O_i complexes. Ab-initio modeling predicts two stable configurations of I-O_i complexes, depending on the neutral or positively charged state of the considered self-interstitial, whose structures are illustrated in Fig. 3.7 (a) and (b), respectively.

In Ref. [28] it was argued that the I-O_i complex becomes mobile at temperatures higher than 50°C. Diffusion and interaction of these defects with other interstitials oxygen atoms, which are the most abundant sinks in oxygen-rich Ge crystals, result in the formation of I-O_{2i} complexes. Moreover, from experimental results, it was speculated that there are at least two configurations for these complexes, among which the most stable has orthorhombic symmetry [29].

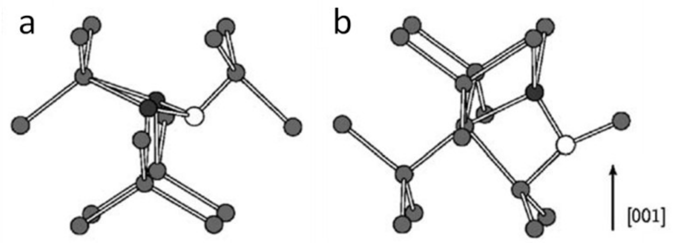

Fig. 3.7 Lowest energy structures of the *I*-Oi defects that form considering neutral (a) or positively charged (b) self-interstitial atoms. Germanium and oxygen atoms are represented in grey and white, respectively. Interstitial Ge atoms are highlighted in darker gray [27].

These complexes can also evolve in extended defects. In fact, in an early study concerning the solubility of oxygen in Ge, Kaiser and Thurmond [31] observed the appearance of a broad infrared (IR) absorption band centered at a wavelength of 11.5 µm in the IR absorption spectra of oxygen-rich Ge samples annealed above 600°C, as evident from the comparison between the as-grown (B) and annealed (C) spectra, reported in Fig. 3.8. The curve A in Fig. 3.8 shows, indeed, the IR absorption spectrum of oxygen-free Ge. It is known that the concentration of O_i in Ge is determined by the peak amplitude α_{max} of the 856 cm^{-1} absorption band through the relation: $C_{O_i}[at/cm^3] = 1.5 \cdot 10^{17} \cdot \alpha_{max}$ (at RT) and with α_{max} expressed in cm^{-1}. This quantity does not necessarily reveal the total oxygen concentration, as some of the oxygen may also be present under the form of GeO_x precipitates grown during thermal treatment. The origin of the 11.5 µm broad band, indeed, was attributed to this kind of precipitates .

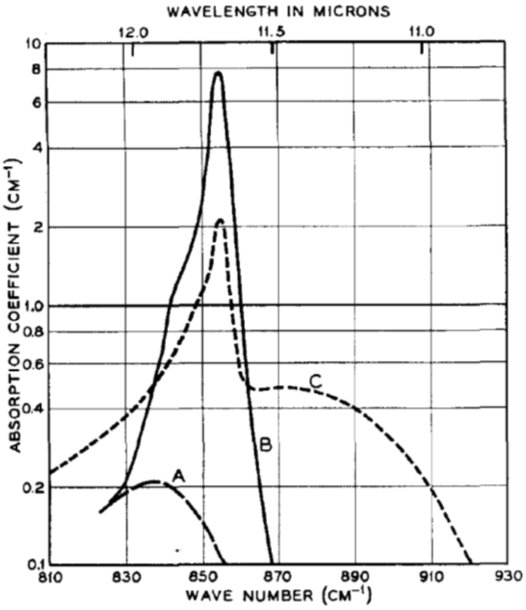

Fig. 3.8 Absorption coefficient of oxygen doped germanium before (B) and after (C) annealing at 610°C for 66 hr. Curve A shows a small lattice absorption of oxygen free germanium [31].

These results were confirmed also by De Gryse et al. [32, 33] through a new procedure based on the Bergman-Milton spectral representation of the dielectric function of a composite material [34-36]. In particular, they assumed that the precipitates are composed of a mixture of two phases, i.e. the amorphous Ge and the GeO_2, and that they can be spherical or disc-like. In Fig. 3.9, the results of this procedure (dashed line) is reported for the experimental IR absorption spectrum of an oxygen-rich Ge sample after a 560 °C, 240 h annealing (continuous line). The results seem to indicate that germanium oxide precipitates of different morphology may be formed. Nonetheless, the details outcoming from this procedure, such as shape and stoichiometry of the precipitates, have not been experimentally verified yet.

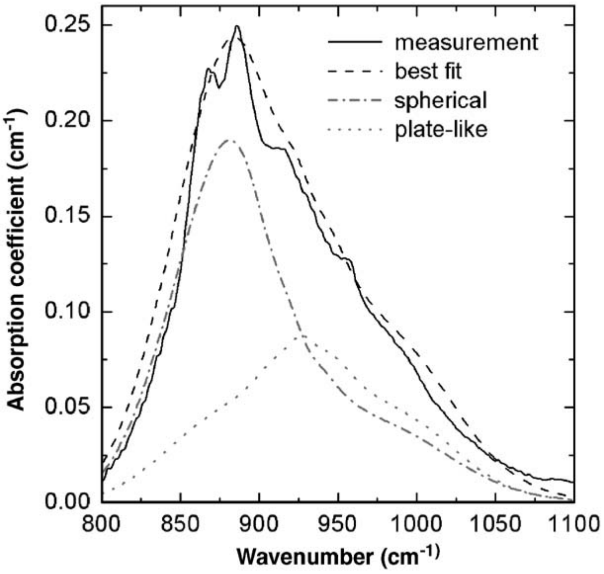

Fig. 3.9 Simulated (dashed line) and experimental (continuous line) spectra assuming a mixture of spherical (dash-dot line) and disc-like (ditted line) GeO_2 precipitates [32].

All of these results testify that it is possible to obtain germanium oxide inside the Ge matrix, overcoming the problems related to the thermal oxidation as discussed above.

In spite of this there are no evidence on the role of GeO_2 in altering the interstitials concentration in Ge. In principle, however, considering that the Ge densities in Ge and in GeO_2 are respectively:

$\rho_{Ge}(Ge) = 4.8 \times 10^{22}\, at/cm^3$ and $\rho_{Ge}(GeO_2) = 2.4 \times 10^{22}\, at/cm^3$,

the volume per Ge atom in the oxide is twice than in pure Ge. Thus a mechanism of *I* injection from the Ge/GeO_2 interface, similar to that occurring in Si, as described in the previous section, could potentially occur. For this reason our study wants to shed light on this phenomenon. All the analysis performed with this aim will be discussed in the next paragraphs.

3.3 Experimental

As discussed before, our study aims to observe the formation of GeO_2 precipitates inside a Ge matrix in order to verify if, similarly to what happens during silicon oxidation, they can induce a self-interstitial injection inside the Ge matrix due to relaxation of the strain accumulated at Ge/GeO_2 interface.

In order to perform this study, a (001) Czochralski Ge crystal (Cz-Ge) , *p*-type, with resistivity of ~0.001 Ω/cm, was implanted at room temperature (RT) with 4×10^{14} O^+/cm^2 at 235 keV. In this way the projected range R_p, results at about 450 nm [37], as schematically illustrated in Fig. 3.10. Some implanted samples were then annealed at 650°C for different times from 30 to 180 min in ultrapure N_2 flowing gas with a proximity capping with pure Ge samples. Cross-sectional transmission electron microscopy (XTEM) analysis were done with a 200 keV Jeol 2010F instrument, and secondary ion mass spectrometry (SIMS) analysis were conducted for O profiling with a Cameca IMS-4f instrument using a 14.5 keV Cs^+ analyzing beam. This kind of samples were prepared in order to observe if the annealing at 650°C induces the formation of such oxygen-related clusters and, if it is the case, to observe the morphology of these clusters.

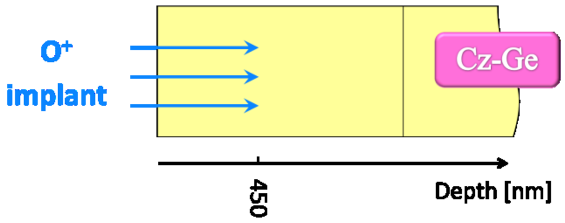

Fig. 3.10 Scheme of the experiment. The Czochralski Ge (Cz-Ge) sample is irradiated with O^+ at 235 keV, with fluence $4x10^{14}$ O^+/cm^2. The calculate projected range of the implant is around 450 nm [37]. Finally annealing process are performed at 650°C in order to investigate O evolution.

In parallel, the same experimental procedure of O implantation (235 keV O^+, 4×10^{14} O^+/cm^2 at room temperature) and annealing (650°C 30 – 180 min) was performed on a molecular beam epitaxy grown Ge (MBE-Ge) containing a B multidelta structure (five narrow B-doped layers B-*δs*, positioned at 100, 300, 500, 700 and 1000 nm) as schematized in Fig. 3.11.

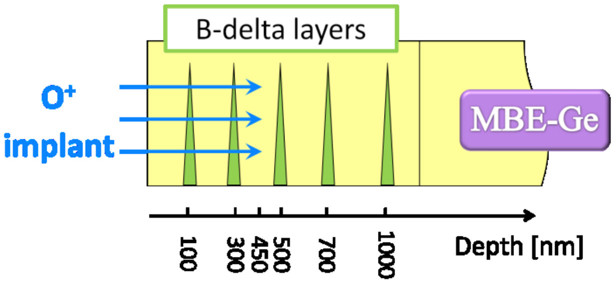

Fig. 3.11 Scheme of the experiment. The sample with five B-δs located at 100 nm, 300 nm, 500 nm, 700nm and 1000 nm respectively is epitaxially grown by MBE on a Ge substrate. Then the sample is irradiated with a 235 keV O^+, $4x10^{14}$ O^+/cm^2. The calculate projected range of the implant is around 450 nm [37]. Finally annealing process are performed at 650°C in order to investigate B diffusion.

It is worth noting that, before the implants, the MBE-Ge samples were preannealed at 600°C, 1 h under N_2 flux to eliminate any possible postgrowth defects. Then, for B SIMS profiling a Cameca IMS-4f instrument with a 3 keV O_2^+ analyzing beam was used. So, since B diffused in Ge through a mechanism exclusively mediated by interstitials, as discussed in Chapter 2, this kind of sample allows to indirectly monitor the interstitial supersaturation eventuallygenerated within the sample by the oxygen related clusters.

3.4 GeO_2 nanocrystals formation in Ge: morphological analysis

First of all we focus the attention on the Cz-Ge sample. Fig. 3.12 shows the O profile in the Cz-Ge sample before (solid line) and after annealing at 650°C for 30 (open squares) and 120 (open triangles) min.

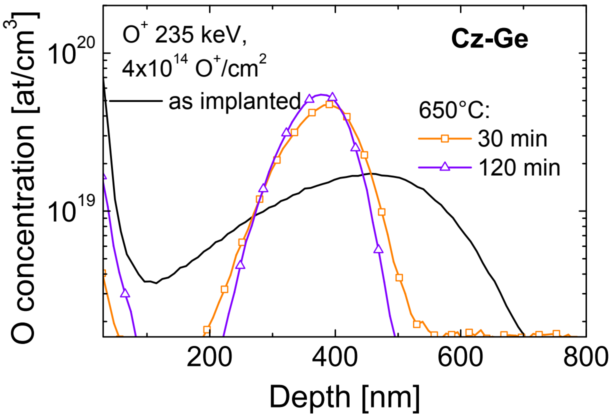

Fig. 3.12 Oxygen profile in the Cz-Ge sample after implantation (O^+ 235 keV, $4x10^{14}$ O^+/cm^2 at RT, black line) and after annealing at 650°C for 30 min (orange line plus squares) and 120 min (violet line plus triangles). No oxygen loss occurs during the annealing, while a significant O accumulation is observed at a shallower depth with respect to the implanted profile.

Comparing the profiles, it can be observed that the annealing does not induce any O loss. On the other hand, a significant shrinkage of the O profile is clearly visible. In particular, after annealing the O profile shows a wide peak at around 4/5 of the R_p, stable up to 3 h at 650°C. According to the experimentally measured [38] and theoretically calculated [39] values of O diffusivity in Ge, we can assume that it is:

$$D_O(Ge) = 0.39 \times exp\left({}^{-2.05[eV]}/_{k_B T} \right) [cm^2/s]$$

Eq. 3.2

where k_B is the Boltzman constant and T is the absolute temperature. It can be calculated that after the 30 min annealing at 650°C, the diffusion length is ~700 nm, long enough to justify a complete flattening of the profile. As it can be seen from Fig. 3.12 this is not the case.

Moreover, the O behavior observed in Fig. 3.12 recalls what happens in the separation by implanted oxygen (SIMOX) technology used in Si [40], as can be observed in Fig. 3.13, where a shrinkage of the O profile after an annealing at 1320°C is evident [Fig. 3.13 (b)], with respect to the as implanted profile [Fig. 3.13 (a)].

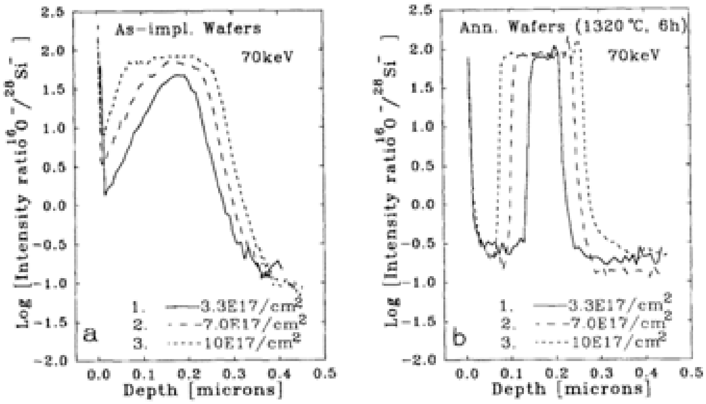

Fig. 3.13 SIMS oxygen profiles of the Si as-implanted (a) samples with fluencies 3.3x10^{17} O$^+$/cm^2 (solid lines), 7x10^{17} O$^+$/cm^2 (dashed lines) and 10x10^{17} O$^+$/cm^2 (dotted lines) and after annealing at 1320°C 6 h (b) for SIMOX process. [40]

It can be noted, however, that differently from SIMOX process, in our case a clear shift of the O distribution is also observed in O SIMS profiles of Fig. 3.12, indicating that another phenomenon occurs in this case. Furthermore, our result recalls what happens in the very high-dose (~10^{18} O$^+$/cm^2) O implantation in Ge [41], where the formation of a buried layer of GeO_2 was observed, but in our case, the O implant dose is four orders of magnitude lower, so we are in a totally different implant regime.

In order to deeply study this phenomenon, cross sectional TEM analysis were performed in the Cz-Ge samples before and after annealing. On this respect, Fig. 3.14 (a) and (b) show the XTEM of Cz-Ge samples implanted with O 235 keV, 4×10^{14} O^+/cm^2 and annealed at 650°C for 30 and 120 min, respectively.

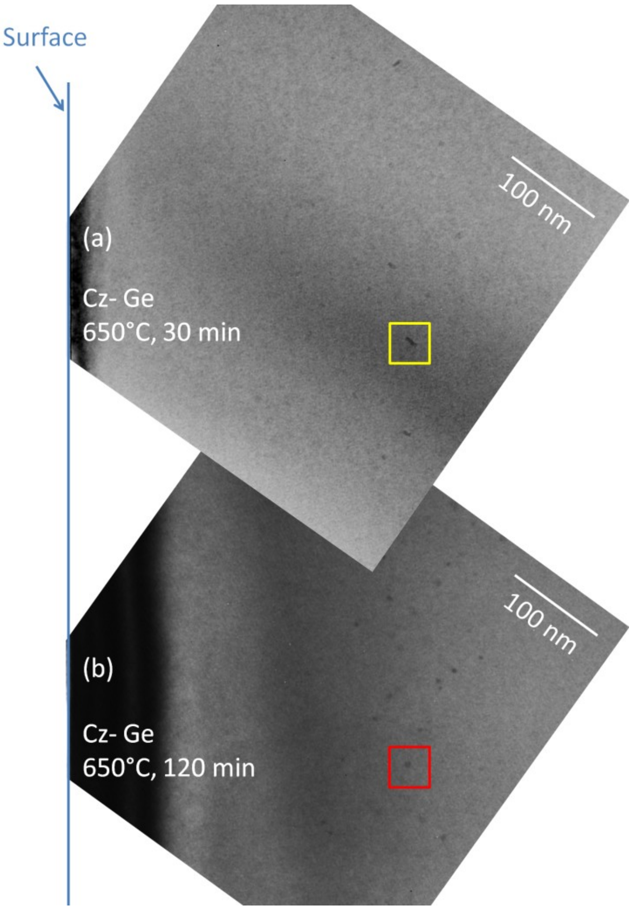

Fig. 3.14 Cross-sectional TEM micrograph of Cz-Ge sample implanted with O^+ 235 keV, $4x10^{14}$ O^+/cm^2 at RT, and annealed at 650 ◦C for (a) 30 min and (b) 120 min, revealing the presence of GeO2 nanoclusters at a depth of about 370 nm.

In both cases, it can be seen that around ∼ 370 nm, which corresponds to the depth where O accumulates (Fig. 3.12), many self-interstitial-rich nanoclusters are present (also evidenced with the yellow and red squares).
The detail of the structures of the nanoclusters after the two different annealing are reported in the high-resolution (HR) images observed along the [011] zone axis presented in Fig. 3.15 and Fig. 3.16 for the Cz-Ge samples implanted at 650°C for 30 min and 120 min, respectively.

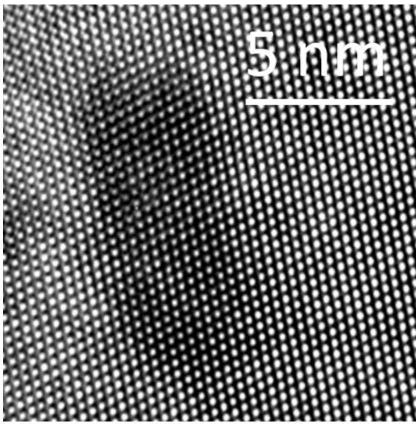

Fig. 3.15 HR-TEM images of a typical nanocluster in the Cz-Ge sample implanted with O^+ 235 keV, $4x10^{14}$ O^+/cm^2 at RT, and annealed at 650°C for 30 min evidencing the elongated shape.

From these figures it is evident that the dimension of these nanoclusters are between 5 and 10 nm. Moreover, from Fig. 3.15 it can be noted that after the annealing at 650°C for 30 min the nanoclusters show an elongated shape, while after 120 min (Fig. 3.16) they have a spherical, crystalline structure. The lattice fringes in correspondence of the nanocluster, visible in Fig. 3.16, indeed, strongly differ from those present in the surrounding Ge matrix.
In fact, the crystalline structure of the nanocluster in Fig. 3.16, interposed between the Ge crystalline lattice, causes the formation of typical Moiré fringes.

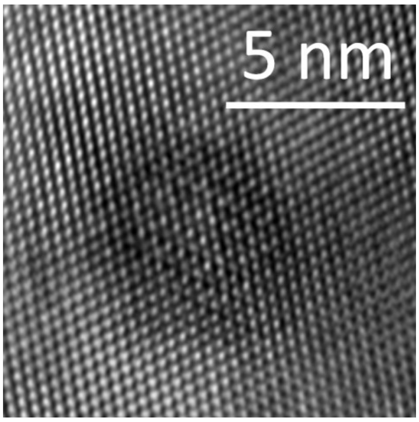

Fig. 3.16 HR-TEM images of a typical nanocluster in the Cz-Ge sample implanted with O^+ 235 keV, $4x10^{14}$ O^+/cm^2 at RT, and annealed at 650°C for 120 min evidencing the spherical shape. The formation of typical Moiré fringes indicate the crystalline structure of the nanocluster.

As a proof, after indexing the fast Fourier transform of the HR image of the nanocluster, some supplementary diffraction spots appear, in addition to the Ge crystalline spots as showed in Fig. 3.17 (a). In particular, the spot indicated with a red arrow in Fig. 3.17 (a) is related to the interplanar distance d=4.3 Å, compatible with the {100} lattice planes of the rutile GeO_2 [42]. After filtering the HR-TEM with the frequencies characteristic of these planes, the image of the nanocluster showing the {100} planes has been obtained and is reported in Fig. 3.17 (b).

It can be noted that the observed GeO_2 nanoclusters exhibit a thermal stability much larger than the EOR defects in Ge, which dissolve at about 400°C, as discussed in Chapter 2. In order to explain the O accumulation, observed also after 180 min at 650°C annealing, it should be noted that: (i) TEM analysis on the as-implanted sample revealed a highly defective crystalline structure, confirming the subamorphizing implant; (ii) the O accumulation region corresponds to the depth along the ion track where the rate of energy loss versus depth (and thus the crystal damage rate) is maximum [37].

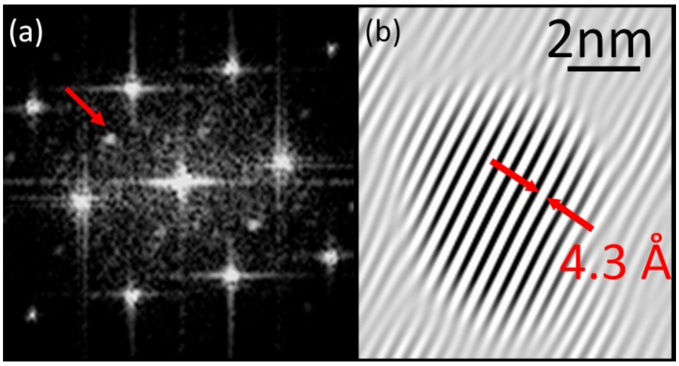

Fig. 3.17 (a) The fast Fourier transform diffraction pattern of the HR image of the cluster reported in Fig. 3.16 with the arrow indicating one of the supplementary diffraction spots of crystalline GeO_2. (b) The image of the cluster showing the planes compatible with {100} GeO_2 planes obtained after filtering the HR-TEM of Fig. 3.16.

Thus, the O accumulation can be promoted by some crystal defects as, for example, distorted or broken bonds and point defects created by the implantation and acting as stable gettering centers for O, as discussed in the previous section. Moreover, our results regarding the change in shape that occurs from 30 min to 120 min annealing at 650°C agrees well with the hypothesis assumed to simulate infrared spectra of oxide precipitates in Cz-Ge in Ref. [32,33], according to which the shape of GeO_2 clusters should be spherical and disclike at 560°C but only spherical at 620°C.

Once established that in our experimental condition GeO_2 nanoclusters are formed inside the Ge matrix and that they undergo a structural transformation from an elongated to a spherical crystalline phase, it is now important to investigate if they can affect the concentration of point defects in bulk Ge.

3.5 Evidence of interstitials injection through GeO_2 nanocrystals

In order to study the concentration of interstitial within Ge samples we used an indirect mechanism. Indeed, knowing that B diffusion in Ge is mediated by interstitials (Cfr. Chapter 2), monitoring B diffusion at different depths within the sample, it can be traced back the interstitial concentration as a function of depth. Fig. 3.18 shows the B profiles of the MBE-Ge as grown (orange line) and after O^+ 235 keV, 4×10^{14} O^+/cm^2 implantation (dashed line). It can be seen that the two profiles are indistinguishable, so the RED that occurs during implantation is negligible in this case.

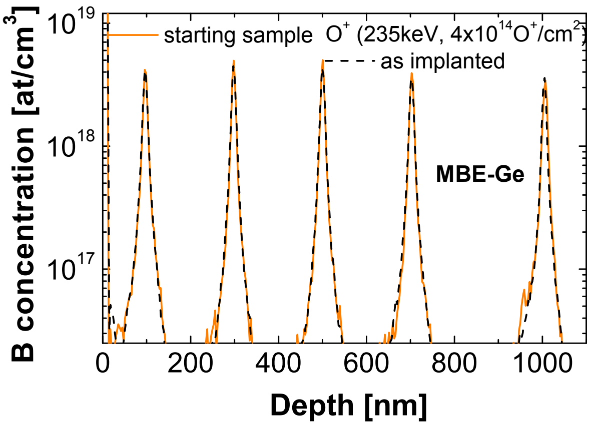

Fig. 3.18 Boron SIMS profiles of the sample grown by MBE containing five B-δs located at 100 nm, 300 nm, 500 nm, 700 nm and 1000 nm respectively, after an annealing at 600°C for 1 h (orange continuous line) or after O^+ 235 keV, $4x10^{14}$ O^+/cm^2 implantation (dashed line).

In Fig. 3.19, indeed, the B profiles of the MBE-Ge after O^+ 235 keV, 4×10^{14} O^+/cm^2 implantation (dashed line) and after annealing at 650°C for 30 min (squares), 120 min (triangles), and 180 min (stars) are compared. A clear broadening of B-δs is visible already after 30 min at 650°C (for which the equilibrium diffusion is negligible [43]), going on up to 120 min. The profiles at 120 min and 180 min are, indeed, equivalent.

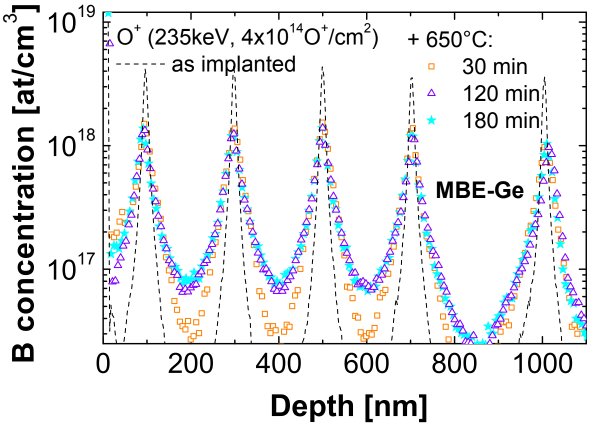

Fig. 3.19 Boron SIMS profiles in MBE-Ge sample after O^+ 235 keV, 4×10^{14} O^+/cm^2 implantation (black dashed line), and after annealing at 650°C for 30 min (orange open squares), 120 min (violet open triangles), and 180 min (cyan stars). A homogeneous broadening of the B profiles is observed, evidencing a transient enhanced diffusion of B lasting less than 120 min at 650°C.

This behavior indicate that B undergoes an evident transient enhanced diffusion (TED) related to the O implantation and exhausted after 120 min at 650°C. In addition, Fig. 3.19 shows that such TED of B is homogeneous from the surface down to 1.2 μm, not limited to the region of GeO_2 nanoclusters, that, as seen before, are located at around 370 nm from the surface, so in between the 2nd and the 3rd B-δs.

In order to verify the origin of the observed B TED, a 265 keV Ne^+ implantation, at a fluence of $3x10^{14}$ Ne^+/cm^2 was performed on MBE-Ge samples. In particular the energy and fluence of the Ne^+ implant were chosen to give a similar crystal damage of the O implant (O^+ 235 keV, 4×10^{14}

O^+/cm^2), in order to have a similar nuclear energy loss, as calculated by SRIM [37], as shown in Fig. 3.20.

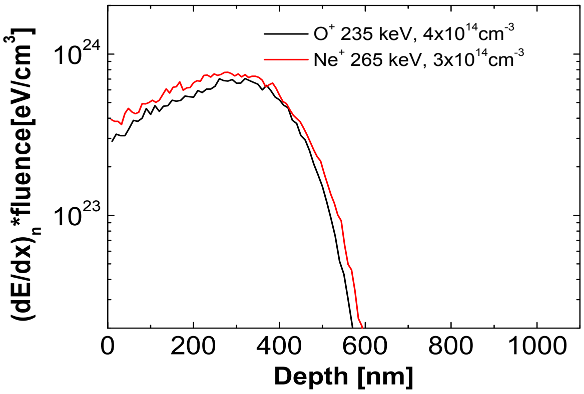

Fig. 3.20 Total energy loss by nuclear collisions $(dE/dx)_n$ for the 235 keV, 4×10^{14} O^+/cm^2 (black line) or 265 keV, 3×10^{14} Ne^+/cm^2 (red line) implants, as obtained by SRIM simulation [37].

After the Ne^+ implant, the sample was annealed at 650°C for 60 min. In this sample a negligible broadening of B profiles is observed (green solid line in Fig. 3.21) with respect the one obtained at the same temperature, during a shorter annealing (i.e. 30 min) when O is present inside the sample (open squares) as shown in Fig. 3.21. This is counterproof that the injection of interstitials is related to the presence of O.

If we compare the boron TED with previous results on GeO_2 nanoclusters formation and changes, we can affirm that there is a strong relationship between these two phenomena. This is an evidence that, in our case, the embedded GeO_2 nanoclusters formed inside the matrix could act as the self-interstitial source as discussed in section 3.2.2. In this respect, we can assume that the self-interstitials are created at ~370 nm and diffuse, just after 30 min, at least up to a depth of ~1000 nm, in which the B diffusion is visible. So, using the equation $\lambda = \sqrt{D_I/t}$, (where D_I is the self-interstitial diffusivity, while λ and t are the length and the time of the diffusion, respectively), a lower limit for the self-interstitial diffusivity at 650°C can be obtained: $D_I(650°C) > 2 \times 10^{-12}\ {cm^2}/_{s}$.

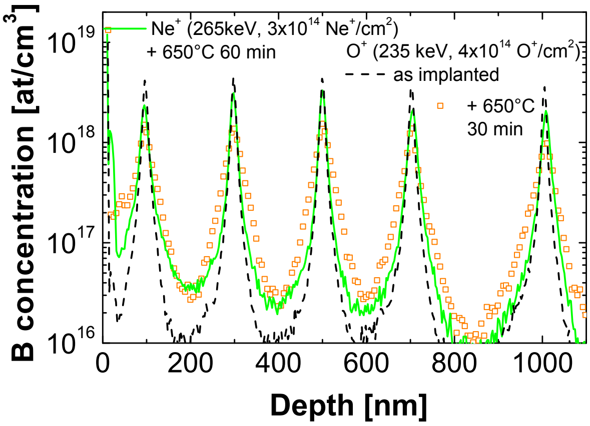

Fig. 3.21 Boron SIMS profiles in MBE-Ge starting sample (i.e. after annealing at 600°C, 1h, dotted line) and after O^+ 235 keV, 4×10^{14} O^+/cm^2 plus annealing at 650°C for 30 min (orange open squares) and after Ne^+ 265 keV, 3×10^{14} Ne^+/cm^2 plus annealing at 650°C for 60 min (green line).

These data show that self-interstitials, once formed, can affect the Ge lattice at long distances and in a non-negligible way, remarking that the weak role of self-interstitials in Ge can be related only to their quite large formation energy with respect to vacancies. Moreover, the homogeneous broadening of the B-δs indicates that self-interstitials are reflected by the surface, causing a flat self-interstitial supersaturation, in agreement with Refs. [44] and [45].

In order to quantitatively study the self-interstitial supersaturation, we fitted the B profiles by means of a χ^2 optimization of numerical simulations based on the *g*-λ diffusion model, largely discussed in section 2.2.3. Here, *g* gives the B-self-interstitial interaction rate leading to one B diffusion event, while λ is the mean length of B migration per each diffusion hop. B diffusivity is given by $D_B = g\lambda^2$. The model was applied to all the B δs, and Fig. 3.22 shows the simulation curves (continuous lines) for 30 and 120 min annealing, in particular of the 3rd B-δ, accounting for the very good quality of the fits.

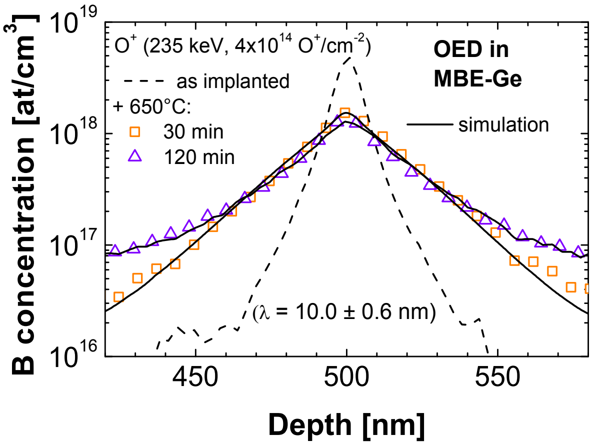

Fig. 3.22 Oxidation-enhanced diffusion produces non-Gaussian shape: boron SIMS profiles in the MBE-Ge sample after O$^+$ 235 keV, 4×10^{14} O$^+$/cm^2 implantation (black dashed line) and after annealing at 650°C for 30 min (orange open squares) and 120 min (violet open triangles). Solid lines are simulations based on *g-λ* diffusion model.

The average number of diffusion events (*gt*, being *t* the annealing time) for each B atom in the 0–30 and 30–120 min annealing windows, obtained by the simulations, are reported in Fig. 3.23. It can be seen that they differ by about one order of magnitude going from 2.39 ± 0.17, after the first 30 min annealing, to 0.24 ± 0.04 during the successive 90 min at 650°C, confirming that the oxidation enhanced diffusion of B is transient.

Moreover, given the model results, and extrapolating the B diffusivity at 650°C in equilibrium conditions from Ref. [43], we are able to calculate that D_B in the 0–30 min annealing is enhanced by a factor of ~2x10^5. Actually, the OED of B in Si is much lower (D_B enhancement of ~10, as discussed in paragraph 3.1 Refs. [10, 46]), but the equilibrium self-interstitial density in Si is much larger than in Ge, weakening the effect of self-interstitial injection during OED in Si. In our case, if all the implanted O atoms are involved in GeO_2 clusters (5 nm in diameter and distributed over the 150-nm-wide peak of Fig. 3.12), a cluster density of ~1x10^{16} cm^{-3} is expected.

This is only a lower limit, since smaller GeO_2 clusters cannot be excluded. Thanks to the high surface-to-volume ratio, the self-interstitial injection by the GeO_2 nanoclusters can be very effective, justifying the larger self-interstitial enhancement in our case.

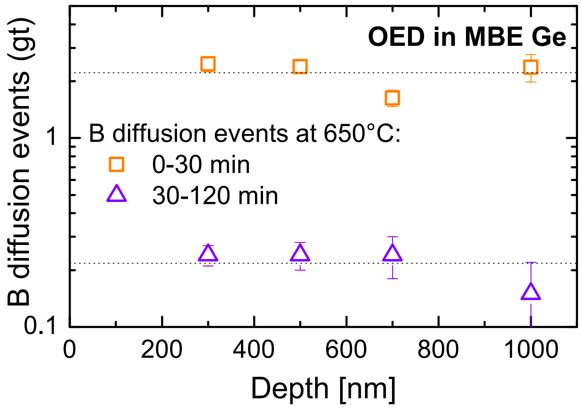

Fig. 3.23 Number of B diffusion event (gt, where t is the annealing time) as a function of the depth calculated for samples implanted with O^+ 235 keV, 4×10^{14} O^+/cm^2 at RT and then annealed for 30 min (orange squares) or for 120 min (so for additional 90 min, violet triangles). The dashed lines are guidelines for the eye.

Finally, it can be noted that the B diffused profiles show a non-Gaussian shape, with large exponential tails, revealing a quite long migration length ($\lambda \sim 10$ nm), as reported in Fig. 3.22. This behavior is different from what expected according to what demonstrated in Chapter 2 in the high temperature regime. Indeed, according to the results obtained for radiation enhanced diffusion (i.e. B diffusion during 200 keV H^+ implant) at 700°C, reported in Fig. 3.24, we would have expected a Gaussian-like shape in this high-T regime. In particular, it can be observed that the B diffusion length obtained under equilibrium diffusion at 755°C or under proton irradiation at 700°C (reported in Fig. 3.24) is about 10 times lower (λ~2-3nm) than that obtained during OED in Ge (Cfr. section 2.2.6).

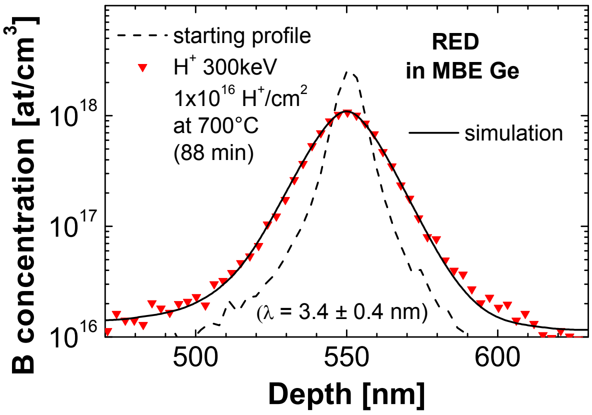

Fig. 3.24 Radiation Enhanced Diffusion at 700°C produces a Gaussian profile: boron SIMS profiles in the starting sample (i.e. the as-grown sample after 600°C 1h, dashed line) and after 200 keV H^+ implant performed at 700°C (red triangles). Solid line is the simulated profile based on *g-λ* diffusion model.

Despite the similar temperatures, the significant disparity in λ indicates that the migration length per each B diffusion event is markedly longer when GeO_2 nanoclusters are present. It should be noted that λ could be related to the availability of vacancies, which can trap the diffusing B atom, reducing the migration length. Indeed, differently from the RED case, in this case, while the interstitial population is increased by the presence of GeO_2 nanoclusters, vacancies can be only thermally generated. Therefore, the longer λ in the presence of GeO_2 nanoclusters is compatible with an undersaturation of vacancies, probably due to recombination with self-interstitials injected from GeO_2 nanoclusters through the reaction $V + I \rightarrow 0$

3.6 Conclusions

In conclusion, as schematically illustrated in Fig. 3.25, we showed that O implantation in crystalline Ge followed by a 650°C annealing induces the formation of GeO_2 nanoclusters. These defects, undergo a structural transformation, between 30 min and 120 min at 650°C, from an elongated shape to a spherical form, with a structure compatible with that of crystalline GeO_2. At the same time, a large enhancement of self-interstitial density (depicted in Fig. 3.25 with blue dotted segment), exhausted after 120 min at 650°C, is revealed by B diffusion experiments.

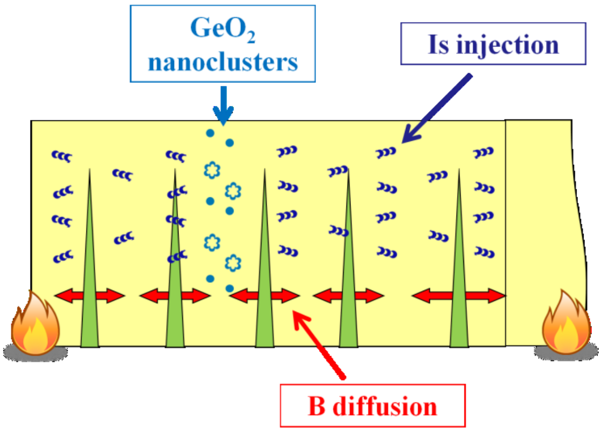

Fig. 3.25 Pictorial representation of the obtained results. The 650°C annealing of an O rich Ge sample causes the formation of GeO_2 nanoclusters. During the structural transformation of these nanoclusters from elongated to spherical and crystalline a huge Ge self-interstitial injection occurs over the whole sample. This injection is testified by a large Oxidation Enhanced Diffusion of B in Ge that occurs also at depth more than 600 nm far to the interstitial source (i.e. GeO_2 nanoclusters).

It is proposed that a significant self-interstitial injection occurs as a result of the relaxation of the strain at Ge/GeO_2 interface during nanoclusters formation, similar to what happens in Si under surface oxidation.

Based on the B diffusion shape and its simulations, this system is compatible with a significant vacancy impoverishment. Such a noteworthy imbalance of point defect density in favor of self-interstitials allows a significant change in the basic properties of crystalline Ge, dominated by vacancies under equilibrium conditions.

3.7 References

1. C. Claeys, E. Simoen, *Germanium-based technologies – from materials to devices* (Elsevier, Great Britain, 2007).
2. A. Satta and E. Simoen, R. Duffy, T. Janssens, T. Clarysse, A. Benedetti, M. Meuris, and W. Vandervorst, Appl. Phys. Lett. **88**, 162118 (2006).
3. V. I. Fistul, A. G. Yakovenko, A. A. Gvelesiani, V. N. Tsygankov, and R. L. Korchazhkina, Inorg. Mater. **11**, 457 (1975).
4. E. Simoen, A. Satta, A. D'Amore, T. Janssens, T. Clarysse, K. Martens, B. De Jaeger, A. Benedetti, I. Hoflijk, B. Brijs, M. Meuris, W. Vandervorst, Mat. Sci. Semicon. Proc. **9**, 634 (2006).
5. S.M. Hu, Mat. Sci. Eng. R **13**, 105 (1994).
6. P.M. Fahey, P.B. Griffin, and J.D. Plummer, Rev. Mod. Phys. **61**, 289 (1989).
7. M. Uematsu , H. Kageshima, K. Shiraishi, Comp. Mater. Sci**. 24**, 229 (2002).
8. K. Taniguchi, Y. Shibata, and C. Hamaguchi, J. Appl. Phys. **65**, 2723 (1989).
9. S. Matsumoto, Y. Ishikawa, and T. Niimi, J. Appl. Phys. **54**, 5049 (1983).
10. N.E.B. Cowern, G.F.A. van de Walle, D.J. Gravesteijn, and C.J. Vriezema, Phys. Rev. Lett. **67**, 212 (1991).

11. W.L. Jolly and W.M. Latimer, J. Am. Chem. Soc. **74**, 5757 (1952).
12. J.T. Law And P. S. Meigs, J. Electrochem. Soc . **104**, 154 (1957).
13. J. Sládková, Czech. J. Phys. B **27**, 154 (1977).
14. Y. Wang, Y.Z. Hu, and E.A. Irene, J. Vac. Sci. Technol. A **12**, 1309 (1994).
15. A. Molle, Md. N.K. Bhuiyan, G. Tallarida, and M. Fanciulli, Appl. Phys. Lett. **89**, 083504 (2006).
16. R. Xie, W. He, M. Yu, and C. Zhu, Appl. Phys. Lett. **93**, 073504 (2008) and references therein.
17. J. Oh, J.C.Campbell, Mat. Sci. Semicon. Proc. **13**, 185 (2010).
18. S. K. Wang, K. Kita, C.H. Lee, T. Tabata, T. Nishimura, K. Nagashio, and A. Toriumi, J. Appl. Phys. **108**, 054104 (2010).
19. S. Baldovino, A. Molle, and M. Fanciulli, Appl. Phys. Lett. **93**, 242105 (2008).
20. B. E. Deal and A. S. Grove, J. Appl. Phys. **36**, 3770 (1965).
21. F. Bellenger, M. Houssa, A. Delabie, V. Afanasiev, T. Conard, M. Caymax, M. Meuris, K. De Meyer, and M. M. Heynsa, J. Electrochem. Soc. **155**, G33 (2008).
22. D. Schmeisser, R.D. Schnell, A. Bogen, F.J. Himpsel and D. Rieger, G. Landgren and J.F. Morar, Surf. Sci. **172**, 455 (1986).
23. K. Prabhakaran, F. Maeda, Y. Watanabe, and T. Ogino, Appl. Phys. Lett. **76**, 2244 (2000).
24. X.-J. Zhang, G. Xue, A. Agarwal, R. Tsu, M.-A. Hasan, J.E. Greene, and A. Rockett, J. Vac. Sci. Technol. A **11**, 2553 (1993).
25. D.A. Hansen, and J.B. Hudson, Surf. Sci. **292**, 17 (1993).
26. K. Kita, S. Suzukiy, H. Nomuraz, T. Takahashi, J. J. Appl. Phys. **47**, 2349 (2008).

27. L.I. Khirunenko, Yu.V. Pomozov, M. Sosnin, V.P. Markevich, L.I. Murin, V.V. Litvinov, A. Carvalho, R. Jones, J. Coutinho, S. Öberg, P.R. Briddon, Mat. Sci. Semicon. Proc. **11**, 344 (2008).
28. V.P. Markevich, Mat. Sci. Semicon. Proc. **9**, 589 (2006).
29. V.P. Markevich, A.R. Peaker, S.B. Lastovskii, L.I. Murin, V.V. Litvinov, V.V. Emtsev, L. Dobaczewski, Physica B **404**, 4533 (2009).
30. H. Haesslein, R. Sielemann, and C. Zistl, Phys. Rev. Lett. **80**, 2626 (1998).
31. W. Kaiser, and C.D. Thurmond, J. Appl. Phys. **32**, 115 (1961).
32. O. De Gryse, J. Vanhellemont, P. Clauws, Mat. Sci. Semicon. Proc. **9**, 246 (2006).
33. O. De Gryse, P. Vanmeerbeek, J. Vanhellemont, P. Clauws, Physica B **376–377**, 113 (2006).
34. D.J. Bergman, Phys. Rep. **43**, 377 (1978).
35. G.W. Milton, J. Appl. Phys. **52**, 5286 (1981).
36. A.R. Day, M.F. Thorpe, J. Phys.: Condens. Matter **11**, 2551 (1999).
37. Ziegler J. F., J. P. Biresack, and U. Littmark, The Stopping and the Range of Ions in Solids (Pergamon, New York, 1985); http://www.srim.org.
38. J.W. Corbett, R.S. McDonald, and G.D. Watkins, J. Phys. Chem. Solids **25**, 873 (1964).
39. V. Gusakov, J. Phys. Condens. Matter **17**, S2285 (2005).
40. Y. Li, J. A. Kilner, P. L. F. Hemment, A. K. Robinson, J. P. Zhang, K. J. Reeson, C. D. Marsh, and G. R. Booker, Nucl. Instr. and Meth. Phys. Res. B **64**, 750 (1992).
41. N.M. Ravindra, T. Fink, and W. Savin, T.P. Sjoreen, R.L. Pfeffer, L.G. Yerke, R.T. Lareau, J.G. Gualtieri, and R. Lux, C. Wrenn, Nucl. Instrum.Meth. B **46**, 409 (1990).

42. T. I. Milenov, V. I. Dimov, P. M. Rafailov, and M. M. Gospodinov, Appl. Phys. A **92**, 643 (2008).
43. S. Uppal, A. F. W. Willoughby, J. M. Bonar, N. E. B. Cowern, T. Grasby, R. J. H. Morris, and M. G. Dowsett, J. Appl. Phys. **96**, 1376 (2004).
44. H. Bracht, S. Schneider, J. N. Klug, C. Y. Liao, J. Lundsgaard Hansen, E. E. Haller, A. Nylandsted Larsen, D. Bougeard, M. Posselt, and C.Wündisch, Phys. Rev. Lett. **103**, 255501 (2009).
45. S. Schneider and H. Bracht, Appl. Phys. Lett. **98**, 014101 (2011).
46. M. Miyake, J. Appl. Phys. **57**, 1861 (1985).

Chapter 4

Sb in Ge: a promising candidate for optoelectronics

It is well assessed that it is possible to modulate electrical and optical properties of semiconductors by properly varying both doping or strain (Cfr. Paragraph 1.3). These features could be exploited to realize high-speed microelectronic applications or Si-based light emitting devices. In particular, as widely discussed in Chapter 1, the characteristics of crystalline Ge, such as the very high charge carrier mobility and the very small difference (136 meV) between the indirect and direct band-gap, make it a very interesting material for new generation, more performing optoelectronic devices. In this respect,a very large effort has been recently developed in order to realize a Si-compatible laser using Ge as an active medium. However, achieving direct band-gap in Ge and improving the Ge light emitting efficiency are still huge challenges.

In this chapter, we will propose a new promising approach to properly engineering the Ge energy bands to use it as a light source, that can represent a real breakthrough in the field of telecommunications. Our approach, based on the use of highly Sb doped Ge as virtual substrate will be described in paragraph 4.1. However, the first step that must be overcome to realize our idea stems from the issues related to Sb incorporation in Ge, a review of which is reported in paragraph 4.2. In paragraph 4.3 the promising features of laser annealing process in melting regime, largely used in the past to obtain highly doped Si, will be described. Then, our results on high Sb incorporation and electrical activation in Ge, by using laser annealing will be largely reported in paragraph 4.4 and 4.5 in the cases of implanted or molecular beam epitaxy grown samples.

4.1 Methods to enhance direct recombination

As largely described in Chapter 1 (Cfr. paragraph 1.3), in order to obtain a proper band-gap engineering to increase direct electron-hole recombination, both tensile strain and n-type dopant approaches have been tried. In spite of this, the objective of an efficient Ge-laser has not been reached yet because of the issues related to the high tensile strain and high dopant concentration needed to transform Ge in a direct band-gap semiconductor.

In order to overcome these issues, a method that employs at the same time both strain and doping is highly demanded. In this respect, we propose an innovative approach based on the use of Sb doped Ge substrates. Indeed, while being a n-type dopant for Ge, Sb is characterized by a covalent radius much higher than that of Ge, as reported in Table 4.1. Moreover Sb covalent radius is similar to the Sn one (Table 4.1). In this respect, recently, $Ge_{1-y}Sn_y$ alloys have been the object of an extensive study, since they can already furnish a substrate for tensile Ge, while absorbing differential stress caused by the heteroepitaxy lattice mismatch, thanks to their softness [1]. However, being $Ge_{1-y}Sn_y$ metastable materials, they cannot be produced in bulk form, so $Ge_{1-y}Sn_y$ films have been grown by MBE and sputtering [1]. Major problems encountered in applying $Ge_{1-y}Sn_y$ alloys are related to the high Sn segregation in Ge and to the poor thermal stability of the grown materials [1]. For these reasons, the objective of a 2% Ge strained on $Ge_{1-y}Sn_y$ films, needed to transform Ge in a direct band-gap semiconductor (Cfr. paragraph 1.3), has not been achieved yet.

However, the similar features of Sn and Sb indicate that also by introducing an high concentration of substitutional Sb into Ge matrix it should be possible, in principle, to obtain a GeSb layer with bigger lattice parameter than that of Ge, like for $Ge_{1-y}Sn_y$ alloys.

	Atomic radius [Å]
Ge	1.22
Sb	1.4
Sn	1.41

Table 4.1 Values of atomic radius of Ge, Sb and Sn [2].

This layer could hence act as a substrate for tensile Ge, as schematized in Fig. 4.1. On the other hand, since Sb is a n-type dopant for Ge, a proper band engineering could make electrons coming from the Sb doped Ge substrate to transfer into the undoped Ge tensile layer, where they can hence recombine emitting photons. It is worth noting that, differently from what done in literature so far, the dopants would be in the substrate and not in the Ge tensile film. Indeed, the absence of dopant impurities within the Ge layer can avoid any related scattering of the charge carriers.

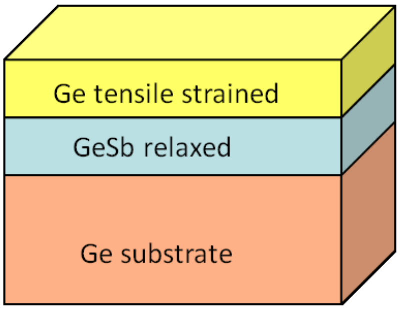

Fig. 4.1 Schematic representation of the innovative idea consisting of the use GeSb relaxed as a virtual substrate to growth Ge tensile strained film in order to obtain a proper Ge band-gap engineering that could be exploited for Ge-based light emitter.

The main problem related to the use of this original approach is related to the difficulty to obtain extremely high concentrations of substitutional and active Sb in Ge, due to its very low solubility in this matrix ($1.2\text{x}10^{19}$ Sb/cm^3 [3]). Moreover, the doping process itself is a very challenging issue, leading to severe Ge damaging or high segregation effects, as will be reviewed in the next paragraph.

4.2 Related issues on Sb doped Ge

Antimony is a very heavy atom if compared to Ge. Thus, if it is introduced in Ge by ion implantation it can severely damage the Ge matrix up to create, when the fluence increases, a permanent damage consisting of the sample swelling and the formation of surface cratering, as revealed by cross-sectional scanning electron microscopy (XSEM) image in Fig. 4.2 (a). It has been suggested that the formation of porous Ge is the consequence of voids formation that is driven by the minimization of dangling bond energy [4].

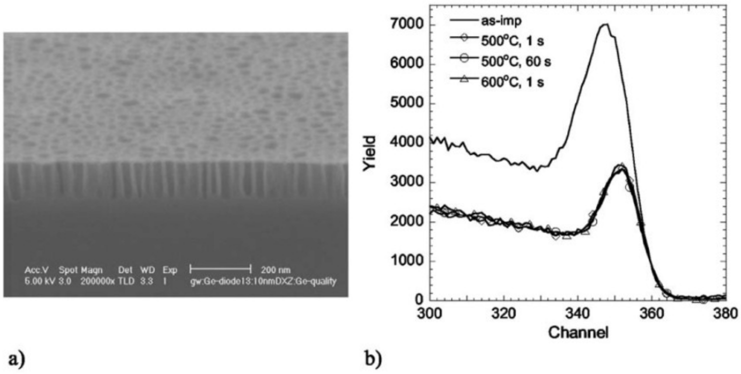

Fig. 4.2 Cross sectional-SEM image of Ge implanted with 70 keV Sb at a fluence of 10^{15} Sb^+/cm^2 (a). While panel (b) shows c-RBS spectra of Ge layers, doped with 70 keV $3x10^{15}$ Sb^+/cm^3, after implantation (continuous line) and after annealing at 500 °C for 1 s (line plus diamonds), and 60 s (line plus circles), and at 600 °C for 1 s (line plus triangles) [5].

Moreover, this very high damaging results irreversible, persisting even after high temperature annealing, as shown by RBS measurements in the channeling mode reported in Fig. 4.2 (b) [5, 6]. This characteristic limits the use of implantation to put high Sb concentration in Ge, as also discussed in

Chapter 1. So, in order to have high incorporation of this dopant, also above the solid solubility limit, it is necessary to use a nonequilibrium technique such as molecular beam epitaxy (MBE).

Nonetheless, with this technique, active Sb concentrations higher than $2x10^{20}$ Sb/cm^3 (more than one order of magnitude higher than equilibrium solid solubility) have been never obtained [7]. This can be principally related to the segregation and precipitation of Sb during epitaxial growth. In particular, Sb segregation is strictly connected to the very high diffusivity of Sb in Ge.

Several studies [7, 8] obtained that the segregation of Sb increases with increasing the growth temperature. It was detected, indeed, that temperatures lower than 200°C are needed to avoid Sb segregation to the surface. This is also visible in Fig. 4.3, in which, at growth temperatures higher than 200°C the sheet resistance dramatically increases (i.e the doping concentration decreases) because of the large segregation of Sb in Ge.

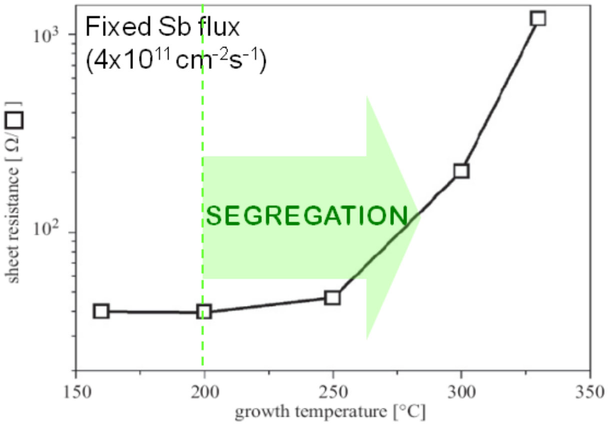

Fig. 4.3 Measured sheet resistances of a 200 nm-thick Sb doped Ge layer as a function of the substrate growth temperature. The Ge growing rate was 0.5 Å/s and the antimony flux $4x10^{11}$ Sb/cm^2 s. The green dashed line indicated the temperature over which the phenomenon of Sb segregation is observed [7].

The cause of this high segregation in Ge (higher than in Si) has been attributed to a reduced energy barrier for Sb to jump toward the surface [8].

Moreover, it was also observed that, increasing the flux of Sb atoms evaporated during the deposition of a 200 nm doped Ge layer (grown at a fixed substrate temperature of 160°C) the sheet resistence measured decreases with increasing doping flux up to 1.6x10^{12} Sb/cm^{2} s, and increases after this value (Fig. 4.4). This result is in contrast with the better electrical conductivity expected in corrispondence of a higher doping flux, if all dopant atoms are activated.

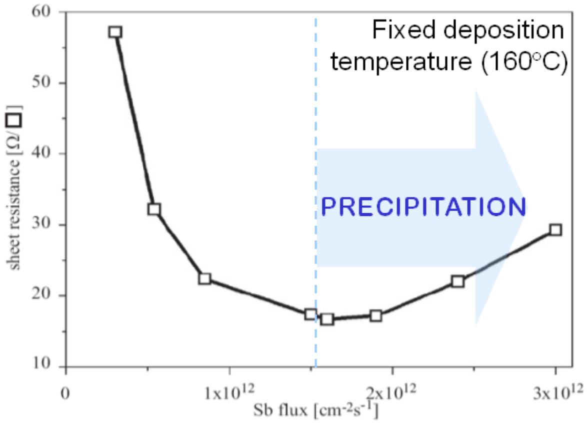

Fig. 4.4 Measured sheet resistances of a 200 nm-thick Sb doped Ge layer as a function of the Sb flux. The Ge growing rate was 0.5 Å/s and the growth substrate temperature was 160 °C. Light blue dashed line indicate the flux over which the sheet resistance increases due to the Sb precipitation [7].

This anomaly is correlated to a drastic reduction of the active carrier concentration in the Ge structure. Indeed, Fig. 4.5 shows that for a Sb flux of 9x10^{11} Sb/cm^{2}s the doping profile is constant (red line plus squares) and comparable with secondary ion mass spectroscopy (SIMS) profile (red line). On the other hand, for the higher Sb flux (3x10^{12} Sb/cm^{2} s) the active dopant profile (black line plus circles) is completely different to the SIMS measurement (black line). In this case, the electrical carrier concentration is not constant over the Sb doped Ge structure. Indeed, the carrier concentration first increases with depth achieving a maximum of 1.6x10^{20} Sb/cm^3 (a factor of about 4 smaller than the chemical profile) and then decreases to 6x10^{19} Sb/cm^3 with increasing layer thickness. So, at this high antimony flux not all Sb atoms are electrically active in the Ge layer due to Sb precipitation [7].

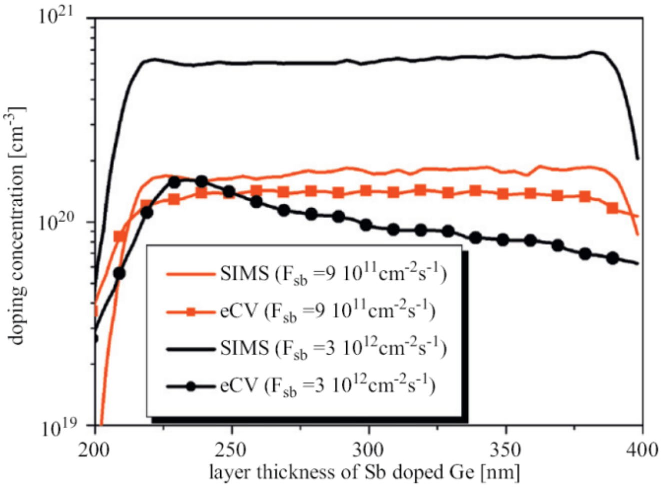

Fig. 4.5 Comparison of electrical (eCV measurement, line plus symbols) and chemical (SIMS analysis, lines) measurement on incorporation of Sb doped Ge layer with Sb fluxes of 9x10^{11} Sb/cm^2 (red lines) and 3x10^{12} Sb/cm^2 s (black lines). The Ge growth rate was 0.5 Å/s, and the growth substrate temperature was 160 °C [7].

In any case, in order to develop the Ge-based light emitter by improving the new approach described above it is necessary, first of all, to overcome the issues related to Sb incorporation in Ge and, then, to study electrical activation, thermal stability and strain effects of very high Sb doped Ge. With this aim we have used laser annealing in melting regime in order to promote Sb incorporation in Ge. This technique, indeed, has very high potentialities as will be discussed in the next section.

4.3 Laser annealing in melting regime

The laser thermal annealing in melting regime has numerous advantages over the conventional used techniques [e.g. rapid thermal annealing (RTA)] especially for the case of Ge, which has a relatively low melting point (937°C). Indeed, in pulsed laser annealing, the rapid deposition of a high energy density into the near surface region (in times on the order of several nanoseconds, which is about nine orders of magnitude shorter than those typical of a RTA) leads to the surface melting. The high diffusivity characteristic of the liquid phase (10^{-5} – 10^{-4} cm^2/s [9,10]) allow the implanted dopants to redistribute over the molten layer, before a liquid phase epitaxial (LPE) regrowth occurs.

Furthermore, another advantage of laser annealing over RTA is related to the fact that the recrystallization of the melted region takes place under conditions far from equilibrium due to the very high velocity of the liquid/solid (l/s) interface (several m/s). Under this condition, the interfacial distribution coefficient, defined as $k' = C_s/C_l$ (being C_s and C_l the solute concentration at the interface in the solid and liquid phase, respectively), is much greater than the corresponding equilibrium value $k_0 = (C_s/C_l)_{eq}$ (e.g. the distribution coefficient for Sb in Si is 0.023 under equilibrium conditions and becomes 0.7 when Sb is incorporated with a growth velocity of 2.7m/s [9,10]). This allows to obtain very high active dopant concentrations (even higher than the solid solubility) since the very fast l/s interface freezes the dopant before it can diffuse across the interface to maintain the equilibrium [9,10]. This behavior is evidenced in Fig. 4.6 [11], in which the sheet resistance (R_s) of a Ge sample implanted with P at 15 keV, with a fluence of $1x10^{15}$ P^+/cm^2, at 0°C, and then annealed with RTA (red line plus squares) or by laser annealing (blue line plus asterisks) are shown as a function of junction depth. The sheet resistance corresponding to the maximum solid solubility ($2x10^{20}$ P/cm^3, pink line plus triangles) is also plotted as a reference. It can be seen that laser annealing leads to a lower R_s than the RTA case, for the same junction depth, even if still higher than that expected with an active concentration as high as the solid solubility limit because the implanted fluence is not sufficient to reach this concentration value.

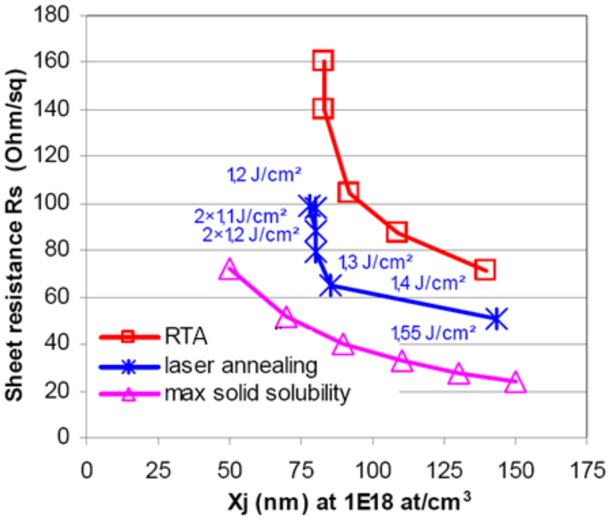

Fig. 4.6 Measured sheet resistance as a function of the junction depth of Ge implanted with P 15 keV, with a fluence of 1×10^{15} P^+/cm^2, annealed with various laser energy densities with single and double pulses (blue asterisks) or after RTA (red squares), compared with calculated sheet resistance corresponding with the maximum solid solubility (2×10^{20} P^+/cm^3 [3]) [11].

Ion implantation and laser annealing have been particularly successful for Si doping in the ‘80s, but in Ge very few studies are present in literature. Thus, a deep systematic study is highly demanded in order to exploit this technique to improve dopant activation also in Ge. In this chapter a detailed study of Sb incorporation and activation in Ge is hence reported, as described in the following.

4.4 Incorporation of Sb in the laser melting regime: implanted samples

4.4.1 Experimental

Experiments were performed on *p*-type, Ge low resistivity Czochralski (100) crystalline wafers. Samples were implanted with Sb at 50 keV, with a fluence of $6.4\text{x}10^{15}$ Sb^+/cm^2, either at the liquid nitrogen temperature (LN_2T) or at 300°C, as schematically depicted in Fig. 4.7. The implanted profile has a projected range R_p of about 20 nm, as calculated by the SRIM code [12]. The samples implanted at 300°C, crystalline after Sb implant, were further amorphized for about 60–70 nm at room temperature using a 60 keV, $8\text{x}10^{14}$ Ge^+/cm^2 ion beam in order to increase the energy absorption during the following laser annealing [9,10].

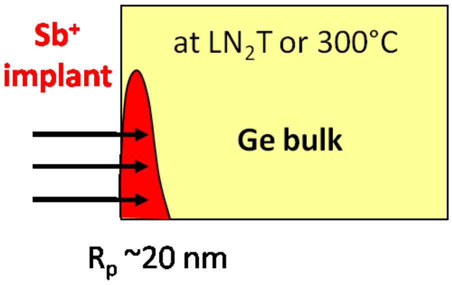

Fig. 4.7 Scheme of the Ge sample implanted with Sb at 50 keV, with a fluence of $6.4\text{x}10^{15}$ Sb^+/cm^2, at the liquid nitrogen temperature (LN_2T) or at 300 °C. The implanted profile has a projected range R_p of about 20 nm, as calculated by the SRIM code[12].

Part of the samples were then melted by irradiation with a pulsed laser. In particular, two different lasers were used: a frequency doubled neodymium-doped yttrium aluminum garnet (Nd:YAG) laser with wavelength $\lambda_{Nd:YAG}$=532 nm and pulse duration (τ) of 12 ns, located in the laboratories of the University of Catania, and a XeCl excimer laser with wavelength λ_{exc}=308 nm and a pulse duration of 28 ns, located in the laboratories of the CNR-IMM (Rome).

In particular, the Nd:YAG laser has a circular shape with a diameter of about 5 mm and is characterized by a Gaussian energy-density profile with a full-width-half-maximum (FWHM) of ~ 2 mm, as represented in Fig. 4.8. In the following, we will refer to the energy-density peak (indicated with the green arrow in Fig. 4.8) to indicate the used irradiation fluence of the Nd:YAG laser.

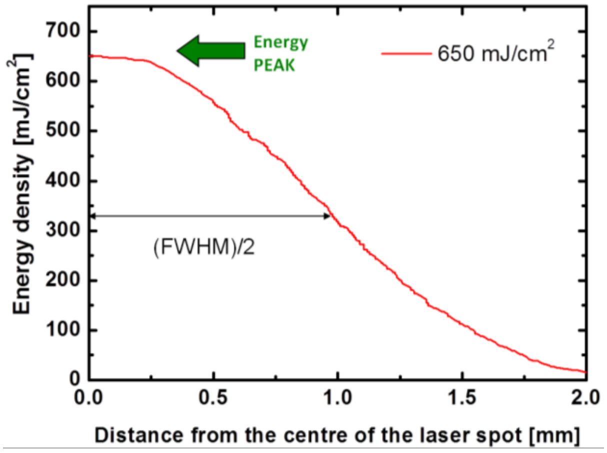

Fig. 4.8 Energy density profile as a function of the distance from the center of the laser spot for the Nd:YAG laser. In particular, the energy density profile reported has a peak of 650 mJ/cm^2 evidenced with the green arrow and a FWHM of 2 mm.

On the other hand, the XeCl excimer laser is characterized by a square spot of 5x5 mm^2, where the energy density profile is homogeneous over the whole spot area.

All these different characteristics of the two lasers are summarized in Table 4.2.

In all cases, the energy density was tuned by a continuously variable beam splitter and measured by a power and energy meter. All the used energy densities are higher than the threshold to melt the Ge surface [13,14] as verified by reflectivity measurements.

	Nd:YAG	*excimer*
λ [nm]	532	308
τ [ns]	12	28
Spot shape	circle	square
Spot dimension [mm]	5	5
Enegy-density profile	Gaussian	rectangular
Environment	air	vacum

Table 4.2 Diffferent characteristics of the used lasers (i.e Nd:YAG and XeCl excimer lasers)

Rutherford backscattering spectrometry (RBS) analysis were carried out with a 3.5 MeV HVEE Singletron accelerator, using a 2 MeV He^+ beam, both in random (r-RBS) and channeling (c-RBS) along the <100> and <111> axes configurations, in order to determine the Sb fluence and concentration profile and to investigate the Sb lattice location, respectively.

Furthermore, chemical and electrical profiles have been analyzed by means of secondary ion mass spectrometry (SIMS) and a spreading resistance profiling (SRP), respectively. In particular, Sb SIMS profiling was performed at the University of Padova, using a CAMECA IMS 4f instrument, with a 5.5 keV Cs^+ analysing beam, while SRP analysis was carried out at CNR-IMM laboratories in Catania using a Solid State Measurements, 150 Spreading Resistance Probe, interfaced with an IBM personal computer with a custom-designed software.

Finally, structural analysis were performed. In particular, cross-sectional transmission electronmicroscopy (XTEM) analysis were done with a 200 keV Jeol 2010 instrument, while, selected samples were also observed by scanning electron microscopy (SEM) in order to check the surface morphology.

4.4.2 Damage recovery

Fig. 4.9 (a) shows the SEM image of the surface of a Ge sample implanted with 50 keV Sb, 6.4x10^{15} Sb^+/cm^2, at the LN_2T. Even if the implant is performed at such a low temperature, this high-fluence Sb implantation has caused a structural modification of the Ge surface, with the formation of a well defined porous structure that remains even after thermal annealing at temperatures as high as 600°C. Moreover, r-RBS analysis indicate an Sb loss of 30% as a consequence of the implantation process, likely related to self-sputtering during this structure formation.

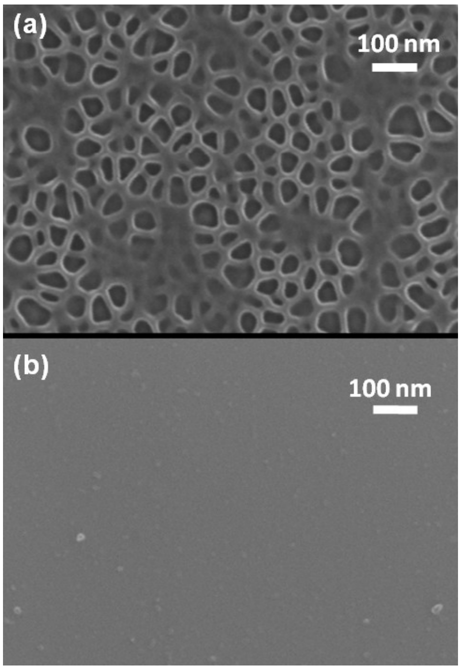

Fig. 4.9 SEM images of a Ge sample implanted with 50 keV Sb, at a fluence of 6.4x10^{15} Sb^+/cm^2, at the LN_2T just after the implant (a) and after the irradiation with a single Nd:YAG laser pulse at 880 mJ/cm^2.

Nonetheless, laser irradiation is able to totally recover the damage by melting the surface beyond the amorphous/crystalline interface and subsequent liquid phase epitaxial (LPE) regrowth. Indeed, the SEM image of the surface of a Ge sample implanted with 50 keV Sb, 6.4x10^{15} Sb^+/cm^2, at the LN_2T and then irradiated with a single pulse with Nd:Yag laser, at 880 mJ/cm^2, reported in Fig. 4.9 (b), shows a smooth and good quality surface, where only the normal roughness of the material has been evidenced, while, as verified by RBS analysis, no further Sb loss is observed.

The only way to avoid this voids formation, and hence the related Sb loss during the implant is to performe the implantation above the recrystallization threshold of amorphous Ge, i.e. at around 300°C [15]. Indeed, the same Sb implant (i.e. 50 keV Sb, 6.4x10^{15} Sb^+/cm^2) performed at 300°C does not induce any surface roughening, likely due to the dynamic annealing of the damage during the implant itself, and, as showed by r-RBS measurements, the Sb fluence is preserved too. Moreover, the implanted Ge remains crystalline after implantation, as previously said. However, also in this case, laser annealing eliminates any residual defects produced by Sb implantation, in such a way that most of Sb can occupy a substitutional location in the Ge lattice, as reported in the next sections.

4.4.3 Incorporation and redistribution of Sb in Ge

Laser annealing strongly modifies the Sb implanted profile. The very high Sb diffusivity in the liquid phase makes the Sb profile to change its shape during a melting laser irradiation before LPE regrowth occurs. Fig. 4.10 shows the depth over which the implanted Sb at 50 keV, with a fluence of 6.4 x10^{15} Sb^+/cm^2 at 300°C and then amorphized (Cfr. section 4.4.1) redistributes under laser irradiation (Nd:YAG laser pulses with energy density of 1350 mJ/cm^2) by gradually increasing the number of subsequent laser pulses, repeated with a frequency of 1 Hz (red circles). The FWHM of the Sb profile measured by r-RBS analysis, in fact, indicates that it broadens with respect the as-implanted profile. This means that gradually more Sb is able to reach the depth of the molten region, finally redistributing over the whole melted depth within five subsequent pulses. Then, further pulses do not change the final Sb depth, that depends only on the laser energy-density, i.e., on the depth of the molten region.

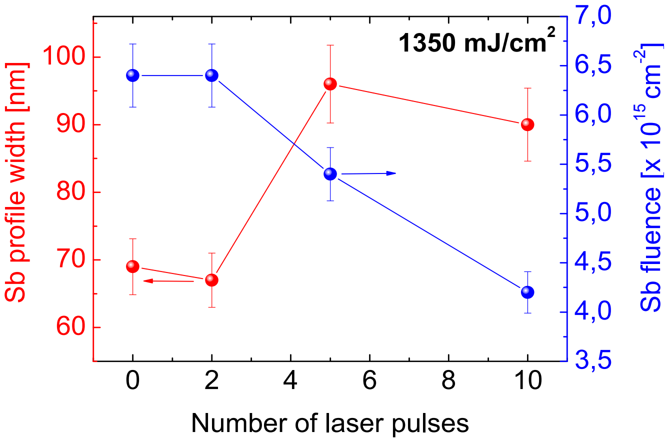

Fig. 4.10 Depth over which the implanted Sb (i.e 50 keV Sb, at a fluence of 6.4x10^{15} Sb$^+$/cm^2 at 300 °C and then amorphized) redistributes under laser irradiation with Nd:YAG laser pulse at 1350 mJ/cm^2 as a function of the number of subsequent laser pulses, repeated with a frequency of 1 Hz (red circles, left scale), and the correspondent Sb fluence present in the sample obtained by r-RBS (blue circles, right scale).

The Nd:YAG laser pulse lasts for 12 ns, while the surface remains liquid for about 70 ns when lasered at this energy fluence, as obtained by *in situ* reflectivity measurements. Hence, since the melting occurs while the laser is irradiating the sample, the LPE growth lasts for about 60 ns. In particular, since the melt depth is about 95 nm, as measured by the broadening of Sb profiles obtained by r-RBS in Fig. 4.10 (red circles), we can estimate that the liquid/solid (l/s) interface moves with a velocity of about 1.6 m/s during the LPE process. On the other hand, as discussed in the previous section, the Sb diffusivity in the liquid phase (D^l_{Sb}) is of the order of 10^{-4} cm^2/s [9,10,16,17].

If we consider the diffusion length as $\lambda = \sqrt{D_{Sb}^{l}\, t}$, where t is the duration of the liquid phase at the Sb depth (i.e., ~55 ns), we can estimate that the implanted Sb, originally peaked at about 20 nm, as obtained by SRIM simulations,[12] can move at maximum for ~10–20 nm in each laser pulse. Thus, since the melt depth is 95 nm, several pulses (three to six) are needed to obtain a complete redistribution of the implanted Sb, in agreement with the data in Fig. 4.10. Unfortunately, as reported still in Fig. 4.10, a measure of the total Sb fluence present in the sample obtained by r-RBS (blue circles) indicates that laser annealing can induce also a dopant loss due to Sb outdiffusion, that becomes relevant as the number of subsequent irradiations increases. As a consequence, the number of pulses by which irradiating the sample has to be evaluated as a compromise between the wanted redistribution depth of the implanted Sb and the amount of Sb that remains.

Fig. 4.11 (a)–(d) show the r-RBS and c-RBS spectra along the <100> and <111> axes (black and red lines, respectively) in the sample implanted with Sb 50 keV, 6.4x10^{15} Sb^{+}/cm^{2} at 300 °C, amorphized and then irradiated with five pulses of Nd:YAG laser at 1350 mJ/cm^{2}. Panels (a) and (c) report the Ge signals and panels (b) and (d) the Sb ones. In particular, in Fig. 4.11 (b) and (d) the correspondent depth scale of the Sb profile is also plotted. Furthermore, dashed lines in panels (a) and (c) are the spectra along the <100> and <111> axes in a Ge single crystal, reported as a reference. The Ge channeling spectra, reported as red lines in Fig. 4.11 (a) and (c), demonstrate that the sample is effectively epitaxially recrystallized.

The quality of the crystal can be observed considering the minimum yield χ_{min}, i.e. the minimum yield of RBS spectrum along the channel direction normalized to the yield in a random direction. In particular it can be seen that χ_{min}(Ge) is about 5% for both axes in the c-Ge and in the lasered GeSb sample, as reported in Table 4.3, indicating a good crystalline quality of the lasered sample, comparable to the single crystal apart from a light dechanneling for energies <1.5 MeV.

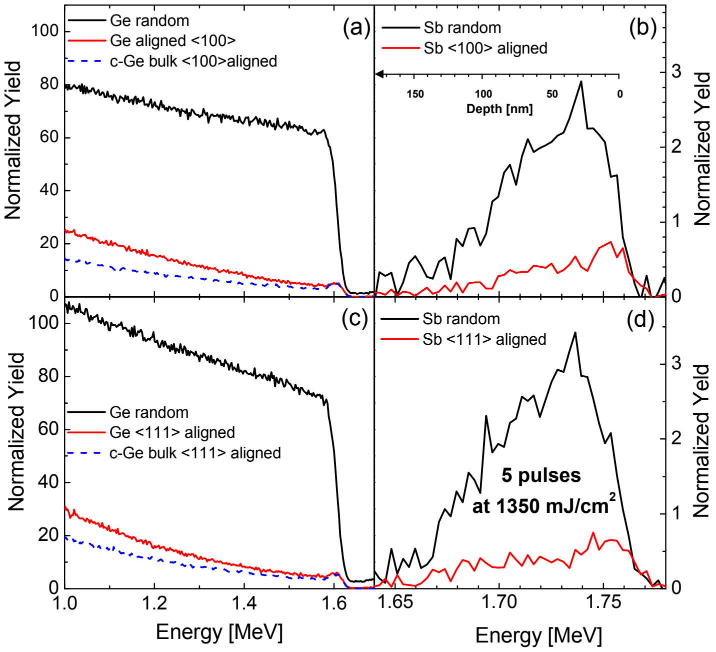

Fig. 4.11 r-RBS (black lines) and c-RBS (red lines) spectra along the <100> and <111> axes in the sample implanted with Sb 50 keV, at a fluence of 6.4x10^{15} Sb$^+$/cm^2 at 300°C, amorphized and then irradiated with five Nd:YAG laser pulses at 1350 mJ/cm^2. Panels (a) and (c) report the Ge signals and panels (b) and (d) the Sb ones in different samples (where the correspondent depth scale of the Sb profile is also plotted). The blue dashed lines in panels (a) and (c) are the spectra along the <100> and <111> axes in a Ge single crystal, reported as a reference.

It is known that the aligned fraction of a solute atom (Sb in our case) along a particular <uvw> axis in the Ge host lattice is defined as [18]:

$$f_{aligned}^{<uvw>}(Sb) = \frac{1-\chi_{min}^{<uvw>}(Sb)}{1-\chi_{min}^{<uvw>}(Ge)}$$

Eq. 4.1

where $\chi_{min}^{<uvw>}(Sb)$ and $\chi_{min}^{<uvw>}(Ge)$ are the minimum channeling yields measured on the impurity and Ge signals, respectively. The aligned fraction furnishes, in first approximation, the fraction of impurity atoms located in substitutional sites. However, there are particular interstitial sites of the diamond lattice that are shadowed only along some directions.

sample	$\chi_{min}^{<100>}(Ge)$	$\chi_{min}^{<111>}(Ge)$
GeSb	0.062	0.054
c-Ge	0.051	0.046

Table 4.3 Obtained values for $\chi_{min}^{<100>}(Ge)$, and $\chi_{min}^{<111>}(Ge)$ in the GeSb and in a crystalline Ge (c-Ge) samples, respectively.

To avoid that such kind of interstitial impurities could be assumed as substitutional it is necessary to measure the aligned fraction along two different axes [19].

In our case, the obtained values for the aligned fraction of Sb atoms along the <100> and <111> axes are 0.75 and 0.85, respectively. Then, since the total Sb fluence in the Ge sample after this laser annealing is (5.4±0.3)x10^{15} Sb/cm^2 while being distributed over a thickness of about 95 nm (see Fig. 4.10), the substitutional Sb concentration results ~ 5x10^{20} Sb/cm^3, i.e., well higher than that reached in literature by conventional techniques [5, 20] and also more than twice with respect the one obtained by Contreras et al. through laser annealing (2.2x10^{20} Sb/cm^3) [21].

In the next section our study will be focused on the comprehension of the effects that laser annealing can have on the electrical activation process of Sb in Ge.

4.4.4 Electrical activation of Sb

In order to study Sb electrical activation in Ge we performed laser annealing with a XeCl excimer laser (λ=308 nm). As previously said (Cfr. section 4.4.1), this laser allows to uniformly irradiate a square area, necessary to perform detailed spreading resistance profiling (SRP). It is worth noting that the different wavelength with respect to the analysis described in previous sections only implies a different absorption coefficient of Ge, but the effects on dopant redistribution are the same, being related to the molten phase. Fig. 4.12 (a) shows chemical Sb profiles in Ge samples implanted with Sb at 50 keV, with a fluence of 6.4 x10^{15} Sb^+/cm^2 at 300°C and amorphized (black continuous line), after excimer laser annealing at an energy density of ~360 mJ/cm^2 with one (violet continuous line) and five subsequent pulses (red continuous line). It is worth noting that from the SIMS and r-RBS analysis, a small Sb loss is observed after 5 pulses, compatible with the results described above (Cfr. Fig. 4.10), after five subsequent pulses a Sb outdiffusion of about 15% is present. It can be observed that laser annealing cause an enlargement of thr Sb profile after one pulse. This can be related to Sb redistribution in the liquid phase produced by the laser pulse. On the other hand, observing Sb elemental profile after five subsequent pulses (red continuous line) it can be seen a Sb accumulation at a depth of around 55 nm from the surface. Moreover, a surprising backdiffusion is observed, against the concentration gradient [evidenced with the green arrow in Fig. 4.12 (a)]. Finally, after five subsequent pulses it can be seen also an increase of Sb concentration near surface with respect to the Sb profile after a single pulse (violet continuous line). In Fig. 4.12 (b), the carrier concentration, i.e. the electrically active profiles, of the same samples plotted in Fig. 4.12 (a) are reported. After one pulse an Sb active concentration up to ~ 8x10^{20} Sb/cm^3 is observed (violet dashed line), evidencing that all the implanted Sb is active. This value agrees with substitutional values found in the previous section. It can be seen also that the active profiles rapidly falls down around 90 nm, evidencing a non active distribution beyond this depth. After five pulses the active profile (red dashed line) shrinks toward the surface to around 50 nm, as evidenced by the red arrow in Fig. 4.12 (b). Moreover, it can be observed that the surface active Sb concentration after five pulses increases up to ~ 1x10^{20} Sb/cm^3. It is worth noting that the SIMS wide peak at 55 nm observed after five pulses laser irradiation [red continuous line in Fig. 4.12 (a)] falls in the region in which the Sb deactivation is observed.

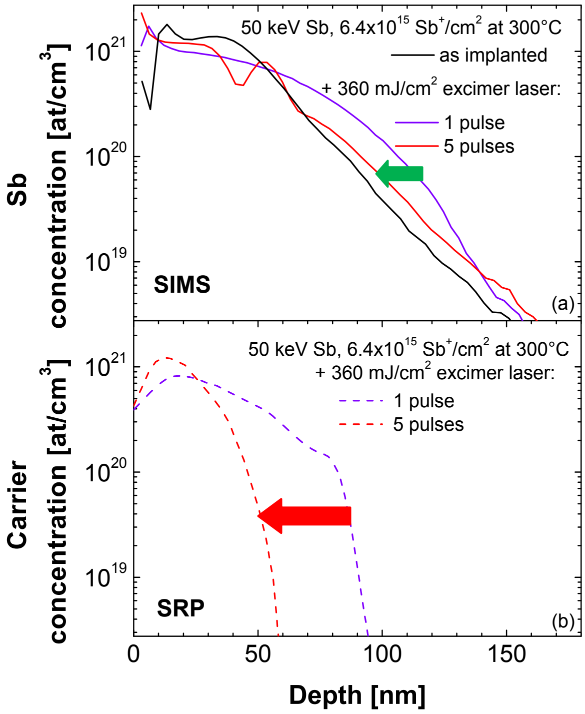

Fig. 4.12 Antimony SIMS (a) and SRP (b) profiles of the samples implanted with Sb 50 keV, at a fluence of 6.4x10^{15} Sb$^+$/cm^2 at 300 °C, amorphized (black line) and then irradiated with XeCl excimer laser with one (violet lines) or five (red lines) pulses at ~ 360 mJ/cm^2. The green arrow evidences the Sb back diffusion, while the red arrow evidences the Sb deactivation occurring after five pulses.

The SIMS and SRP results obtained repeating the same experiment at higher laser energy density (i.e. 600 mJ/cm^2) are reported in Fig. 4.13 (a) and (b), respectively. In particular Fig. 4.13 (a) shows chemical Sb profiles in Ge samples implanted with Sb at 50 keV, with a fluence of 6.4 x10^{15} Sb$^+$/cm^2 at 300°C and amorphized (black continuous line) after excimer laser annealing at energy of ~ 600 mJ/cm^2 with one (violet continuous line) and five subsequent pulses (red continuous line). It can be seen that, as expected, the Sb redistributed profiles extend for a larger region than in the previous case in which a lower energy density irradiation was performed (Cfr. Fig. 4.12). Moreover, it can be seen that the Sb profile after five pulses assumes a box-like shape, due to the fact that Sb can redistribute over the whole molten region during the five subsequent pulses, in agreement with the results obtained in section 4.4.3. However, in this case no evident Sb peak is visible.

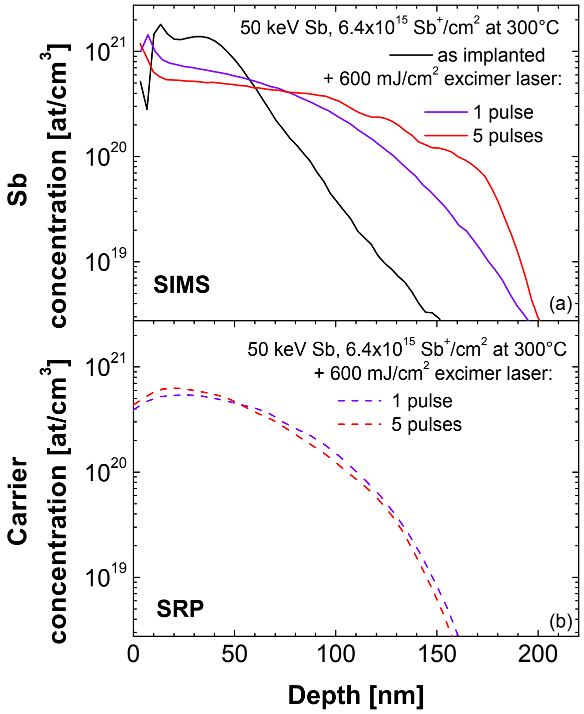

Fig. 4.13 Antimony SIMS (a) and SRP (b) profiles of the samples implanted with Sb 50 keV, at a fluence of 6.4x10^{15} Sb^{+}/cm^{2} at 300 °C, amorphized (black line) and then irradiated with XeCl excimer laser with one (violet lines) or five (red lines) pulses at ~600 mJ/cm^{2}.

Fig. 4.13 (b) shows, indeed, the electrical profiles measured on the same samples reported in Fig. 4.13 (a). In this case no appreciable differences can be observed between Sb active profiles of the samples irradiated at 600 mJ/cm^2 with one (violet dashed line) or five pulses (red dashed line).

All these apparently surprising phenomena can be explained by an empirical model, based on the hypothesis that an excess of vacancies is created in the sample at the l/s interface after LPE regrowth. This suggestion is similar to what observed after laser annealing in Si [22, 23], and is compatible to the results obtained by Contreras et al. in Ge [21].

In this respect, Fig. 4.14 shows the XTEM image of the Ge sample reported in Fig. 4.12, after five excimer laser pulses at an energy density of ~ 360 mJ/cm^2. From Fig. 4.14 it can be observed that this energy density is able to melt all the amorphous region, allowing the recovery of the crystalline phase through the LPE, but it is not able to completely eliminate the extended defects created by amorphization (in the 75 – 120 nm region)[24]. The XTEM image is acquired in off-Bragg bright field conditions to eliminate diffraction contrast and, at the same time, to emphasize the mass contrast. So, in this conditions, it can be affirmed that higher mass/density areas will appear darker than lower mass/density area. Looking closely Fig. 4.14 it can be observed a lighter band at about 55 nm (evidenced by black arrows), compatible with a vacancy enriched (i.e. low-density) zone. In particular this band is located in correspondence of the Sb electrically inactive peak observed in Fig. 4.12. These observation are well-matched with a process for which Sb deactivation occurs because of the interaction with vacancies that can produce stable Sb_m-V_n complexes, as theoretically predicted by Chroneos et al. [25, 26]. These clusters, besides causing the Sb deactivation, act as a sink for further Sb from adjacent regions.

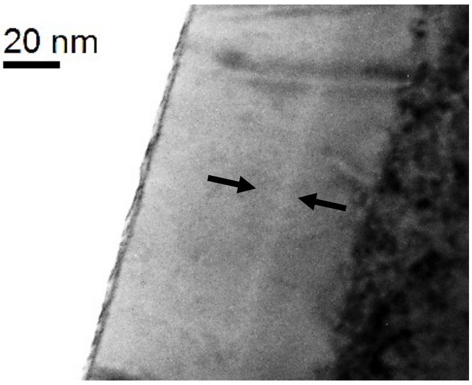

Fig. 4.14 XTEM image of the Ge sample implanted with Sb at 50 keV, with a fluence of 6.4 x10^{15} Sb^+/cm^2 at 300°C and amorphized, after five excimer laser pulses at an energy density of ~360 mJ/cm^2.

It is worth noting that the melt depth depends on different features, such as the absorption coefficient and melting point of the irradiated material and differs from crystalline to amorphous phase [9, 10, 27]. In particular in Fig. 4.15 the original l/s interface (i.e. melt depth) of a crystalline Ge (c-Ge) sample (black line) as well as the one of a sample with a 70 nm-thick amorphous Ge (α-Ge) layer on the top (red line) was calculated as a function of the energy density of the laser pulse, considering a laser wavelength of 308 nm [27]. The simulation was performed with a model based on the phase field approach [28]. The phase field methodology is based on a physical description of the moving phase boundary problem considering a finite dimension of the transition region between the solid and liquid phases. According to this approach the Helmoltz free energy of the system F can be written, as a function of the phase parameter Φ ($0 \leq \Phi \leq 1$, with $\Phi = 0$ and $\Phi = 1$ in the pure liquid and solid phases, respectively), in the form:

$$F = \int_{\Omega} \left[f_{Ge}(\Phi, T) + \frac{\epsilon}{2} |\nabla \Phi|^2 \right] dV$$

Eq. 4.2

where ε is the kinetic parameter controlling the local fluctuations of the phase field, $\nabla\Phi$ corresponds to the interfacial energy, while $f_{Ge}(\Phi,T)$ is the potential term, usually expressed as the sum of a double function plus a term which rules the phase transition [28]. In particular the global minimum of $f_{Ge}(\Phi,T)$ is at $\Phi=0$ (solid) if the temperature T is below the melting point (T_m), conversely is at $\Phi=1$ (liquid) if $T>T_m$. The volume integral in Eq. 4.2 is extended to the whole system volume Ω. The coupled differential equations that describe the evolution of the phase and thermal fields during the laser irradiation are then obtained by minimizing *F* with respect to Φ and considering also the heat diffusion equation that takes into account the laser source. By numerically solving these equations, one can obtain the melt depth as a function of the energy density, as reported in Fig. 4.15.

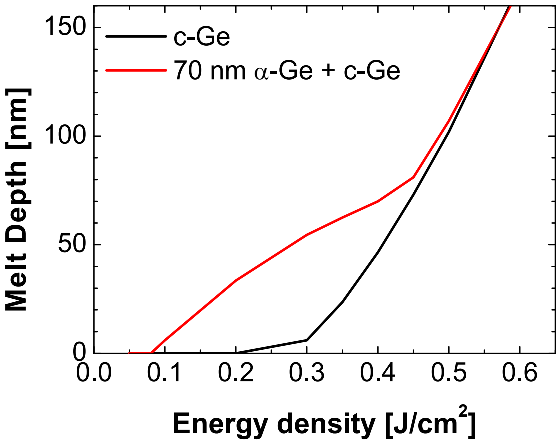

Fig. 4.15 Calculated melt depth as a function of the energy density of the XeCl excimer laser in a c-Ge sample (black line) and in a sample with a 70 nm-thick amorphous layer on the top (red line). The calculation is based on the phase field approach.

It can be seen that the energy threshold to melt α-Ge is lower than that necessary to melt c-Ge. This means that, in our samples, the melt depth after the first laser pulse for the energy density of ~ 360 mJ/cm^2 (i.e. on the amorphized sample) is larger than that obtained with the subsequent pulses because these pulses are performed after the recovering of the crystalline phase (the energy density of ~ 360 mJ/cm^2 used in our case is able to overcome the original amorphous/crystalline interface). The difference of the melt depth between the first pulse and the subsequent pulses becomes less and less pronounced as the laser energy density increases, up to disappear for energy densities higher than ~550 mJ/cm^2 (Fig. 4.15).

All these considerations give rise to the scenario depicted in Fig. 4.16. After the first pulse, all the amorphous layer (60 – 70 nm) is melted, inducing a complete recrystallization of the sample [Fig. 4.16 (a)]. After this, a vacancy excess is left in correspondence of the original l/s interface. Vacancies can interact with Sb causing a deactivation of the Sb profile beyond ~ 90 nm.

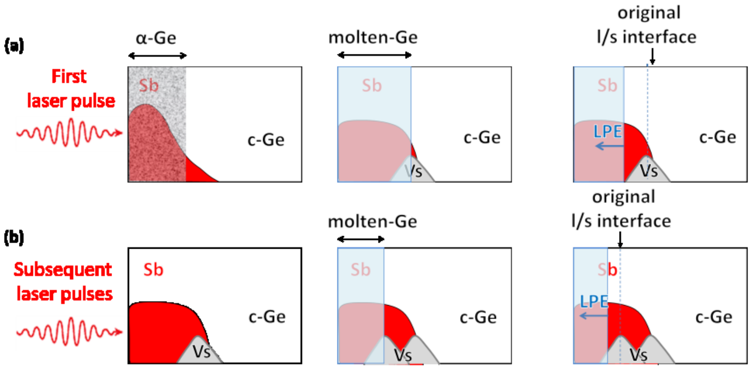

Fig. 4.16 Schematic representation of the empirical model suggested in order to explain Sb deactivation and diffusion observed after multiple pulses. The first pulse (a) occurs on a sample with 70 nm-thick a-Ge on the top. The used energy density of ~ 360 mJ/cm^2 is able to melt a depth higher than the amorphous layer, so after the LPE the sample is crystalline. At the original l/s interface, an excess of vacancies are generated, favoring Sb deactivation. The subsequent laser pulses (b) occur on a crystalline sample, so, according to the calculation presented in Fig. 4.15, the same energy density is able to melt a thinner layer with respect the first pulse (for energy density up to 550 mJ/cm^2). This means that the original l/s interface is located within the Sb active profile and so the vacancy excess generated here, contributes to the deactivation as well as to the Sb backdiffusion, acting as a sink. For further detail see the text.

During the following pulses, being the sample crystalline, the same laser energy density causes the melting of a thinner region (for energies lower than 550 mJ/cm^2), according to Fig. 4.15. Thus, the vacancies produced after these further pulses are located closer to the surface than those relative to the first pulse, in a region in which a high Sb concentration is present. This leads, in the case of the ~ 360 mJ/cm^2 energy density, to the high Sb deactivation beyond 50 nm observed in Fig. 4.12 (b). Moreover, vacancies produced in each pulse add each other [Fig. 4.12 (b)] creating a vacancy supersaturation peaked at ~ 50 nm well-suited with Fig. 4.14. Indeed, a Sb accumulation around 55 nm is compatible with the formation of Sb_m-V_n complexes. They act as a sink for further Sb, during their progressive growth, causing a Sb back-diffusion from the tail. It is worth noting that, Sb in Ge also diffuses through a vacancy mediated mechanism [29, 30], as said before (Cfr. Chapter 1). Thus, in spite of the very short times involved in laser annealing (~ few hundred of nanoseconds), the very large amount of vacancies produced by the laser annealing process (with much higher concentration than in tha Si case [22,23]) allows Sb to diffuse some decades of nanometers. Nonetheless, a role of the temperature gradient or the vacancy gradient in this anomalous Sb diffusion cannot be excluded. As far as the 0-50 nm region is concerned, the increase in Sb concentration (and electrical activation) can be explained considering that, as said before, the Sb back-diffusion of the tails contributes to increase the Sb concentration in correspondence to the vacancy accumulation (i.e. at the original l/s interface). In each pulse (after the first) the l/s interface reaches the peak depth. Thus, it is able to melt part of the clustered Sb, allowing its redistribution within the molten surface layer; this implies a gradual increase of the Sb concentration close to the surface.

All these effects are not visible in the case of high energy irradiation because, in this case, after all the pulses the vacancy excess is generated at the same depth (according to Fig. 4.15). Moreover, the vacancy accumulation occurs at a depth of 150 – 200 nm at which the Sb concentration is lower than before. Finally, in the case of 600 mJ/cm^2 irradiation, the melt depth is much deeper than the as implanted Sb profile, so there is no Sb beyond the l/s interface to be sinked by vacancy accumulation and thus promoting Sb_m-V_n cluster growth and, subsequently, the increase of surface Sb concentration.

4.5 Incorporation of Sb in the laser melting regime: MBE grown samples

Even if laser annealing shows great potentialities in increasing the Sb incorporation in Ge, the final Sb profile and hence the maximum Sb substitutional or electrical active concentration is still limited by the fluence that can be implanted in Ge before structural modifications (i.e. porous structure) occur. In fact, though laser annealing recovers the crystal phase, the swelling of Ge during Sb implantation reduces the dopant concentration already in the as implanted samples (Cfr. section 4.4.2). These effects can be avoided by high temperature implants. However, self-sputtering during the implant can limit Sb content. In order to overcome these issues different strategy was also followed: GeSb samples with high Sb concentration were grown through MBE as described below.

4.5.1 Experimental

As discussed in paragraph 4.2 the epitaxial growth of Sb doped Ge films is limited by Sb high segregation at the temperature needed to obtain a good crystal quality of the film itself. Nonetheless, the capability of the laser to recover sample crystal structure shown before could solve this problem. So, some samples were prepared by MBE, depositing at 100 °C in a way to avoid Sb segregation, as reported above [7] and with a growth rate of 0.5 Å/s. With these conditions, a 55-nm-thick $Ge_{1-x}Sb_x$ (x=0.06) film was grown on a (100) Ge-on-insulator (GeOI) substrate (c-Ge/SiO_2/Si) with a top c-Ge layer 35 nm thick, as schematically shown in Fig. 4.17. The growing parameters (i.e. low substrate temperature) makes the film deposition to be far from an epitaxial growth, but depositing an amorphous layer while maintaining a flat surface. In fact, no appreciable roughness has been observed by SEM analysis with respect to the untreated Ge. Indeed, this low-T deposition allows to incorporate a very high amount of Sb, with a profile that is flat already after the deposition, by playing with the temperature of the Sb cell and the deposition rate in the MBE system. Furthermore the low Ge evaporation rate, chose together with a temperature of the Sb cell of 460 °C, for instance, allow us to incorporate a flat concentration of Sb as high as 2.5×10^{21} Sb/cm^3.

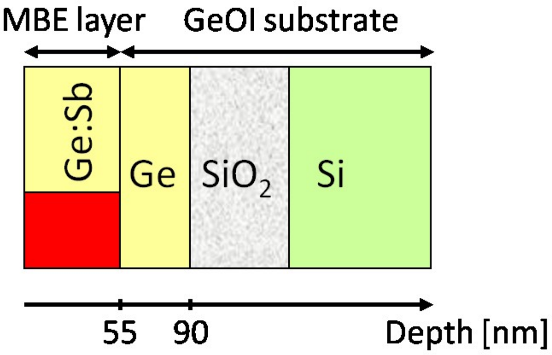

Fig. 4.17 Schematic representation of the sample obtained by low temperature (i.e. 160°C) MBE deposition: a ~ 55 nm-thick layer of GeSb on a GeOI substrate characterized by a ~ 35 nm-thick Ge layer on the top.

This sample was then cut and each piece, annealed with Nd:YAG laser (λ=532 nm) at 550 mJ/cm^2. The details of the laser beam are reported in section 4.4.1. In particular the energy of the laser pulse, in this case, was chosen in order to melt the sample beyond the original interface between the MBE layer and the GeOI substrate but before the Ge/SiO_2 interface. This has been made in order to save a thin crystalline Ge layer to act as a seed for the LPE process of the melted layer. It is worth noting that in the GeOI case lower energies are needed to melt Ge, with respect to the Ge-bulk case, because of the underneath oxide that hinder heat dissipation, while being the reflectance comparable in the two systems, at the used wavelength [31]. Indeed the absorption length of Ge at the used wavelength is $\alpha^{-1} \cong 50nm$ [9,10], so it is smaller than the Ge/SiO_2 interface depth. After laser annealing, r-RBS and c-RBS analysis were performed in order to evaluate the substitutional fraction of dopant (for more detail on the experimental apparatus see section 4.4.1). Furthermore, measurements of the lattice parameters were carried out by means of High-resolution x-ray diffraction (HRXRD) ω−2θ scans (rocking curves, RCs) with a Philips MRD X-Pert PRO™ diffractometer equipped with a parabolic mirror and a Bartels monochromator, located at the University of Padova. Moreover, the combined use of the parabolic mirror and of an Anton Paar DHS 900 hot stage allowed us to collect on selected samples in situ fast RCs in an N_2 atmosphere during a linear annealing ramp. The temperature range spanned from room temperature (RT) to ~ 500°C and the temperature was raised by ΔT = 3°C every Δt = 14 min [32].

4.5.2 Very high incorporation of Sb in Ge

The used laser annealing process allows both the surface amorphous GeSb layer to recrystallize and the eventual defects at the MBE film/GeOI substrate interface to disappear, while Sb can redistribute also in the GeOI top Ge layer melted by the laser irradiation. Fig. 4.18 shows c-RBS (red line) and r-RBS (black line) analysis of the MBE grown GeSb sample irradiated with five Nd:YAG laser pulses at 550 mJ/cm^2. From these analysis it can be observed that a concentration as high as ~1.3×10^{21} Sb/cm^3 is substitutional.

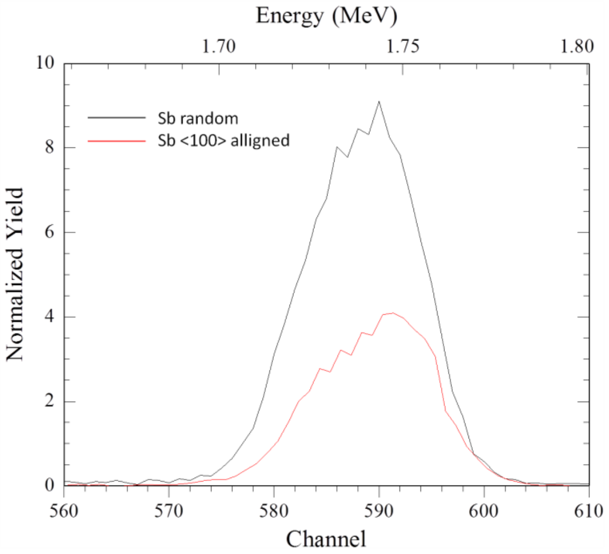

Fig. 4.18 r- and c-RBS spectra along the <100> axis (black and red line, respectively) in the MBE grown GeSb sample and then irradiated with five Nd:YAG laser pulses at 550 mJ/cm^2.

This means that by combining low-T epitaxial growth of Sb doped Ge and melting by laser annealing it is possible to reach Sb substitutional concentrations much higher than those ever obtained before (Cfr. Section 4.4.3). Moreover, the possibility of varying the thickness of the molten layer by varying the laser energy fluence also allows to control the final profile (depth and shape) of the incorporated Sb. These results confirm laser annealing as a very promising alternative technique for optimizing *n*-type doping in Ge.

4.5.3 Thermal stability of Sb in Ge

In the previous sections we demonstrated that laser annealing is able to induce a very high Sb incorporation in substitutional Ge sites, well above the solubility limit of Sb in Ge. In this section, we focus the attention on the stability of the incorporated Sb in the GeOI structure, reporting HRXRD investigation on how Sb behaves if further thermally annealed up to a temperature of about 500 °C.

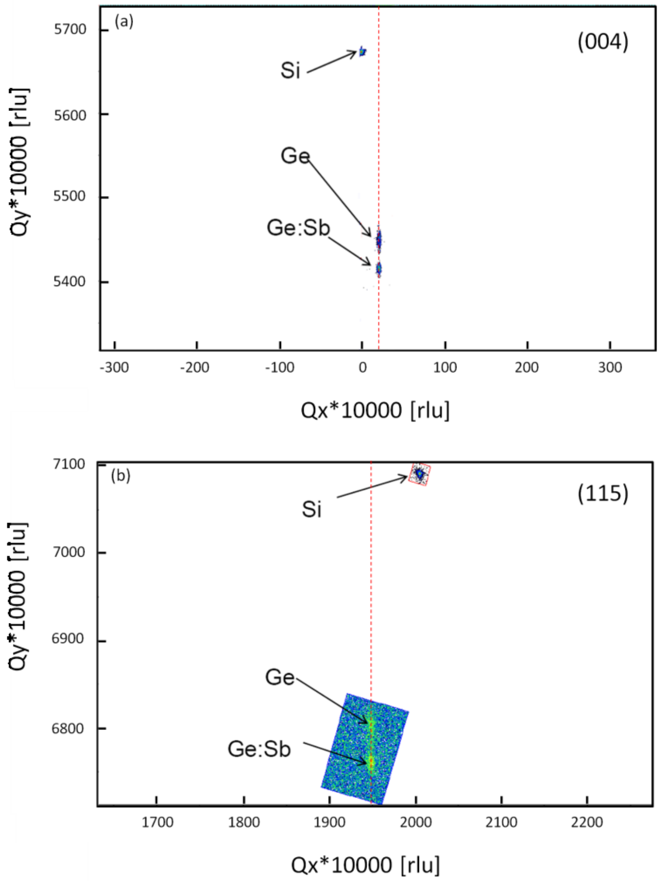

Fig. 4.19 RLMs around the (004) and (115) RL points of the MBE grown GeSb sample irradiated with five Nd:YAG laser pulses at 550 mJ/cm^2 are reported in panel (a) and (b), respectively.

The dimensions of the x-ray spot impinging on the samples were reduced up to 2x2 mm^2 and very accurate alignments were adopted in order to collect the signal only at the center of the laser-irradiated regions. We performed reciprocal lattice maps (RLMs) around the (004) and (115) RL points, reported in Fig. 4.19 (a) and (b), respectively. In both RLMs three signals due to Si, Ge, and GeSb layers are observed. It is worth noting that the (004) RLM discloses the existence of a tilt (0.4°) between the Si and the Ge lattice planes, a common feature exhibited, in various extents, by the majority of the multilayer structures realized by smartcut processes [33]. Nonetheless, as can be observed (red dashed line), there is no tilt between the pure Ge and the Sb-doped Ge layers (as expected, since it is regrown by liquid phase epitaxy).By combining the results obtained by both the RLMs after laser irradiation, we verified that the lattice parameter of Ge is that of bulk Ge and that the Sb-doped Ge layer is pseudomorphic to the underlying Ge substrate . This means that GeSb layer and Ge shared the in-plane lattice parameters, as schematically depicted in Fig. 4.20.

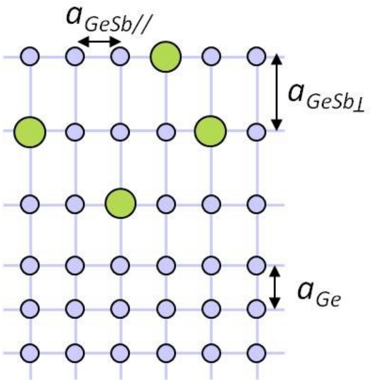

Fig. 4.20 Schematic representation of the pseudomorphic configuration of a GeSb layer on Ge. In particular, light blue and green circles represent Ge and Sb atoms in the lattice sites, respectively. In this configuration the bulk Ge and the in-plane GeSb layer lattice parameters (represented as a_{Ge} and $a_{GeSb//}$, respectively) are the same, while a tetragonal distortion of the GeSb film along the direction perpendicular to the growth plane is evidenced.

Moreover, RLMs recorded after *in situ* annealing (up to 488°C), demonstrate that the GeSb film is still pseudomorphic to Ge, i.e., no relaxation of the GeSb film is observed. In order to clarify the strain status of the structure after laser irradiation, in Fig. 4.21 we report, as an example, the (004) RC of the GeOI sample lasered with five subsequent pulses at 550 mJ/cm^2 (line plus open circles). Here we used the maximum angular acceptance due to the weak signals produced by the thin Ge and GeSb layers. This acquisition strategy is mandatory also to collect quick *in situ* measurements. The Bragg peak related to the Si thick substrate is located at 0 arcsec, while at negative angles the Ge and GeSb epilayers Bragg peaks are marked. As mentioned above, due to the different covalent radii, the presence of Sb induces a positive lattice strain in the Ge lattice. In particular, since the GeSb layer remains pseudomorphic to the substrate, as previously evidenced by the RMLs, the presence of substitutional Sb atoms induces a tetragonal distortion on the Ge host lattice along the direction perpendicular to the growth plane, as depicted in Fig. 4.20. This fact, keeping in mind the Bragg's law, generates a peak in the RC located at the left side of the Ge related peak.

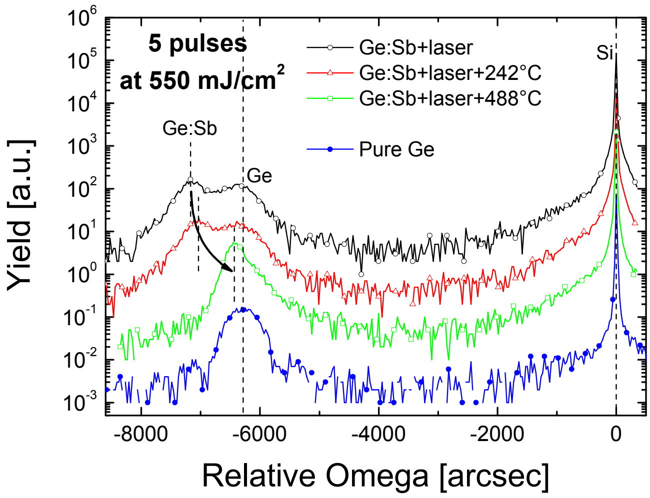

Fig. 4.21 (004) RCs of the MBE grown GeSb sample irradiated with five Nd:YAG laser pulses at 550 mJ/cm^2 (black line plus open circles) and further thermally annealed up to 242 °C (red line plus open triangles) and up to 488 °C (green line plus open squares). The RC of a pure c-Ge sample (blue line plus closed circles) is also plotted as a reference.

In Fig. 4.21, the comparison between the RC of the sample with Sb just after laser irradiation (line plus open circles) and the one of a reference pure GeOI (without Sb, line plus closed circles) clearly evidences that this left-hand side peak (at about 7000 arcsec) is absent in the latter case, definitively demonstrating that it is strictly related to the positive strain generated by Sb in the Ge host lattice when substitutionally located after laser annealing.

By using the differential form of the Bragg law [33], we can obtain the perpendicular lattice parameter of the GeSb film ($a_{GeSb\perp}$) from the distance between the Ge and the GeSb peaks [34]. Moreover, since it is pseudomorphic to the Ge layer (i.e., $a_{Ge} = a_{GeSb\parallel}$, where a_{Ge} and $a_{GeSb\parallel}$ are the bulk Ge and the in-plane GeSb layer lattice parameters, respectively), with the help of the elasticity theory, we can obtain the corresponding GeSb film relaxed lattice parameter ($a_{GeSbrelax}$, i.e., the lattice parameter once the epitaxial constraint is removed, as schematically depicted in Fig. 4.22) from the relation:

$$\frac{a_{GeSb\perp} - a_{GeSbrelax}}{a_{GeSbrelax}} = -2\frac{C_{12}}{C_{11}}\frac{a_{Ge} - a_{GeSbrelax}}{a_{GeSbrelax}}$$

Eq. 4.3

where C_{12} and C_{11} are the elastic constants of Ge [35].

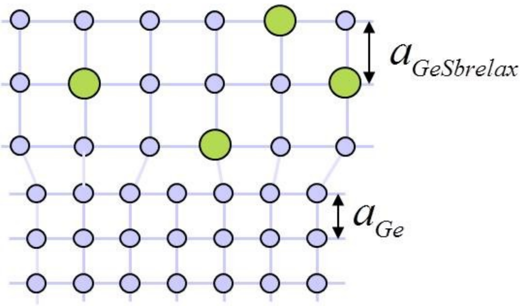

Fig. 4.22 Schematic representation of the relaxed configuration of a GeSb layer on Ge. In particular, light blue and green circles represent Ge and Sb atoms in the lattice sites, respectively. Moreover, the bulk Ge and the GeSb layer lattice parameters are represented as a_{Ge} and $a_{GeSbrelax}$, respectively.

Then, since no information on the relation between the $a_{GeSbrelax}$ is available, in order to extract the Sb concentration (*x*) by HRXRD measurements, we use the Vegard's law:

$$a_{GeSbrelax} = a_{Ge}(1-x) + \left(8\frac{r_{Sb}}{\sqrt{3}}\right)x$$

Eq. 4.4

This relation is applied under the assumption that the residual off-lattice Sb gives a negligible or even absent strain contribution. As a result, we can estimate that the Sb concentration after laser annealing is about 1.1x10^{21} Sb/cm^3 (in agreement with c-RBS analysis reported in section 4.5.2). This further demonstrates that off-lattice Sb induces negligible strain in the Ge lattice.

Fig. 4.23 reports the trend of the lattice parameter $a_{GeSbrelax}$ obtained by the analysis of the RCs collected *in situ* during the linear temperature ramp.

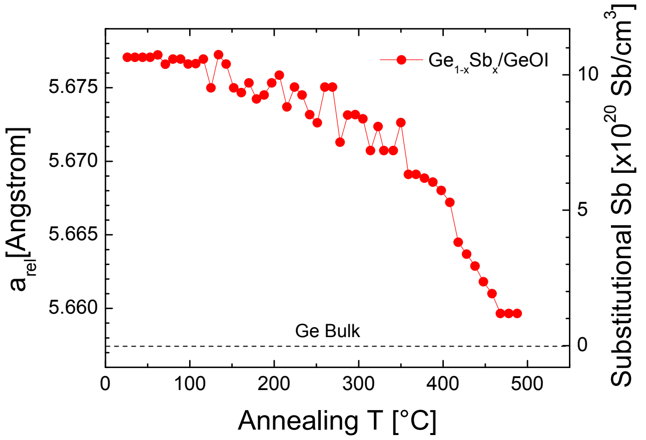

Fig. 4.23 Relaxed lattice parameter ($a_{GeSbrelax}$) of the $Ge_{1-x}Sb_x$ alloy obtained by the analysis of the RCs collected *in situ* during the linear temperature ramp. On the left is plotted the correspondent substitutional Sb concentration, related to $a_{GeSbrelax}$ by the Vegard's law.

We observe that $a_{GeSbrelax}$ continuously decreases as the temperature is increased, as testified by the GeSb peak shift in the RCs in Fig. 4.21 increasing the temperature to T=242 °C and 488 °C (open triangles and squares, respectively). This means that substitutional Sb fraction decreases with annealing, causing a lowering of the maximum substitutional Sb concentration from ~1.1 x10^{21} Sb/cm^{3} (just after laser annealing) to a value of ~ 1x10^{20} Sb/cm^{3} after 488 °C.

In order to verify if the decrease in $a_{GeSbrelax}$ is due to Sb outdiffusion or precipitation r-RBS and c-RBS analysis were performed in the sample after the annealing at 488°C. r-RBS analysis demonstrate that less than 4x10^{15} Sb/cm^{2} (~25%) has left the sample. On the other hand, c-RBS and r-RBS spectra of this sample after thermal annealing, shown in Fig. 4.24, indicate that most of Sb has indeed precipitated and the substitutional Sb concentration is reduced to ~2.5x10^{20} Sb/cm^{3}, very close to the value extrapolated by strain analysis in Fig. 4.23.

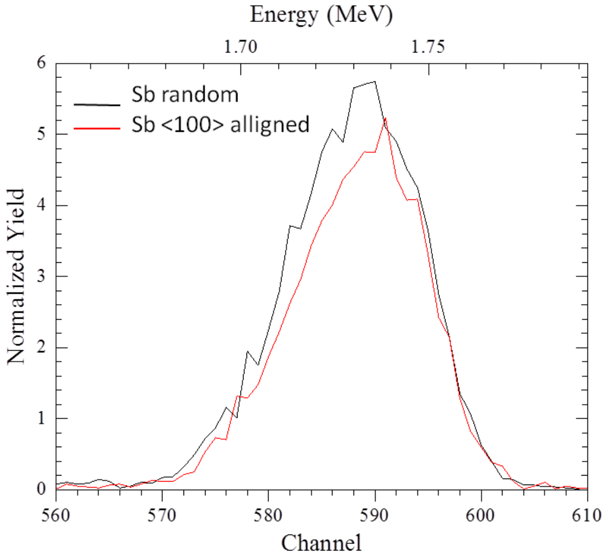

Fig. 4.24 r- and c-RBS spectra along the <100> axis (black and red lines, respectively) of the MBE grown GeSb sample irradiated with five Nd:YAG laser pulses at 550 mJ/cm^{2} and then annealed up to 488°C.

This means that the change in the lattice parameter shown in Fig. 4.23 is due to Sb going off-lattice. Indeed, contrary to what happens in Si [36], the precipitated Sb does not induce a further increase in positive strain due to cluster formation, since no strain inversion is observed after annealing up to 488 °C. Thus, we can assume that off-lattice Sb does not produce any appreciable strain to the Ge host lattice.

Finally, it is worth noting that the $a_{GeSbrelax}$ reduction cannot be ascribed to the small Sb loss observed under thermal annealing. In fact, even if all lost Sb would have come only from the previously substitutional Sb fraction, a fluence of ~ $5.5\text{x}10^{15}$ Sb/cm^2 should have been still substitutional, corresponding to a $a_{GeSbrelax}$=5.669 Å, while $a_{GeSbrelax}$ reaches a much lower value after the annealing (Fig. 4.23).

4.6 Conclusions and perspectives

In conclusion, we demonstrated at laser annealing is able to promote substitutional and electrically active Sb incorporation in Ge at very high concentrations. These could have enormous potentialities to realize proper doped virtual substrates for tensile Ge. This films, in turn, are predicted to be efficient light emitters. Indeed, due to the surface melting, this kind of annealing is able to eliminate also that permanent damage resistant to conventional thermal annealing, such as the porous structure, thus recovering the surface quality. Moreover, due to the high Sb mobility in the liquid phase, a complete redistribution of the dopant over the whole molten depth can be gained, while achieving very high concentration of substitutional Sb in Ge. In particular, by coupling low temperature deposition techniques and laser annealing, concentrations of substitutional and electrically active Sb higher than $1\text{x}10^{21}$ Sb/cm^3, well above the Sb solid solubility in Ge and of any other value ever obtained so far in literature, have been obtained. However, the electrical analysis showed a characteristic phenomenon of Sb deactivation in correspondence of the l/s interface that can be attributed to a generation of a vacancy excess at l/s original interface after laser annealing. This phenomenon has been empirically modeled, evidencing that vacancies can induce Sb deactivation by the formation of very stable Sb_m-V_n complexes, that can act as a sink for Sb atoms inducing also a back-diffusion of Sb against the concentration gradient.

However, we observed that the very high doped Ge layers obtained in this way are always pseudomorphic to the Ge substrate, and the elastic energy of this metastable state is released during further thermal annealing leading Sb to go out of lattice already at 500°C. On the basis of the results obtained so far, it is clear that further efforts are needed to reach a Ge-based light source. In fact, we are still investigating several approaches, e.g. structural modifications aimed to make the GeSb layer relaxed to its characteristic lattice parameter, while maintaining Sb in substitutional electrically active position. This step is essential to use this layer as a substrate for tensile Ge. In parallel to it many efforts are devoted to study and optimize the realization of the top Ge tensile film, as well as the final device structure, with the help of a proper theoretical support either for the laser annealing related phenomena and for the band structure calculations. The goal of this research, even if many open points still need to be solved, will surely represent a breakthrough in the field of information technology.

4.7 References

1. J. Kouvetakis, J. Menendez, and A.V.G. Chizmeshya, Annu. Rev. Mater. Res. **36**, 497 (2006), and references therein.
2. IUPAC (International Union of Pure and Applied Chemistry), http://www.iupac.org/ .
3. F. A. Trumbore, Bell Syst. Tech. J., **39**, 205 (1960).

4. B. Stritzker, R.G. Elliman, J. Zou, Nucl. Instrum. Meth. B **175-177**, 193 (2001).
5. A. Satta, T. Janssens, T. Clarysse, E. Simoen, M. Meuris, A. Benedetti, I. Hoflijk, B. De Jaeger, C. Demeurisse, and W. Vandervorst, J. Vac. Sci. Technol. B **24**, 494 (2006).
6. T. Janssens, C. Huyghebaert, D. Vanhaeren, G. Winderickx, A. Satta, M. Meuris, and W. Vandervorst, J. Vac. Sci. Technol. B **24**, 510 (2006).
7. M. Oehme , J. Werner, E. Kasper, J Cryst. Growth. **310**, 4531 (2008).
8. K. Nakagawa, N. Sugii, S. Yamaguchi, M. Miyao, J Cryst. Growth. **201-202**, 560 (1999).
9. J. M. Poate and J. W.Mayer, *Laser Annealing of Semiconductors* (Academic, New York, 1982).
10. J. Poate, G. Foti, and D. Jacobson, *Surface Modification and Alloying by Laser, Ion, and Electron Beams*(Plenum, New York, 1983).
11. V. Mazzocchi, C. Sabatier, M. Py, K. Huet, C. Boniface, J-P. Barnes, L. Hutin, V. Delayer, D. Morel, M. Vinet, C. Le Royer, J. Venturini, and K. Yckache, 17th IEEE International Conference on Advanced Thermal Processing of Semiconductors, 1 (2009).
12. Ziegler J. F., J. P. Biresack, and U. Littmark, *The Stopping and the Range of Ions in Solids* (Pergamon, New York, 1985); http:// www.srim.org.
13. J. S. Preston and H. M. van Driel, Phys. Rev. B **30**, 1950 (1984).
14. M. Mulato, D. Toet, G. Aichmayr, P. V. Santos, and I. Chambouleyron, J.Appl. Phys. **82**, 5159 (1997).
15. I. Suni, G. Göltz, and M.-A. Nicolet, S. S. Lau, Thin Solid Films **93**, 171 (1982).

16. J. P. Garandet, J. Cryst. Growth **310**, 3268 (2008).
17. A. Ostrogorsky and G.Müller, J. Cryst. Growth **121**, 587 (1992).
18. J. R. Tesmer, and M. Nastasi, eds., *Handbook of modern ion beam materials analysis*, (Materials Research Society, Pittsburg, 1995).
19. D. V. Morgan, *Channeling Theory, Observation and Application*, (John Wiley & Sons, New York, 1973).
20. E. Simoen, A. Satta, A. D'Amore, T. Janssens, T. Clarysse, K. Martens, B. De Jaeger, A. Benedetti, I. Hoflijk, B. Brijs, M. Meuris, W. Vandervorst, Mat. Sci. Semicon. Proc. **9**, 634 (2006).
21. G. Contreras, L. Tapfer, A. K. Sood, M. Cardona, Phys. Status Solidi B **131**, 475 (1985).
22. G. Mannino, V. Privitera, A. La Magna, and E. Rimini, E. Napolitani, G. Fortunato and L. Mariucci, Appl. Phys. Lett. **86**, 051909 (2005).
23. A. La Magna, V. Privitera, G. Fortunato, and M. Cuscunà, B. G. Svensson, and E. Monakhov, K. Kuitunen, J. Slotte, and F. Tuomisto, Phys. Rev. B **75**, 235201 (2007).
24. P. Tsouroutas, D. Tsoukalas, I. Zergioti, N. Cherkashin, and A. Claverie, J. Appl. Phys. **105**, 094910 (2009).
25. A. Chroneos, R. W. Grimes, B. P. Uberuaga, H. Bracht, Phys. Rev. B **77**, 235208 (2008).
26. A. Chroneos, J. Appl. Phys. **107**, 076102 (2010).
27. W. Szyszko, Appl. Surf. Sci. **90**, 325 (1995).
28. A. La Magna, P. Alippi, and V. Privitera, G. Fortunato, M. Camalleri, B. Svensson, J. Appl. Phys. **95**, 4806 (2004).
29. S. Brotzmann and H. Bracht, J. Appl. Phys. **103**, 033508 (2008).
30. C. Claeys and E. Simoen, *Germanium-Based Technologies-From Materials to Devices,* (Elsevier, Amsterdam, 2007), and references therein.
31. E. Centurioni, Appl. Opt. **44**, 7532 (2005).

32. G. Bisognin, D. De Salvador, E. Napolitani, M. Berti, A. Polimeni, M. Capizzi, S. Rubini, F. Martelli, and A. Franciosi, J. Appl. Crystallogr. **41**, 366 (2008).

33. T. Ma, H. Tu, G. Hu, B. Shao, and A. Liu, J. Cryst. Growth **289**, 489 (2006).

34. V. Holý, U. Pietsch, and T. Baumbach, *High Resolution X-Ray Scattering from Thin Films and Multilayers (*Springer, Berlin, 1998).

35. O. Madelung, *Semiconductors: Basic Data*, (Springer, Marburg, 1996).

36. Y. Takamura, A. F. Marshall, A. Mehta, J. Arthur, P. B. Griffin, J. D. Plummer, and J. R. Patel, J. Appl. Phys. **95**, 3968 (2004).

List of publications

This thesis is based on the following publications:

1. **Role of self-interstitials on B diffusion in Ge**
   G. G. Scapellato, E. Bruno, A.J. Smith, E. Napolitani, D. De Salvador, S. Mirabella, M. Mastromatteo, A. Carnera, R. Gwilliam, and F. Priolo.
   Nucl. Instr. Meth. in Phys. Res. B (in press) - DOI:10.1016/j.nimb.2011.08.041

2. **Self-interstitial injection in crystalline Ge induced by GeO_2 nanoclusters**
   G. G. Scapellato, S. Boninelli, E. Napolitani, E. Bruno,A.J. Smith, S. Mirabella, M. Mastromatteo,D. De Salvador,R. Gwilliam, C. Spinella, A. Carnera,and F. Priolo.
   Phys. Rev. B **84**, 024104 (2011) - DOI: 10.1103/PhysRevB.84.024104

3. **Radiation enhanced diffusion of B in crystalline Ge**
   E. Bruno, S. Mirabella, G.G. Scapellato,G. Impellizzeri, A. Terrasi, F. Priolo,E. Napolitani, D. De Salvador, M. Mastromatteo, A. Carnera
   Thin Solid Films **518**, 2386 (2010) - DOI: 10.1016/j.tsf.2009.09.173

4. **High-level incorporation of antimony in germanium by laser annealing**
   E. Bruno, G. G. Scapellato, G. Bisognin, E. Carria, L. Romano, A. Carnera, and F. Priolo
   J. Appl. Phys. **108**, 124902 (2010) - DOI: 10.1063/1.3520671

5. **Recent Insights in the Diffusion of Boron in Silicon and Germanium**
   Mirabella S., De Salvador D., Bruno E., Napolitani E., Scapellato G. G., Mastromatteo M., Impellizzeri G., Bisognin G., Boninelli S., Terrasi A., Carnera A., Priolo F.
   ECS Transactions **33**, 167 (2010) - DOI: 10.1149/1.3485691

6. **Transient enhanced diffusion of B mediated by self-interstitials in preamorphized Ge**
   E. Napolitani, G. Bisognin, E. Bruno, M. Mastromatteo, G.G. Scapellato, S. Boninelli, D. De Salvador, S. Mirabella, C. Spinella, A. Carnera, F. Priolo
   Appl. Phys. Lett. **96**, 201906 (2010) - DOI: 10.1063/1.3429084

7. **Mechanism of B diffusion in crystalline Ge under proton irradiation**
   E. Bruno, S. Mirabella, G.G. Scapellato, G. Impellizzeri, A. Terrasi, E. Napolitani, D. De Salvador, M. Mastromatteo, A. Carnera, F. Priolo
   Phys. Rev. B **80**, 033204 (2009) - DOI: 10.1103/PhysRevB.80.033204

Other publications:

1. **Defects in Ge caused by sub-amorphizing self-implantation: Formation and dissolution**
   G. Bisognin, S. Vangelista, M. Mastromatteo, E. Napolitani, D. De Salvador, A. Carnera, M. Berti, E. Bruno, G.G. Scapellato, A. Terrasi
   Thin Solid Films **518**, 2326 (2010) - DOI: 10.1016/j.tsf.2009.09.136

Curriculum vitae

Giorgia Graziella Scapellato was born on 23th of April 1984 in Catania (Italy). In 2003 she obtained the General Certificate of Education at the Technical Institute "Guglielmo Marconi" of Catania (Information Technology specialization) with mark 100/100. She studied Physics at the University of Catania (Italy), attaining the First Degree in Physics with full marks (110/110 *cum laude*) on 24th of November 2006. Then she attained her Master Degree in Physics with full marks (110/110 *cum laude*) on 10th of October 2008. In November 2008 she was admitted to the three-year Ph.D. course in Material Science at the University of Catania. In November 2011 she had a post-doc position at CNR-IMM-UOS Catania (University). She has also collaborated with several groups: CNR-IMM, University of Padova, University of Münster, University of Surray through the European consortio SPIRIT (Support Of Public And Industrial Research Using Ion Beam Technology). Giorgia G. Scapellato has been mainly involved in experimental studies concerning the doping process in Ge for micro and optoelectronics, under the supervision of Prof. F. Priolo. In particular she investigated During the Ph.D. course she attended international conferences and schools (E-MRS Spring meeting, 2010 France; E-MRS Spring meeting, 2011 France; 16th International Winterschool on New Developments in Solid State Physics, Austria; the "47th Course of the International School of Solid State Physics on "Materials for Renewable Energy", Italy; SPIRIT Tutorial on "Ion implantation and irradiation", Germany; SPIRIT Tutorial on "High resolution depth profiling", France), giving oral and poster contributions. She won the young scientist award at E-MRS 2011. Moreover, Giorgia G. Scapellato is author or co-author of several articles, published in international referred scientific journals.

Acknowledgments

I think that, surely, I will not be able to express the gratitude in a way suitable to all the people I met during these three years of PhD, and for this I apologize in advance.

First of all I want to say thanks to my tutor, Prof. F. Priolo that has given me the possibility, as well as the enthusiasm, to work in the field of material science. His enlightening discussions, as well as all his advice and encouragement, give me the opportunity to grow every day in my research experience. I have learned very much from his strong physical sense.

I am deeply grateful to my supervisor Dr. Elena Bruno who has shared with me all the results and the activities of this experimental thesis. Her scientific support and her sincere friendship have been essential for me.

Heartfelt thanks to my fellow travelers Egidio and Paolo. We shared exams, study, work, from the first year of University until the last year of PhD. But we also have shared confidences, laughter and the usual volleyball tournaments ... we are the blue team! Obviously with our great “president” Dr. Roberto Lo Savio. Thanks to your sincere support.

Thanks also to my special friend Ciccio, for all the shared moment, for the “theoretical” discussions and for all the advices given to me. Simply thanks for everything.

I want to thank Prof. A. Terrasi, for his knowledge and experience in MBE laboratory, Prof. M.G. Grimaldi, for her frankness and scientific support in RBS analysis and laser annealing process, and Prof. E. Rimini for his enormous wisdom. In the last PhD year, I also had the pleasure of knowing Dr. V. Privitera. I especially thank him for the relaxing and, at the same time, stimulating discussions, and also for the cordiality and the attentions that he has given to each person. Thanks also to dr. G. Franzò for the her special support. I would like to acknowledge also Dr. A.J. Smith (*Ion Beam Centre*, The University of Surrey, Guildford, United Kingdom) and Dr. G. Fortunato (CNR-IMM, Rome, Italy) for their collaboration. Moreover very special thanks go to Prof. H. Bracht, and all the people of his group, for inviting me and my supervisor to work with them, and for all the very fruitful discussions.

I consider myself very lucky to have had the opportunity to work within the MATIS group. In this context, indeed, I met very special people that I want to thank. Dr. Salvo Mirabella, for his ability to explain in the simplest way also very complicate notions. Dr. Simona Boninelli, for her determination and her experience in TEM and SEM analysis. Dr. Lucia Romano, for her kindness and her teachings, as well as for the RBS and SEM support and for all the happy moments shared with me. Dr. Maria Miritello, for her enthusiasm and for the Sputtering expertise. Dr. Giuliana Impellizzeri, for her always kind and caring attitude and, Dr. Isodiana Crupi for her generosity and sincerity. I want also to thank the group of Padua: Dr. Enrico Napolitani, for his SIMS experience and for the long discussions, Dr. Gabriele Bisognin for all HRXRD analysis, Dr. Davide De Salvador for the simulation code and specially Dr. Massimo Mastromatteo for the fruitful discussions and the patience shown to me. Thanks also to Carmelo Percolla, Salvo Tatì and Giuseppe Pantè for their essential technical support.

Thanks to many members of the CNR-IMM center of Catania: Dr. Antonino La Magna for his collaboration; Dr. Markus Italia for the SRP analysis; Antonio Marino for some implants; Antonio Mio; Corrado Bongiorno and Salvo Pannitteri for the technical support and the pleasant threads, and of course the director Dr. Corrado Spinella.

I can not forget all the people that have shared their life with me at the Department of Physics: Salvo Cosentino, Pietro Artoni, Gabriele Bellocchi, Dr. Emanuele Pecora, Dr. Francesco Ruffino, Dr. Alessia Irrera, Dr. Alessandra La Greca, Primo Furno, Dr. Giuseppe Politi, Prof. Giuseppe Angilella, Dr. Massimiliano Chiorboli, Dr. Alessio Cardillo, Dr. Roberta Sinatra and Dr. Enzo Nicosia, the best actor in the joke for the first year students! A special thank to Dr. Daniele D’Angelo for organizing all the sportive activities and social events that have made our life in the Department always cheerful. Moreover I want to thank Dr. Salvo Bagiante for the fun times spent together and for all the conversation, always pleasant.

Finally I want to show my gratitude to all the people outside the “scientific environment”. First of all I want to say thanks to my family that always support me: my mum to be so charming and for conveying to me the gift of faith, my dad who is always ready to play around and has inspired me to become a physicist, my sister who is always so determinate and specially my brother that gives me precious technical and moral support. Thanks to my cousins Giovanna, Pamela and Sara, and also to my fiends Angela, Diana, Teresa and Paolo Bonini and Don Peppe to have always supported me and for all the special moments that we share.

A big hug I send to my friend Peppe Raciti, who, I’m sure, is shearing with me this special moment, even though is not here anymore.

Finally I want to thank the person who, more than any other, supported me every day and changes every second in a special moment: thanks to my love Peppe.